On The Roles of Radiation and Low-Level Vorticity in Numerical Simulations of Tropical Cyclogenesis

by

Warren (Ren) Paul Smith II

M.S., University of Colorado Boulder, 2017

B.S., Minnesota State University, Mankato, 2013

A thesis submitted to the
Faculty of the Graduate School of the
University of Colorado in partial fulfillment
of the requirements for the completion of
Doctor of Philosophy
Department of Atmospheric and Oceanic Sciences
2019

This thesis entitled:
On The Roles of Radiation and Low-Level Vorticity in Numerical Simulations of Tropical Cyclogenesis
written by Warren (Ren) Paul Smith II
has been approved for the Department of Atmospheric and Oceanic Sciences

Dr. Melville Nicholls

Prof. Katja Friedrich

Date _________________

The final copy of this manuscript has been examined by the signatories, and we find that both the content and the form meet acceptable presentation standards of scholarly work in the above mentioned discipline.

Warren (Ren) Paul Smith II, (Ph.D., Atmospheric and Oceanic Sciences)

On The Roles of Radiation and Low-Level Vorticity in Numerical Simulations of Tropical Cyclogenesis

Manuscript directed by Dr. Melville Nicholls

Before a hurricane forms, a process known as tropical cyclogenesis must occur during which a tropical disturbance transforms into a tropical depression. In order to further understand how and when hurricanes will form, we must start by examining the processes that lead to tropical cyclogenesis. This dissertation employs numerical modeling techniques to highlight the roles that both low-level vorticity and longwave and shortwave radiation play in this transformation.

Recent numerical modeling and observational studies indicate the importance of vortical hot towers (VHTs) in tropical cyclogenesis. It has recently been recognized that convective-scale downdraft outflows that form within VHTs also preferentially develop positive vertical vorticity around their edges which is considerably larger in magnitude than ambient values. During a numerical simulation of tropical cyclogenesis it is found that particularly strong small-scale low-level convectively-induced positive vertical vorticity anomalies (herein termed "LCVAs") occasionally form as convection acts on the enhanced vorticity at the edges of cold pools. The LCVAs studied are considerably deeper than the vorticity produced at the edges of VHT cold pool outflows, and their evolution is associated with persistent convection and vortex merger events which act to sustain them. This dissertation highlights the formation and evolution of two representative LCVAs and discusses the environmental parameters which eventually become favorable for one LCVA to reach the center of a larger-scale circulation as tropical cyclogenesis occurs.

Recent literature also indicates the importance of longwave and shortwave radiation in TCG. Herein we examine the sensitivity of TCG to radiation in both idealized simulations for different initial vortex strengths, and in a case study framework of Atlantic Hurricane Matthew (2016) to highlight when during tropical cyclogenesis radiation is most important. It is shown that all else equal, a stronger initial vortex reduces the impact that radiation has on accelerating tropical cyclogenesis. In both modeling frameworks we find that radiation's primary role is to moisten the core of a disturbance, and after sufficient moistening occurs over a deep layer and the winds are sufficiently strong at the surface, radiation no longer plays as significant a role in tropical cyclogenesis.

Dedication

This dissertation is dedicated to my family, friends, colleagues, and everybody in between for providing an endless stream of support along this incredible journey of more than 20 years of education. This milestone could never have been reached without you.

Thank you.

"It's a dangerous business, Frodo, going out your door. You step onto the road, and if you don't keep your feet, there's no knowing where you might be swept off to."

- J.R.R. Tolkien, The Lord of the Rings

Acknowledgements

I would like to give a big thank you to my Ph.D. research advisor Dr. Melville Nicholls of CIRES/ATOC for all of his guidance and support through this long journey. I would also like to thank the rest of my Ph.D. committee members for their willingness to serve on my committee and their helpful questions and comments every step of the way: Drs. John Cassano of CIRES/ATOC, Katja Friedrich of ATOC, Roger Pielke Sr. of CIRES/ATOC, and Gregory Thompson of NCAR. I would also like to thank ATOC Program Assistant Laurie Conway for all of her assistance with department requirements through the different phases of graduate school. Finally, I would like to thank my colleague Robinson Wallace for his help with developing the IDL visualization code used to produce nearly every figure herein and my colleague Dr. Matthew Tooth for proofreading this document.

This work was supported by two NSF Grants: NSF AGS 1445875 and NSF AGS 1415244. I would also like to acknowledge high-performance computing support from Cheyenne (doi:10.5065/D6RX99HX) provided by NCAR's Computational and Information Systems Laboratory, sponsored by the National Science Foundation.

Contents

Chapter

Appendix

Tables

Table

Figures

Figure

Chapter 1

Introduction

1.1 Motivation and Background

Hurricanes are devastating cyclonically rotating storm systems which have tremendous impacts on human life and property on planet Earth. These intense vortices have horizontal circulation diameters on the order of 1000 km and are capable of producing winds in excess of 200 km hr^{-1} (124 mph) resulting in powerful coastal storm surges and heavy precipitation which may move hundreds of kilometers onshore. As such, they have the potential to cause death tolls in the thousands and damage in the tens of billions of U.S. Dollars (Blake and Gibney, 2011). At times, large-scale evacuations are necessary to relocate people to inland locations less susceptible to a devastating hurricane landfall. The severity of hurricanes and their widespread socioeconomic impacts are powerful motivators to study the processes that cause their formation and intensification.

The precursors to hurricanes first appear over the ocean as a cluster of deep convective clouds, otherwise known as a "tropical disturbance." Once convection begins to organize about a surface region of lowered pressure, a tropical disturbance becomes a "tropical depression" through a process known as "tropical cyclogenesis" (hereafter "TCG") (e.g. Sharkov 2011). A tropical depression may then intensify into a tropical storm if the sustained near-surface winds reach 17.5 $m\ s^{-1}$ (at which point it receives a name) and may further intensify into a hurricane or typhoon (this term depends on the ocean basin) once these winds reach 33 $m\ s^{-1}$ (e.g. Elsner et al. 1996). In order to continue to advance our understanding of hurricanes and improve our lead times for large-scale evacuations, we must continue to advance our understanding of TCG.

Some of the first observational work on TCG found that this process is often associated with the presence of easterly waves (Riehl, 1948). These synoptic features have an observed wavelength of approximately 2000 km and a period of 3.2 days (Burpee, 1972). A statistical approach has determined that TCG is favored in regions with sea surface temperatures (SSTs) exceeding 26°C, low vertical wind shear, enhanced low-level vertical vorticity, and at latitudes equatorward of 20° in either hemisphere (Gray, 1968). TCG is the result of several simultaneous processes occurring on different spatial and temporal scales, which presents a challenge for improving our understanding of this process (Ooyama, 1982). Because TCG typically occurs in regions far from land masses where in situ observations are scarce, much of the research in this field is performed with the aid of numerical modeling (Pielke Jr and Pielke Sr, 1997). In this dissertation we discuss two distinct factors which may impact TCG: the presence of radiation and the evolution of low-level vorticity.

1.2 Two Pathways to Tropical Cyclogenesis Emerge

Despite decades of active research, there is still some disagreement about the exact mechanisms through which TCG occurs. Numerical modeling studies with similar frameworks have been able to produce significantly different pathways by which a tropical cyclone (hereafter "TC," this phrase encompasses tropical depressions, tropical storms, and hurricanes) is produced (Montgomery et al., 2006; Nicholls and Montgomery, 2013; Nolan, 2007). Data collected during the Tropical Experiment in Mexico (TEXMEX) inspired numerical simulations with a prescribed mesoscale rain shaft. Using a simple axisymmetric model developed by Rotunno and Emanuel (1987), a mid-level cold-core vortex undergoes gradual subsidence from evaporative cooling in the rain shaft, filling the troposphere with cool, humid air. Once low-level equivalent potential temperature recovers, convection develops which converts the vortex to a warm core and signals TCG has begun (Bister and Emanuel, 1997). This progression describes a "top-down" mechanism by which TCG may occur, since it relies on a mid-level vortex (hereafter "MLV") which eventually manifests into a low-level tropical depression vortex.

The formation of a MLV has been documented in observations and numerical models as a frequent precursor to TCG (e.g. Davis and Ahijevych 2012; Gjorgjievska and Raymond 2014; Kutty and Gohil 2017; Nicholls et al. 2018; Nolan 2007; Reasor et al. 2005; Ritchie and Holland 1997). A study which utilized the Weather Research and Forecasting Model (WRF) version 2.1.1 (Skamarock et al., 2005) undertook several idealized experiments of TCG and noted the formation of a MLV in all frameworks, even when the maximum initialized winds were found at low levels. TCG always coincided with the subsequent formation of a small surface concentrated vortex (SSCV) in the center of the larger-scale circulation (Nolan, 2007). The reason for the formation of a much smaller vortex beneath a MLV was not definitively determined in Nolan (2007), a fact which serves as the motivation for Chapter 2 of this dissertation.

The importance of a MLV in TCG is somewhat challenged by a "bottom-up" TCG paradigm which relies more heavily on deep convective structures to stretch ambient vorticity. The term "vortical hot tower" (hereafter "VHT") has been given to deep, rotating columns of cumulus convection that have been found to exist in both numerical models and observations (e.g. Hendricks et al. 2004; Kilroy and Smith 2013; Montgomery et al. 2006; Sippel et al. 2006). VHTs last for approximately one hour and have height and width scales both on the order of 10 km. VHTs trap heat in their cores and may merge with other VHTs to become a larger axisymmetrized vortex in a so-called "upscale vorticity cascade," a process which promotes TCG (Hendricks et al., 2004). These convective structures provide protected environments for the conversion of latent heat into rotational momentum (Montgomery et al., 2006). A larger-scale circulation (radius of order 100 km) may protect a developing tropical disturbance from the lateral entrainment of dry air, which favors convection (Dunkerton et al., 2009). In the absence of such a closed circulation, dry air may intrude the core of the disturbance and suppress convection, which inhibits TCG from occurring (Raymond and López Carrillo, 2011). The reliance of these paradigms on deep convection distinguishes them from the aforementioned “top-down” pathway to TCG.

Recognizing that different paradigms for TCG exist in the literature, an extensive modeling study was undertaken to further the understanding of these competing theories (Nicholls and Montgomery, 2013). Using one modeling framework, two distinctly different pathways to TCG were observed depending on the initial conditions employed. The VHT axisymmetrization mechanism introduced in Hendricks et al. (2004) and further examined in Montgomery et al. (2006) was termed “Pathway One” while the MLV and subsequent formation of an SSCV explored by Nolan (2007) was termed “Pathway Two.” Simulations with a more robust ice phase were found to favor development along Pathway Two as they favor the formation of a MLV. This pathway typically produces smaller TCs and appears to be more favored in environments with low vertical wind shear. In addition to showing that two different pathways are plausible, the authors also noted that the timing of TCG is very sensitive to the chosen radiation scheme, and that withholding radiation entirely is detrimental to TCG (Nicholls and Montgomery, 2013).

1.3 The Role of Radiation

It has been shown in numerous studies that tropical convection exhibits a diurnal cycle (e.g. Fingerhut 1978; Gray and Jacobson Jr 1977; Jacobson and Gray 1976; Kraus 1963). It is thought that clear-sky nighttime radiative cooling promotes an early morning maximum in convection, after which convection tapers off as the sun rises (Gray and Jacobson Jr, 1977). This mechanism has been shown to be important on different scales of tropical convective activity, including the intensification of tropical mesoscale convective systems (MCSs, Dudhia 1989; Miller and Frank 1993).

TCG has also shown a dramatic sensitivity to longwave and shortwave radiation (hereafter just “radiation” unless otherwise noted) in recent numerical modeling studies (Melhauser and Zhang 2014; Nicholls 2015; Nicholls and Montgomery 2013; Tang and Zhang 2016). This has been shown to be true regardless of the TCG development pathway a numerical simulation evolves along (Nicholls and Montgomery 2013, see the discussion of pathways above in Section 1.2). Radiation promotes nocturnal environmental destabilization in a developing disturbance's surroundings, promoting deep moist convection which accelerates TCG (Melhauser and Zhang, 2014).

Idealized simulations performed with the Regional Atmospheric Modeling System (RAMS, Pielke et al. 1992) indicate the importance of radiation on increasing relative humidity (RH) and surface cyclonic circulation in a tropical disturbance as well as modifying static stability. Differential radiative forcing between a cloudy disturbance and its surrounding clear-sky region drives a weak nocturnal transverse circulation (velocity on the order of millimeters per second) which slowly moistens the core, thereby promoting convection in the early morning hours (Nicholls, 2015). This finding is consistent with early observational work by Gray and Jacobson Jr (1977) who noted this mechanism is important for organized convective clouds, and that precipitation in tropical regions experiences an early morning maximum.

In addition to affecting the intensity of a developing storm, the track of a storm is also sensitive to radiation, as demonstrated in a case study of a real hurricane (Tang and Zhang, 2016). After TCG, the presence of cloud radiative forcing (CRF), or the interaction between radiation and hydrometeors, leads to stronger outer-core winds and upper-tropospheric outflow by enhancing convection, as shown by a study that employed Hurricane WRF (HWRF, Gopalakrishnan et al. 2012) to run semi-idealized simulations (Bu et al., 2014). There is some disagreement in numerical modeling about how important radiation becomes after TCG. A study by Nicholls (2015) found that radiation may accelerate the time it takes for a tropical depression to intensify into a tropical storm, whereas Craig (1996) found that radiation has little effect after TCG. Chapter 3 of this dissertation explores the importance of radiation on both TCG and early intensification and comments on this issue. The sensitivity of TC formation, structure and intensity to radiation inspires further research to ensure that the modeling of TCG accurately accounts for the role of radiation.

1.4 Project Summary and Overview

This dissertation has resulted in three first-author publications; one of these has been accepted for publication at the Journal of the Atmospheric Sciences (JAS), another is currently in review at JAS, and another is in preparation for submission in the fall of 2019. These three papers are briefly summarized below and comprise Chapters 2, 3 and 4 of this document, respectively. The evolution of low-level vorticity anomalies was presented at the American Geophysical Union 2016 Fall Meeting in San Francisco, California and won an award for best poster in the "Aerosols, Clouds and Precipitation" category at the 2016 Earth System and Space Science (ESSS) poster conference in Boulder, Colorado. The role of radiation in simulations of TCG was presented at the 33rd Conference on Hurricanes and Tropical Meteorology in Ponte Vedra, Florida and won an award for best poster in the "Boundary Layer and Wind Energy" Category at the 2018 ESSS Poster Conference in Boulder, Colorado. In addition, four coauthor publications have resulted from this work (Nair et al., 2019; Nicholls et al., 2018, 2019a,b). Relevant contributions to two of these publications are briefly discussed in Chapter 5.

This investigation explores the impacts that low-level vorticity and longwave and shortwave radiation have on TCG. The following science questions are specifically addressed along the way:

(1) **By what processes does the small surface concentrated vortex first introduced by Nolan (2007) form, and how does it evolve prior to its appearance in the center of a larger-scale circulation as tropical cyclogenesis occurs?**

In "Pathway Two" from Nicholls and Montgomery (2013), an SSCV appears in the center of a larger-scale circulation as TCG is about to begin. Chapter 2 focuses on exploring the formation of low-level convectively-induced vorticity anomalies (LCVAs) which form sporadically prior to TCG in an idealized simulation. Eventually, one LCVA reaches the center of the larger-scale circulation and takes the form of the SSCV from Nolan (2007). It is shown that LCVAs form from vertical vorticity that is stretched at the edges of shallow surface cold pools that transform from "shear" to "curvature" vorticity during new convection. As LCVAs propagate about the disturbance center, they undergo vortex mergers with other low-level vorticity sources in the domain. As a simulation evolves, additional convection promotes more low-level vorticity sources, which is likely to favor an LCVA reaching the center of the larger-scale circulation.

(2) **At what stage of a tropical disturbance's development is the presence of longwave and shortwave radiation most influential?**

TCG is very sensitive to the presence of radiation (e.g. Nicholls 2015), however there has been little exploration into when radiation is most influential during this process. Chapter 3 explores the role of radiation in idealized simulations of TCG, utilizing three different initial MCVs of varying strength. It is shown that the stronger a vortex and the moister the core of the disturbance is, the less important radiation is in influencing the timing of TCG. Otherwise identical simulations with and without radiation show that radiation dramatically accelerates deep moistening in the core of the disturbance, which is consistent with the transverse circulation mechanism first introduced by Nicholls (2015). Once a vortex is sufficiently strong and moistened into the upper troposphere, radiation no longer plays a meaningful role in determining the timing of TCG.

(3) **How does radiation impact the development of a real Atlantic hurricane?**

Idealized simulations indicate the importance of radiation in TCG, however it is natural to wonder if this sensitivity exists for real hurricanes. Chapter 4 performs a case study of Atlantic Hurricane Matthew (2016) which made landfall in Haiti, Cuba and the United States in October 2016. Simulations which begin about 3 days prior to the genesis of Matthew indicate that Matthew does not exhibit the sensitivity to radiation that is expected from the literature. It is hypothesized that this is because the core of the vortex is already too moist when the simulation begins, which as suggested by Chapter 3 means that radiation does not thereafter play a meaningful role in TCG.

This paper is divided into six chapters. Chapter 1 provides the motivation and necessary background to frame the forthcoming research questions, as well as a summary of the exploration that follows. Chapter 2 explores low-level convectively-induced vorticity anomalies (LCVAs) in an idealized numerical simulation. Chapter 3 explores the role that radiation plays in idealized simulations of TCG with a goal to identify the key processes that radiation is responsible for, as well as when radiation is most important. Chapter 4 performs a case study simulation of Atlantic Hurricane Matthew (2016) to understand the importance of radiation on more complex real-world simulations. Chapter 5 provides some relevant contributions to coauthor papers and serves to reinforce the analysis and conclusions provided in Chapters 2, 3 and 4. Chapter 6 summarizes all of the main findings and provides directions for future research. Several appendices are also included: a description of hydrostatic and cyclostrophic balance, surface-based convective available potential energy (SBCAPE), and methods for calculating the curvature vorticity budget equation performed for LCVAs [Chapter 2], edits to the vertical structure of the initial vortex winds and the moisture profile and a discussion of ensemble simulations for idealized WRF simulations [Chapter 3], and a page of acronyms for reference.

Chapter 2

On the Creation and Evolution of Small-Scale Low-Level Vorticity Anomalies During Tropical Cyclogenesis

In this chapter we explore an idealized numerical simulation which highlights the generation of enhanced low-level vertical relative vorticity and its subsequent importance in TCG. This chapter is adapted from Smith and Nicholls 2019 (full citation given below). The reader is also directed to Sections 5.1 and 5.2 which feature coauthor contributions to Nicholls et al. (2019b) for additional information on vorticity generation around cold pools and the formation of LCVAs.

Smith, W. P. and Nicholls, M. E. (2019), 'On the creation and evolution of small scale low level vorticity anomalies during tropical cyclogenesis (accepted for publication)', Journal of the Atmospheric Sciences. doi: 10.1175/JAS-D-18-0104.1

2.1 Introduction

Hurricanes are powerful cyclonically rotating systems which lead to widespread destruction in coastal areas every year. An important early stage in the formation of a hurricane is the transformation from a tropical disturbance to a tropical depression, a process known as tropical cyclogenesis (TCG). TCG is difficult to predict because it is governed by many simultaneous kinematic and thermodynamic processes occurring at different spatial and temporal scales which are not well understood. Such processes include the development of mid-level vortices (MLVs, horizontal scale of order 100 km) that may persist for several days and rotating convective towers (horizontal scale of order 10 km) that may persist for a few hours. A possible path to TCG has recently been proposed which states that after a MLV forms in a tropical disturbance, a much smaller convective-scale vortex may arrive in its center which subsequently develops rapidly into a tropical cyclone (TC, e.g. Nicholls and Montgomery 2013; Nolan 2007). The current work investigates the origin of such small vortices and what conditions might be favorable for one to propagate to the center of the larger-scale circulation.

MLVs have often been observed and modeled as a precursor to TCG (e.g. Bister and Emanuel 1997, Raymond and López Carrillo 2011, Davis and Ahijevych 2012, Kutty and Gohil 2017, Nicholls et al. 2018), and their formation has been associated with the sudden appearance of a small surface concentrated vortex (SSCV) in its center which then becomes the low-level core of an intensifying TC (Nolan, 2007). In the simulations performed by Nicholls and Montgomery (2013) it was noted that these smaller vortices typically originate tens of kilometers from the larger-scale center rather than forming there. Why these convective-scale vortices behave as they do has prompted calls for more modeling studies in order to further our understanding of how they might contribute to TCG (Fang and Zhang, 2011).

Beneath a MLV, rotating convection has been shown to be an important contributor to TCG (e.g. Hendricks et al. 2004, Montgomery et al. 2006, Fang and Zhang 2011). The term “vortical hot tower” (VHT) has been coined to describe convective-scale rotating cells which span the depth of the troposphere and last for approximately one hour as they propagate within a larger-scale circulation prior to TCG (Hendricks et al., 2004). VHTs provide a protected environment for efficient conversion of latent heat into rotational momentum and can merge with other VHTs to become stronger (Montgomery et al., 2006). A larger-scale circulation can protect a developing disturbance from the lateral entrainment of dry air which would otherwise inhibit moist convection from occurring (Dunkerton et al., 2009;

Raymond and López Carrillo, 2011). This VHT "pathway" to TCG is somewhat distinct from the aforementioned MLV hypothesis because it relies on rotating convective-scale structures which provide enhanced vertical vorticity for the eventual formation of a larger-scale tropical depression. A modeling study by Nicholls and Montgomery (2013) showed that both the VHT mechanism (Hendricks et al., 2004; Montgomery et al., 2006) and the MLV with an SSCV mechanism (Nolan, 2007) manifested in the same numerical modeling framework depending on the initial conditions employed.

Like other forms of tropical deep convection, VHTs produce cold pools from precipitating downdrafts which spread at the surface (e.g. Eastin et al. 2012), and discrete convective towers often form downshear of such cold pools (Davis, 2015). Cold pools produced in this way tend to be shallow (with depths of just a few hundred meters) and often generate positive vorticity at the edge of their spreading outflow which could promote the development of discrete vortices if acted upon by additional convection (Nicholls and Montgomery, 2013). The term "convectively induced vorticity anomalies" (CVAs) has been given to tropical rotating vortices of different sizes and origins, which are often building blocks for larger scales of rotation (Fang and Zhang, 2011). We choose to add a "low-level" modifier to this acronym by distinguishing smaller vortices at the edges of cold pools from VHTs, as we hypothesize they can contribute to TCG in fundamentally different ways.

The present study focuses on the life cycle of strong low-level convectively-induced vorticity anomalies (LCVAs) that form sporadically and propagate cyclonically for up to 8 hours in a numerical simulation prior to TCG. We show that eventually the background conditions of the tropical disturbance become favorable for one LCVA to move into the center and become the low-level core of an intensifying TC, in a manner analogous to the "appearance" of an SSCV in the work of Nolan (2007). This study focuses on exploring two such LCVAs in a numerical simulation: one that dissipates about 8 hours after its formation (which we term the "early LCVA") and one that eventually moves into the center of the larger-scale circulation as TCG occurs (which we term the "genesis LCVA"). A vorticity budget is performed on the formation of an LCVA to show that they form as convection acts upon enhanced regions of vorticity at the edges of cold pools. Insights are made into the presence of shear and curvature vorticity in the formation of LCVAs and the presence of vortex merger events is examined during their life cycle. In doing so, the present understanding of the mechanisms by which these vortices form is improved and insight is provided for the background conditions that allow for increased longevity of LCVAs as time progresses.

The remainder of this paper is organized as follows. The next section describes the numerical model setup. Section Three discusses the formation, development and dissipation mechanisms of LCVAs. Section Four discusses the concept of shear and curvature vorticity and Section Five tests the hypothesis that vortex mergers are occurring which strengthen LCVAs. Discussion and conclusions are given in Sections Six and Seven. Appendices pertaining to cyclostrophic and hydrostatic balances, the presence of surface-based convective available potential energy (SBCAPE) in LCVAs, and a friction estimation for the curvature vorticity budget are also included.

2.2 Numerical Model and Methods

Because TCG typically occurs in areas that are far from land masses, much of the research in the field is performed with the aid of numerical modeling (Pielke Jr and Pielke Sr, 1997). The environments that TCs form in are often complex, and for simplicity many numerical modeling studies have examined development in idealized conditions. Probably the most canonical model configuration is one without any ambient winds, that has a favorable thermodynamic environment with a conditionally unstable troposphere overlying a warm ocean surface, and which is initialized with a weak mesoscale vortex (such as that used in Nicholls and Montgomery 2013).

The Regional Atmospheric Modeling System (RAMS) Version 4.3 (Cotton et al., 2003; Pielke et al., 1992) is employed for the simulation presented in this study. RAMS is a three dimensional nonhydrostatic numerical modeling system which uses time dependent equations for velocity, nondimensional pressure perturbation, ice-liquid water potential temperature (Tripoli and Cotton, 1981), total water mixing ratio, and cloud microphysics. The microphysics parametrization explicitly calculates rain, cloud water, pristine ice, snow, aggregates, graupel, and hail mixing ratios (Meyers et al., 1997; Walko et al., 1995). The simulation analyzed in this study is the same as that discussed in Nicholls et al. (2018) who instead analyzed the formation and evolution of a MLV. The reader is directed to their Figure 1 for a broad overview of how this simulation evolves. Below we restate how this simulation is initialized.

The analyzed simulation is initiated with the hurricane sounding from Jordan (1958) which is slightly dried at low levels (as discussed in Nicholls and Montgomery 2013). Potential temperature perturbations in this work are calculated as the deviation from this horizontally homogeneous initial sounding. The simulation is initialized with a broad vortex with peak wind speeds of 8 $m\ s^{-1}$ at a height of 4 km and a radius of maximum winds (RMW) of 75 km (not shown). In all of this paper's figures, the point x = 0 km, y = 0 km is defined as the center of this larger-scale vortex with positive (negative) values of x and y lying to the east and north (west and south), respectively.

The Sea Surface Temperature (SST) is set as a constant 28°C in this simulation, which is a typical value in the tropics during hurricane season and is favorable for TCG (Gray, 1968). For simplicity, the Coriolis Force is approximated using an f-plane at a latitude of 15°N. The model domain is initially devoid of any liquid or solid water, and no longwave or shortwave radiation schemes are employed. Sub-grid scale turbulence is parametrized according to deformation-K closure found in Smagorinsky (1963) with stability modifications from Lilly (1962) and Hill (1974).

The simulation contains three co-centric grids which have horizontal grid spacings of 12 km (170x170 points), 3 km (202x202 points), and 1 km (302x302 points). All 3 grids have 47 vertical levels which are vertically stretched from the lowest model level at 29.5 m above ground level (AGL) to the top at approximately 23 km AGL. A Rayleigh damping layer is added to suppress gravity waves from reaching the model top, which begins at a height of 15.2 km AGL. Only output from the finest (1 km spacing) grid is considered in the following analysis.

The vertical component of relative vorticity (hereafter just “vorticity”) and horizontal divergence (hereafter just “divergence”) are computed, respectively, by:

$$\zeta = (\nabla \times \vec{u}) \cdot \hat{k} = \frac{\partial v}{\partial x} - \frac{\partial u}{\partial y} \tag{2.1}$$

$$\delta_h = \nabla_h \cdot \vec{u_h} = \frac{\partial u}{\partial x} + \frac{\partial v}{\partial y} \tag{2.2}$$

In the next section we perform a vorticity analysis on the formation of the early LCVA using the material form of the vertical vorticity budget equation with friction neglected:

$$\frac{\partial \zeta}{\partial t} = -(\vec{u} \cdot \nabla)\zeta - \delta_h(f + \zeta) - \left(\frac{\partial w}{\partial x}\frac{\partial v}{\partial z} - \frac{\partial w}{\partial y}\frac{\partial u}{\partial z} \right) + \frac{1}{\rho^2}\left(\frac{\partial \rho}{\partial x}\frac{\partial p}{\partial y} - \frac{\partial \rho}{\partial y}\frac{\partial p}{\partial x} \right) \tag{2.3}$$

where $\vec{u} = \langle u, v, w \rangle$ is the three dimensional wind vector where u, v, and w are the zonal, meridional and vertical components of the wind, respectively, $f = 2\Omega sin(\phi)$ is the Coriolis parameter for Earth’s angular velocity $\Omega = 7.29 \times 10^{-5} s^{-1}$ and latitude ϕ, ρ is the air density and p is the pressure.

The term on the left side of Equation 2.3 is the Eulerian derivative of vorticity with respect to time. The first term on the right hand side represents advection and the second term is the stretching term, which describes vorticity changes from horizontal convergence and divergence. The third term on the right side of Equation 2.3 is the tilting term, which describes the conversion of horizontal vorticity into vertical vorticity through horizontal gradients of vertical velocity. The final term is the baroclinic (or “solenoid”) term, which describes the production of vorticity through a comparison of horizontal gradients in density and pressure.

Because RAMS uses Arakawa-C grid staggering (Arakawa and Lamb, 1977), wind fields are first linearly interpolated onto the same points as the thermodynamic variables before computations are performed. Partial derivatives are then calculated at each point using the adjacent grid points in the appropriate dimension.

2.3 Analysis of LCVAs

In this section, we describe the formation and intensification of two distinct LCVAs that propagate through the domain prior to TCG. These LCVAs are fundamentally different than VHTs in that they have maximum vorticity near the surface, rather than at mid-levels which was suggested by Figure 5 of Hendricks et al. (2004). The first LCVA analyzed is termed the "early LCVA" because it forms and dissipates long before TCG occurs. The other LCVA is termed the "genesis LCVA" because it does eventually reach the center of the larger-scale circulation, an event that coincides with the timing of TCG. The spatial propagation and intensity evolution of both these LCVAs is shown in Figure 2.1. It is important to note that these two LCVAs are not the only two that exist in the simulation, but these two are selected as representative in order to simplify the forthcoming analysis. Analyzing how these LCVAs form and how they interact with their surrounding environments gives clues as to how it is eventually conducive for an LCVA to reach the center of the larger-scale circulation.

2.3.1 The Early LCVA

Figure 2.1a shows the early LCVA's horizontal track and a time series of its intensity from 43 to 52 hour run time. The tracks in this figure are produced by subjective selection of the vorticity maximum in the LCVA. LCVAs move counterclockwise along with the cyclonic flow of the larger scale vortex (discussed in Section 2.2). The early LCVA first is distinguishable as a quasi-circular region of enhanced vorticity at the edge of a cold pool, shown in Figure 2.2a. Panel 2d shows the location of the cold pool to its southeast. This cold pool is roughly 300 m deep, which is a representative depth for this simulation (not shown). The

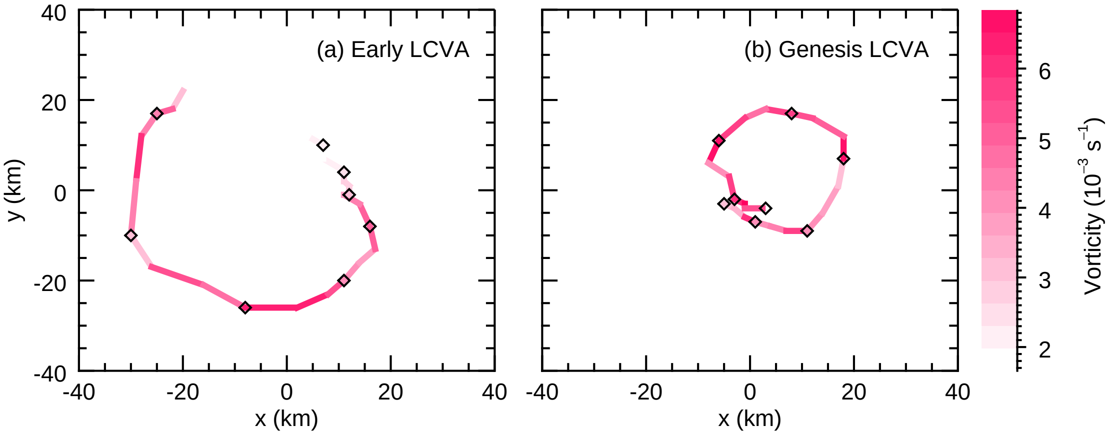

Figure 2.1: Horizontal motion of the (a) early LCVA from 43 hours and 20 minutes to 51 hours and 20 minutes run time and (b) the genesis LCVA from 83 hours to 90 hours run time. Each line segment represents motion over a 20 minute period, and the color of each segment shows the average value of ζ (10^{-3} s^{-1}) calculated in a 2 km x 2 km grid box centered on the LCVA at the lowest model level (z = 29.5 m AGL). Black diamond symbols represent the location of the LCVA at every hour (on the hour) to give information about propagation speed. Tracks are defined by a subjective selection method of the low-level vorticity maximum at each time step.

strongest convective cold pools in this simulation have potential temperature depressions of about 4 K, consistent with other observational and modeling studies in tropical environments (Drager and van den Heever, 2017; Eastin et al., 2012).

In Figure 2.2, the edge of the cold pool is marked by enhanced vorticity (panel a), enhanced convergence (negative divergence in panel b) and therefore an enhanced stretching term in panel g. This mechanism tends to create positive vorticity at the edges of cold pools because the ambient vorticity inside the RMW is generally positive. The vertical velocity field in panel c indicates that deep convection is associated with the LCVA at this time. The convective column is tilted towards the south (by comparison of the filled and black contour fields) indicating that the convective downdraft does not impede convection from continuing to act on the LCVA. By comparing all terms contributing to vorticity changes (Figure 2.2e-i), it can be seen that the stretching term and horizontal advection are the dominant terms in Equation 2.3. Convection acts to stretch even more vorticity in the column as time progresses. This analysis suggests that shallow vorticity at the edges of cold pools can be stretched to produce vortices by updrafts in convective cells and that these vortices may become more intense from the vorticity present in their surroundings.

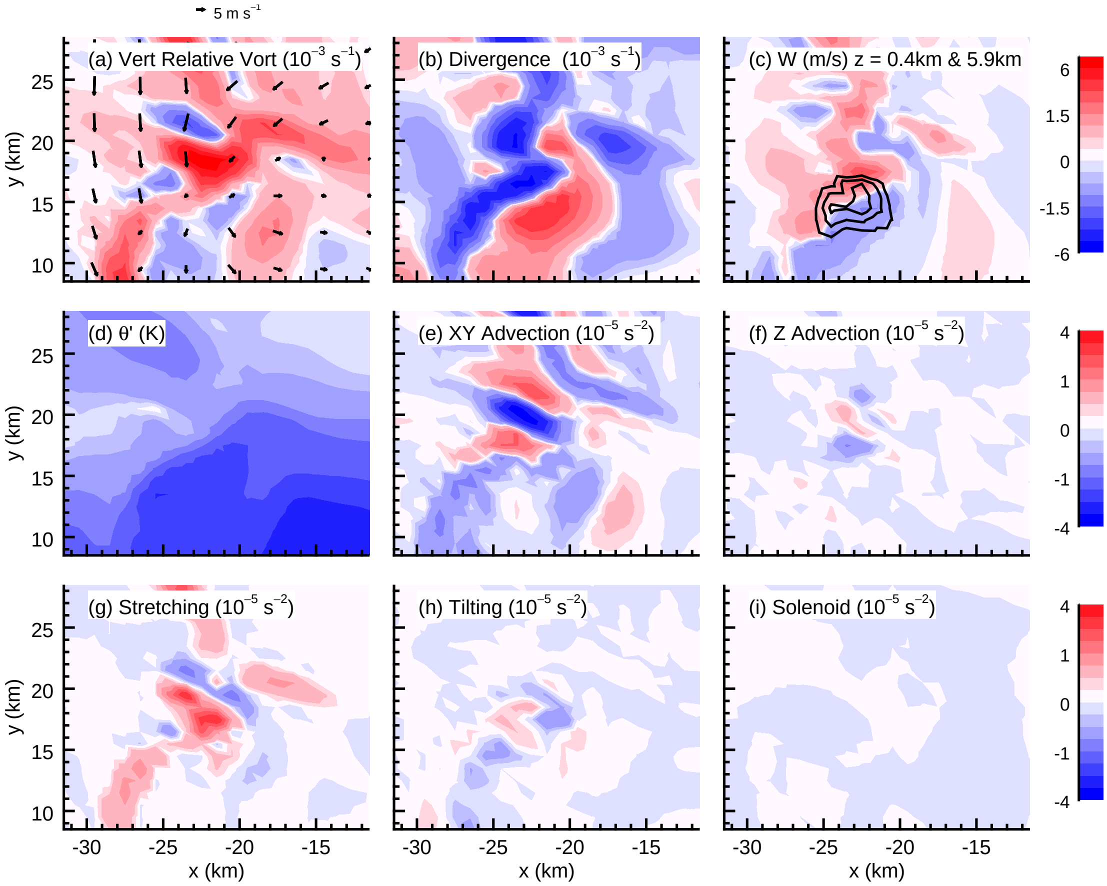

Figure 2.2: Horizontal cross sections of (a) vertical vorticity with horizontal wind vectors, (b) horizontal divergence, (c) vertical velocity, (d) perturbation potential temperature, and the (e) horizontal advection, (f) vertical advection, (g) stretching, (h) tilting, and (i) solenoid terms from Equation 2.3 at a model run time of 43 hours and 40 minutes. All fields are taken at the lowest model level (z = 29.5 m AGL) except panel (c), which shows vertical velocity at z = 0.4 km (fill) and 5.9 km (black lines, which have contour levels of 4, 8, and 12 $m\ s^{-1}$) AGL. Vorticity and divergence are scaled by a factor of $10^3\ s^{-1}$ and all terms from Equation 2.3 are scaled by a factor of $10^5\ s^{-2}$.

Figure 2.3 shows horizontal and vertical cross sections of the early LCVA at 46 hours. The early LCVA is being acted on by convection which causes it to grow from shallow vorticity at the edge of a cold pool (depth of about 500 m) to about 6 km deep (panel a).

This vorticity is on the order of 10^{-2} s^{-1}, which is considerably higher than background values, an observation consistent with the discussion of intense rotating convection in Davis (2015). In the horizontal, the LCVA occupies approximately 10 km x 5 km near the surface (panel c). There are no significant cold pools visible near the LCVA at this time (panel d), but deep convection is present on its west side as evidenced by the vertical cross section of total hydrometeor mixing ratio (panel b).

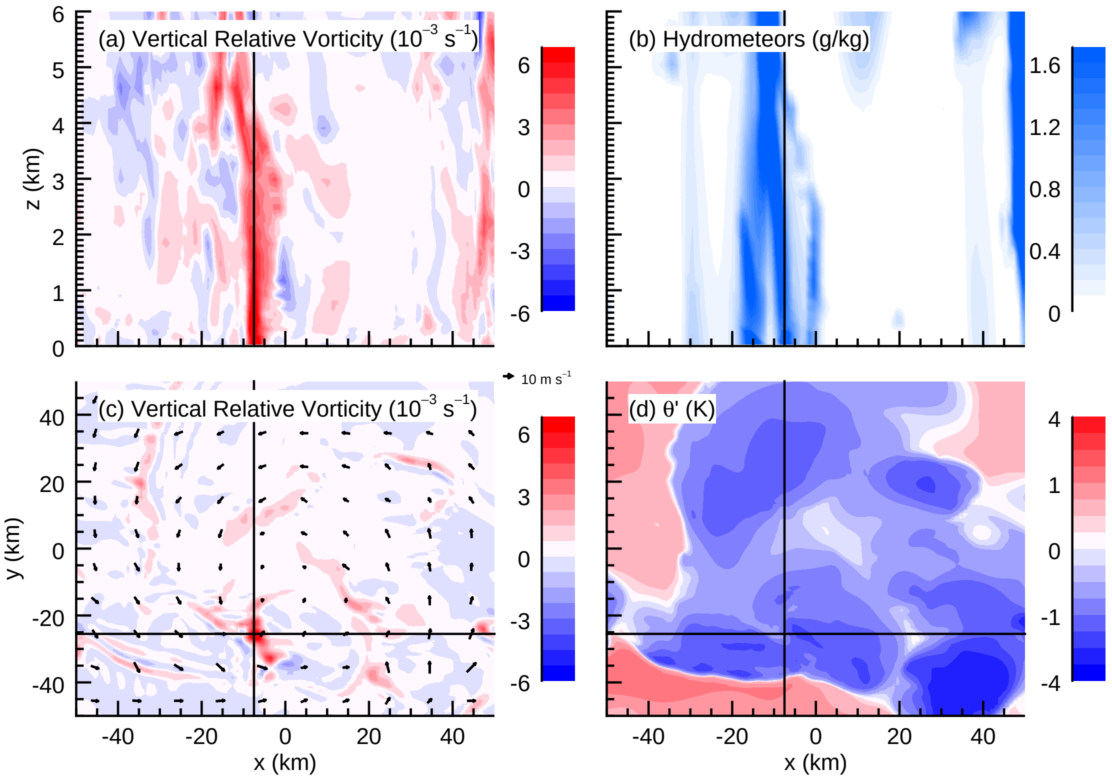

Figure 2.3: Vertical cross sections of (a) vertical vorticity and (b) total liquid and ice hydrometeor mixing ratio and horizontal cross sections of (c) vertical vorticity with horizontal wind vectors and (d) perturbation potential temperature taken at the lowest model level ($z = 29.5$ m AGL) at a model run time of 46 hours. Vertical cross sections are taken through the horizontal lines in the horizontal cross sections. Vertical lines are in the same location in all plots for reference only. Vorticity fields are scaled by a factor of 10^3 s^{-1}.

Figure 2.4 shows the same cross sections as in Figure 2.3, except 3 hours and 40 minutes later at 49 hours and 40 minutes. The early LCVA has weakened remarkably and now only extends to about 2 km AGL (panel a). Convection is absent near the LCVA (panel b) which prevents it from retaining its former depth, and its vorticity is drawing closer to ambient values of about $10^{-3}\ s^{-1}$ (panel c). Two new cold pools are now evident, centered at approximately (37 km, 20 km) and (-25 km, -17 km) (panel d). Both cold pools contain noteworthy enhancements in vorticity nearby which are now stronger than the early LCVA. LCVAs continue to develop and dissipate in a similar fashion as the simulation progresses, until the background conditions eventually become conducive for the genesis LCVA to reach the center about 40 hours later.

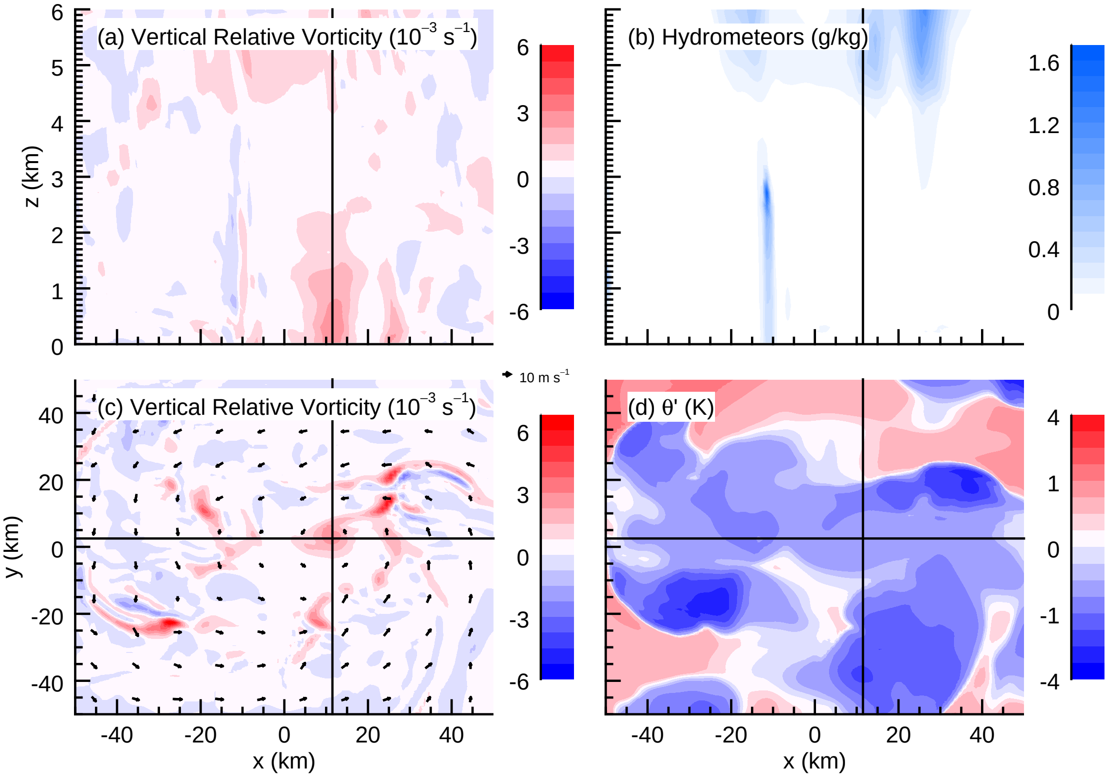

Figure 2.4: As in Figure 2.3, but at a model run time of 49 hours and 40 minutes.

2.3.2 The Genesis LCVA

We now move ahead in time to examine another LCVA which eventually reaches the center of the domain and intensifies, which we term the "genesis LCVA." Figure 2.1b shows the track and intensity of the genesis LCVA from 83 hours through TCG at 90 hours. Figure 2.5 shows its birth, illustrated by low-level cross sections of vorticity and perturbation potential temperature. At about 82 hours, two cold pools form very near to each other (panel b). As these two cold pools mature (panel d) they create particularly strong vorticity along their interface brought about by stretching from opposing outflow directions (panel c, and as in Figure 2.2 for the early LCVA). This interaction spurs deep convection, which concentrates vorticity into a column and leads to the formation of the genesis LCVA (panel e).

Figure 2.6 shows vertical cross sections of vertical velocity and vorticity at various times through the center of the genesis LCVA, illustrating its development and intensification. Figure 2.6a shows a shallow region of enhanced vorticity which is present at the edge of a convective cold pool (similar to that shown in Figure 2.2 for the early LCVA). To its east in panels a and b, the remnants of the VHT that created the cold pool are still visible. This enhanced vorticity suddenly deepens to about 6 km AGL when acted upon by convection 40 minutes later (panels c and d). Convection continues to act on the LCVA throughout its life cycle (panels e and f) until finally it is able to reach the center of the larger-scale circulation (panels g and h), when TCG occurs (as evidenced by a rapid climb in tangential winds and rapid decrease of surface pressure beginning at this time). After this time, the LCVA continues to intensify and the pressure begins to drop as the low-level vortex transforms into a tropical depression. The rapid regeneration of surface-based convective available potential energy (SBCAPE) favors persistent convection throughout the genesis LCVA's life cycle (see Appendix B).

The bend in the convective column in Figures 2.6d and 2.6f is the result of local vertical wind shear from a strong MLV that develops in this simulation (Nicholls et al., 2018). This

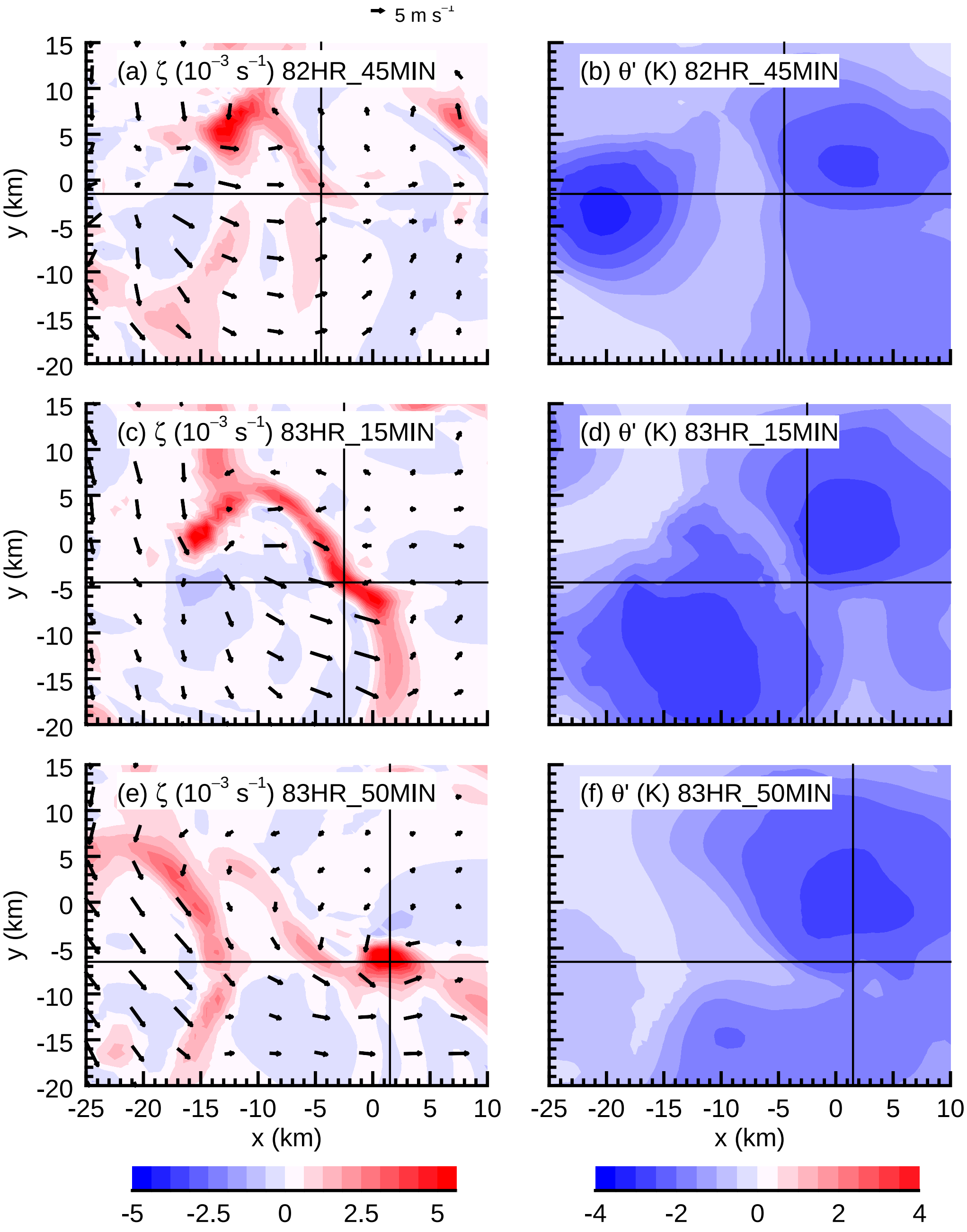

Figure 2.5: Horizontal cross sections of (left) vertical vorticity with horizontal wind vectors and (right) perturbation potential temperature taken at the lowest model level (z = 29.5 m AGL) at (a,b) 82 hours and 40 minutes, (c,d) 83 hours and 15 minutes, and (e,f) 83 hours and 50 minutes. The crosshairs in each plot mark the genesis LCVA. Vorticity fields are scaled by a factor of $10^3 s^{-1}$.

is illustrated more explicitly in Figure 2.7, which shows vertical cross sections at 86 hours

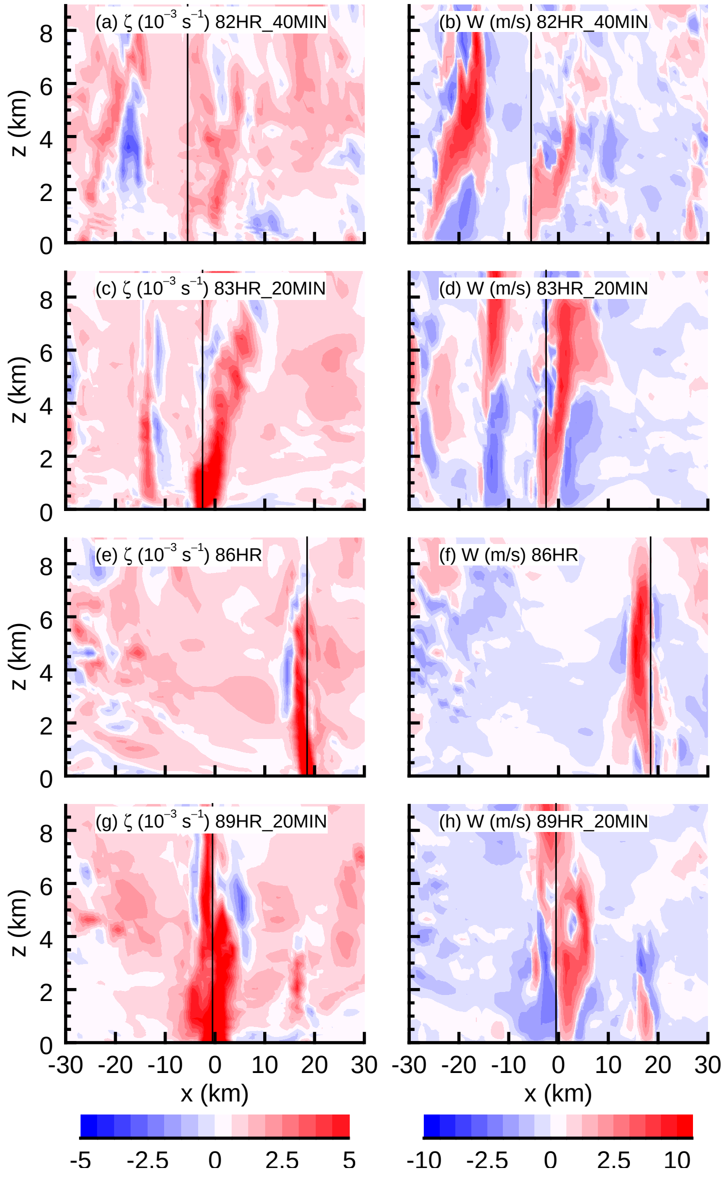

Figure 2.6: Vertical cross sections of (left) vertical vorticity and (right) vertical velocity taken through the center of the genesis LCVA at (a,b) y = 0.5 km at 82 hours and 40 minutes, (c,d) y = -3.5 km at 83 hours and 20 minutes, (e,f) y = 7.5 km at 86 hours, and (g,h) y = -2.5 km at 88 hours and 40 minutes. The vertical lines in each plot mark the center of the LCVA at the surface. Vorticity fields are scaled by a factor of $10^3 s^{-1}$.

and 20 minutes. A strong MLV (between 4 km and 6 km AGL) can be seen in panel b which causes some local vertical wind shear, thus tilting the column of vorticity (panel a). This vertical shear promotes updrafts and downdrafts to not be collocated (panels c and d), which may increase the average lifetime of a convective tower. Therefore we hypothesize that the strengthening and contraction of the MLV throughout the simulation is conducive to longer lasting and stronger LCVAs by promoting vertically tilted convective columns which are sustained longer. This same mechanism was briefly mentioned in Appendix A of Nicholls and Montgomery (2013).

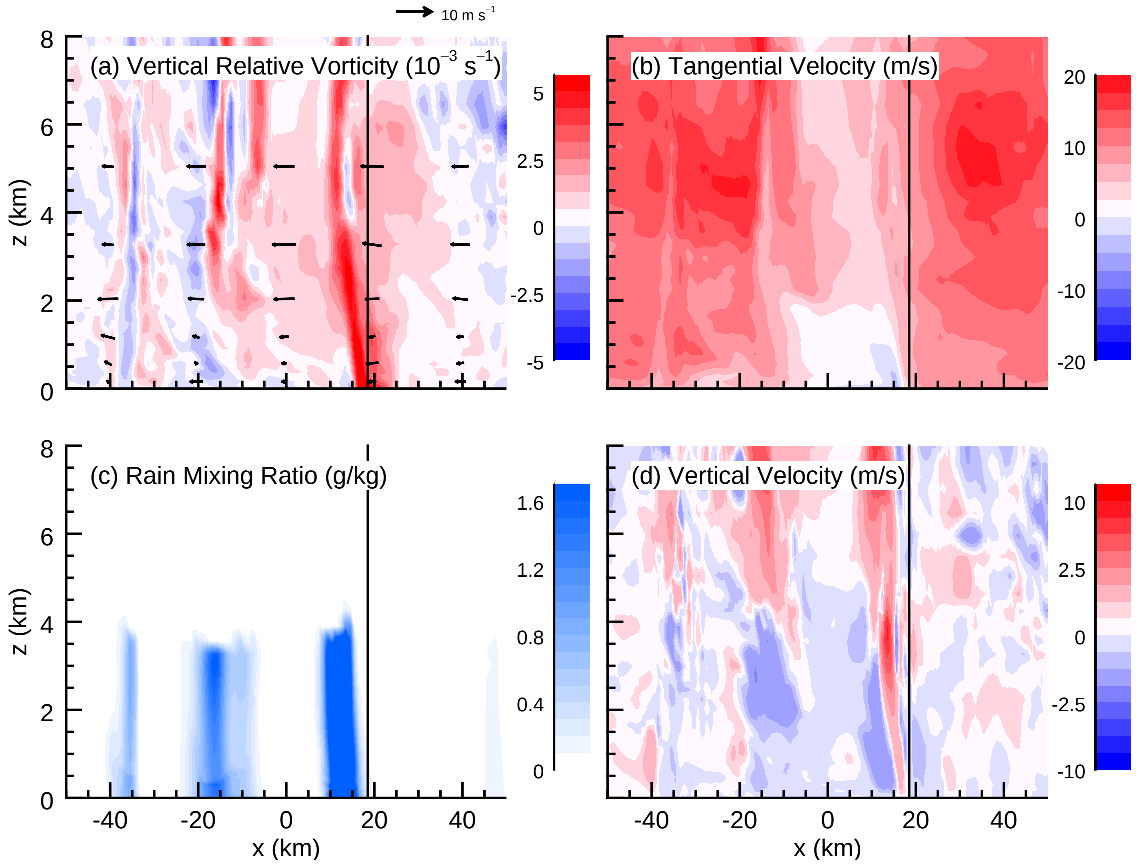

Figure 2.7: Vertical cross sections of (a) vertical vorticity with zonal/vertical wind vectors, (b) tangential wind, (c) rain mixing ratio, and (d) vertical velocity taken at y = 12.5 km (through the center of the genesis LCVA) at a model run time of 86 hours and 20 minutes. Tangential wind is calculated relative to the model center, with positive values indicating cyclonic motion. This means that values to the east (west) of the center are going into (out of) the page in panel b. Vorticity is scaled by a factor of $10^3 s^{-1}$.

Throughout the evolution of both the early and genesis LCVAs, a spatially coincident region of lowered pressure (maximum depression around 2 hPa from the surroundings) exists and synchronously strengthens and weakens with the LCVAs. This pressure drop for the genesis LCVA is illustrated in Figure 2.8, which shows horizontal cross sections of vorticity and pressure perturbation at two times 20 minutes apart. Between the two time steps, convection acts on the genesis LCVA which causes it to intensify at the surface (panels a and c). Consequently, the pressure depression increases slightly and its horizontal extent is reduced to match that of the genesis LCVA (panels b and d). This same process can be seen in the early LCVA as well, but is not shown in the interest of brevity. Pressure depressions are persistent features in LCVAs and are a likely catalyst for promoting TCG when an LCVA reaches the center, as this begins the fall of the central surface pressure.

Figure 2.9 shows the same fields as in Figure 2.3, except at a model run time of 90 hours, when TCG occurs. At this time the genesis LCVA is very strong and reaches the center of the larger-scale circulation. The vorticity maximum is found along the edge of a central cold pool which likely forms from convective precipitation falling out downshear of the LCVA (see Figure 2.7). Vorticity at the edge of this cold pool may also contribute to the strengthening of the LCVA as it moves toward the center of the larger-scale circulation. At this time the genesis LCVA is now analagous to the SSCV from Nolan (2007) that signals TCG is occurring.

We show that LCVAs in this simulation first appear as shallow vorticity signatures at the edges of cold pools which come about from the horizontal wind shift between their convective outflow and the ambient vortex (Figures 2.2 and 2.5). The subsequent presence of convection allows for the concentration of vorticity into a more circular column. These two states represent “shear” and “curvature” vorticity, respectively (Saucier, 1955). In the next section, we break down the vorticity field into these components and analyze how curvature vorticity in LCVAs can form from shear vorticity at the edges of cold pools.

2.4 Shear and Curvature Vorticity

In this section, we examine the formation of shear vorticity at the edges of cold pools and its subsequent conversion to curvature vorticity as LCVAs form. In particular we focus

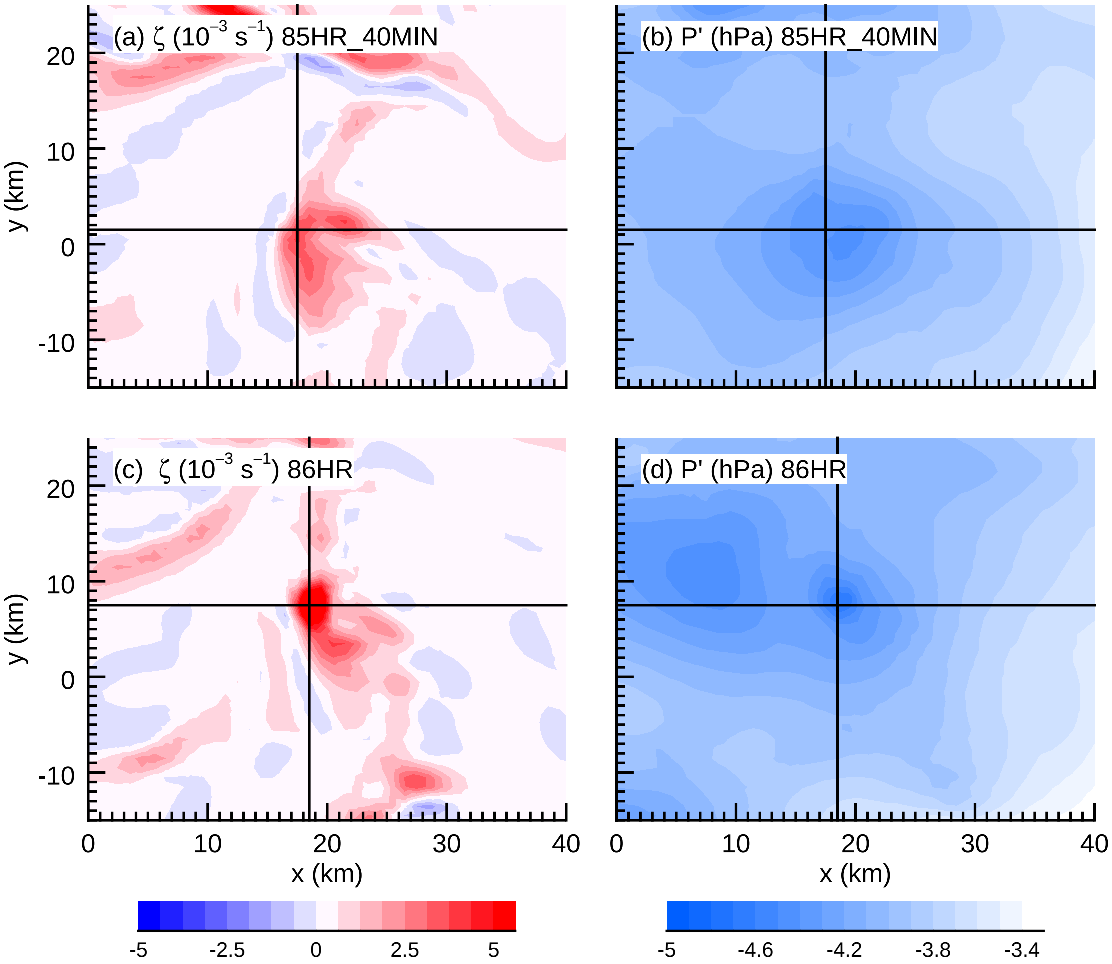

Figure 2.8: Horizontal cross sections of (left) vertical vorticity and (right) perturbation pressure taken at the lowest model level (z = 29.5 m AGL) at a model run time of (top) 85 hours and 40 minutes and (bottom) 86 hours. The crosshairs in each plot mark the center of the genesis LCVA and are included only for reference. Vorticity fields are scaled by a factor of $10^3 s^{-1}$.

on the formation of the genesis LCVA between 83 and 84 hours. We consider shear and curvature vorticity in natural coordinates defined by $-\frac{\delta V}{\delta n}$ and $V\frac{\delta \alpha}{\delta s}$, respectively, for wind speed V and angle of the s-axis with respect to the x-axis α. Partial derivatives with respect to s and n are calculated along the local wind direction and normal to it, respectively, by the definition of a natural coordinate system (e.g. Holton 1992, 61-62). Shear and curvature vorticity are not frame invariant, however the system motion provides a suitable frame for

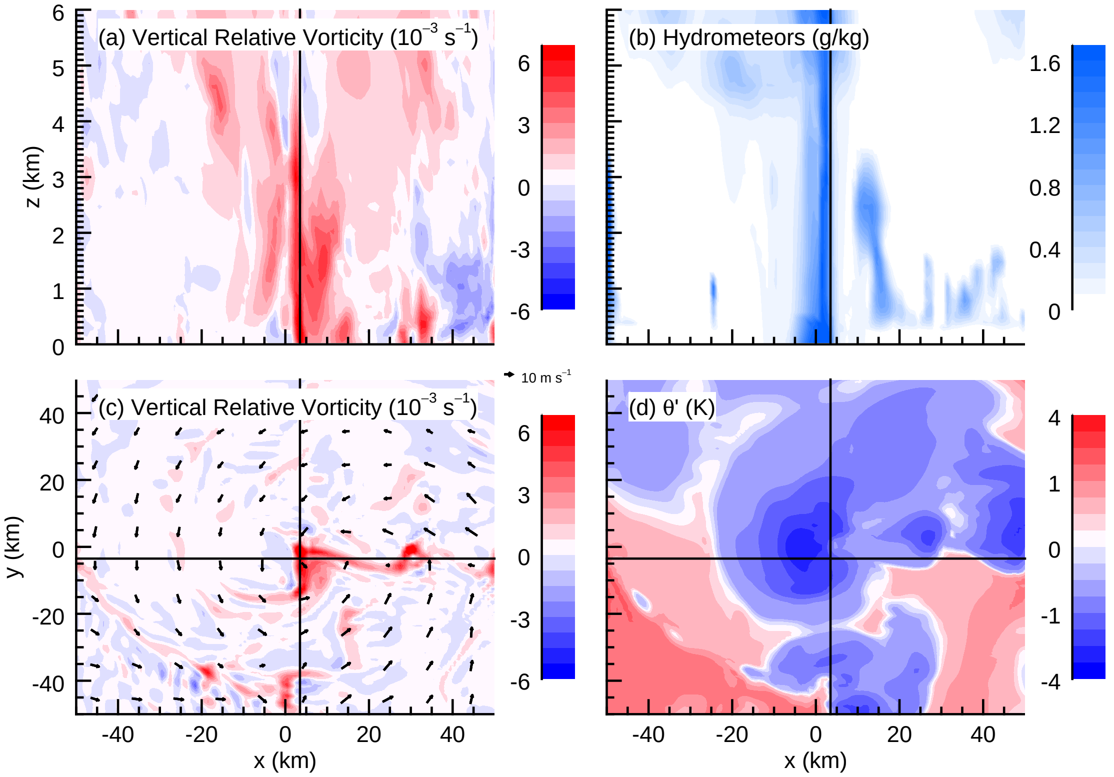

Figure 2.9: As in Figure 2.3, but at a model run time of 90 hours as TCG occurs.

our computations.

We consider the curvature vorticity budget equation employed by Schenkel (2009) originally adapted from Bell and Keyser (1993):

$$\frac{d}{dt}(V\frac{\delta\alpha}{\delta s}) = -V\frac{\partial f}{\partial s} - \frac{\delta V}{\delta s}\frac{d\alpha}{dt} - \frac{\delta}{\delta n}(\frac{\delta\phi}{\delta s}) - (f + V\frac{\delta\alpha}{\delta s})\nabla_p \cdot \vec{V} - V\frac{\delta\omega}{\delta s}\frac{\partial\alpha}{\partial p} + F_{\zeta_c} \tag{2.4}$$

The left hand side of Equation 2.4 is the Lagrangian time derivative of curvature vorticity. On the right hand side, the first term is the change in curvature vorticity from advection in a planetary vorticity gradient. This term is zero for our simulation because of the f-plane approximation. The second and third terms on the right hand side are the shear to curvature vorticity conversion terms, where ϕ is geopotential. These terms appear exactly opposite in the shear vorticity budget equation (not shown), so these terms represent curvature vorticity being produced exclusively at the expense of shear vorticity. The two terms are summed together for the following analysis. The fourth and fifth terms on the right hand side represent stretching and tilting of curvature vorticity, respectively, where ∇_p is the gradient operator in natural coordinates and ω is the vertical velocity in pressure coordinates (O'Brien, 1970). The final term on the right hand side represents our estimate for friction; the exact formulation for this is provided in Appendix C. Directional derivatives (denoted by δ) are used in the equation to account for grid points in which a natural coordinate system is not defined in order to be consistent with Schenkel (2009), although there are no such points in our simulation. Prior to performing calculations, the horizontal wind, geopotential and pressure fields are smoothed once with a 1-2-1 filter.

Figure 2.10 shows horizontal cross sections taken at a model run time of 83 hours and 22 minutes. In this figure, shear and curvature vorticity as well as terms from Equation 2.4 are smoothed once with a 1-2-1 filter after computations are performed to remove excess noise in the fields. Shown are the two adjacent cold pools responsible for the birth of the genesis LCVA (panel d, see Figure 2.5) and an enhanced region of vorticity along the interface between them (panel a). A significant portion of this vorticity is shear vorticity (compare panels b and e) brought about by the different wind directions in the two opposing convective outflows. Panel h indicates that curvature vorticity is being created at the expense of shear vorticity while panels g and i indicate that the curvature vorticity present is beginning to intensify from stretching and tilting. Panel f shows the sum of these three lowest panels and the friction term (not shown) for comparison with the time derivative of curvature vorticity (panel c). While not perfect, these two panels show many similar features, indicating that there is reasonable closure of Equation 2.4. Minor discrepancies may be due to our estimation of friction, which is computed from model output rather than being output from the model directly (see Appendix C). While shear vorticity conversion does not appear to dominate the production of curvature vorticity, its magnitude suggests that it is an important process to consider in the formation of this LCVA.

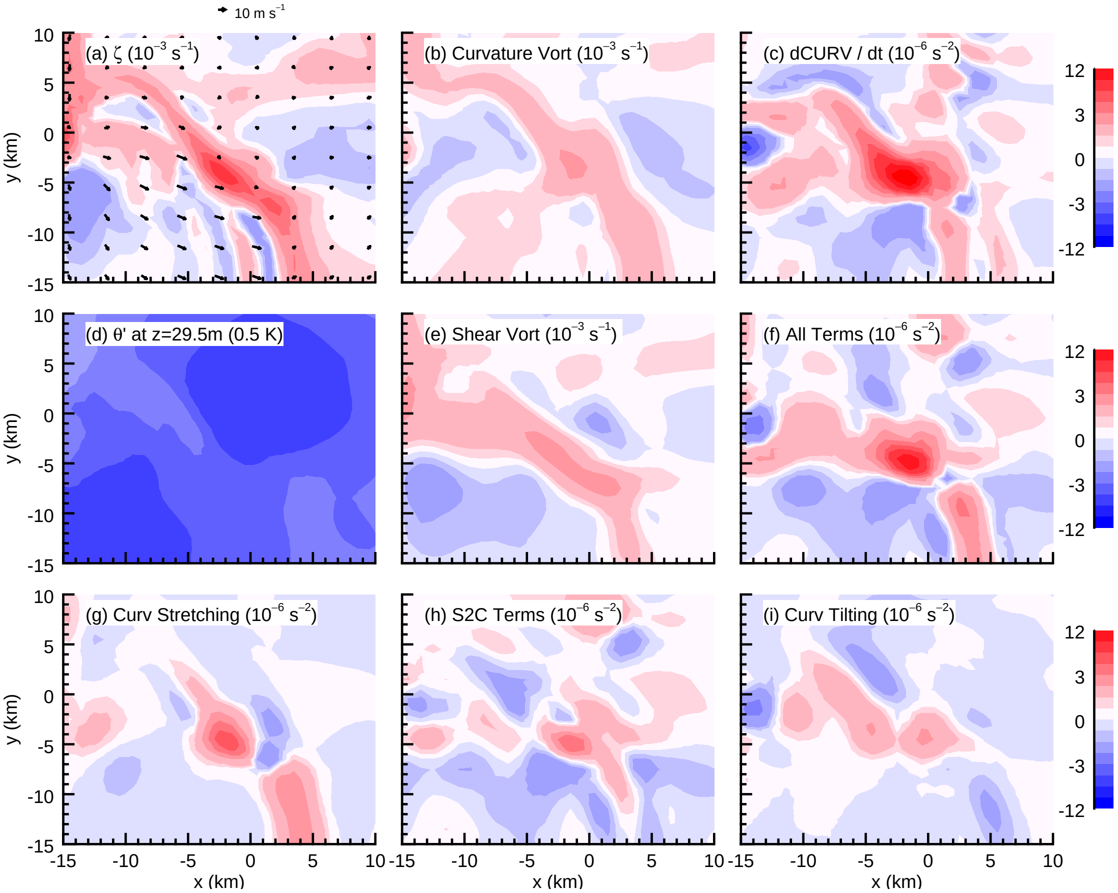

Figure 2.10: Horizontal cross sections taken at z = 91.7 m AGL at 83 hours and 22 minutes. Shown are (a) vertical vorticity with horizontal wind vectors, (b) curvature vorticity, (c) change in curvature vorticity in time, (d) perturbation potential temperature, (e) shear vorticity, and the (g) curvature vorticity stretching term, (h) both shear to curvature vorticity conversion terms and (i) curvature vorticity tilting term from Equation 2.4. Panel f shows the sum of panels g, h, i and the friction term (see Appendix C) for comparison with panel c. All panels except a and d are smoothed once with a 1-2-1 filter. Vorticity fields are scaled by a factor of 10^3 s^{-1}, Equation 2.4 terms are scaled by a factor of 10^6 s^{-2}, and the perturbation potential temperature field (which is instead taken at z=29.5 m AGL) are scaled by a factor of 2 so that it fits on the same colorbar as the other fields.

Figure 2.11 shows the same fields as Figure 2.10, except 12 minutes later at a model run time of 83 hours and 34 minutes. The genesis LCVA is now visible in panel a as a coherent vortex, which is shifted to the east because of both the background vortex and the cold pool outflow coming from the west (Figure 2.10d and the vectors in 2.10a). Although some residual shear vorticity remains (panel e), more curvature vorticity is present than before (panel b), owing primarily to conversion from shear vorticity and the stretching of curvature vorticity (as argued in the previous paragraph). A comparison of the stretching and tilting terms (panels g and i) indicates that stretching is more important than tilting in continuing to generate curvature vorticity, which is consistent with the argument presented in Section 2.3 (see Figure 2.2). The stretching term now dominates the shear to curvature term, which is expected as the LCVA shifts to primarily curvature vorticity. Panels c and f still show a reasonable agreement between the sides of Equation 2.4.

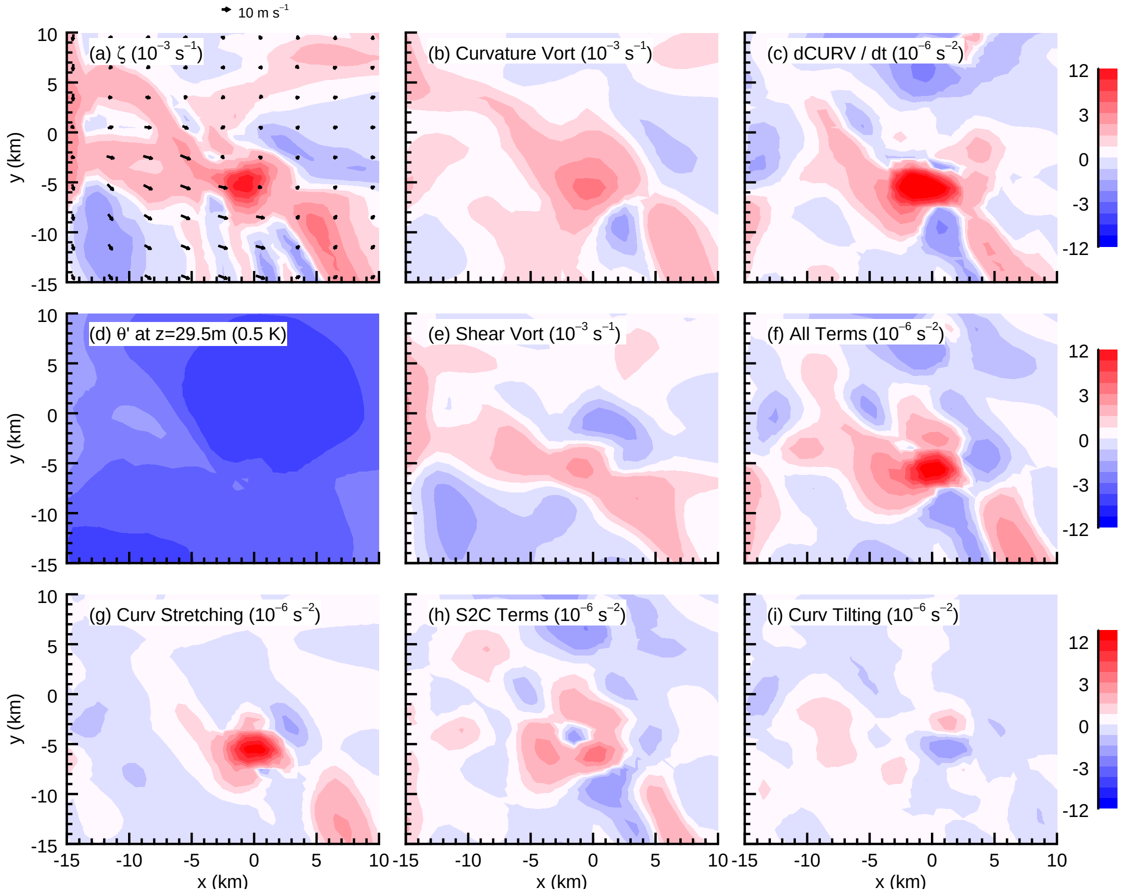

Figure 2.11: As in Figure 2.10, but at a model run time of 83 hours and 34 minutes.

The preceding analysis is evidence that LCVAs can originate from convective outflows in the presence of ambient vorticity and convection. The enhancement of shear vorticity from convergence at the outflow edge allows for the production of these very strong coherent vortices which appear to be important in some cases of TCG. In the next section we discuss the presence of vortex mergers in the simulation, which help LCVAs maintain their strength.

2.5 Vortex Merger Analysis

Many theoretical studies have found that vortices of like sign often interact with each other and may sometimes exchange vorticity without combining altogether (e.g. Dritschel and Waugh 1992; Melander et al. 1987, 1988). Vortices have also been shown to undergo mergers during numerical simulations of TCG (Hendricks et al. 2004, Montgomery et al. 2006, Wang et al. 2010, Kilroy and Smith 2013). In this section we quantitatively examine the early and genesis LCVAs for the presence of vortex mergers which may serve as a mechanism by which they can gain longevity.

Careful inspection of Figure 2.4c reveals that the early LCVA appears to be "connected" to one of the stronger LCVAs at the point $x = 24$ km, $y = 12$ km to the northeast. The vorticity to the northeast is shallow and forms at the edge of a cold pool (Figure 2.4d), just as the early LCVA did in its beginning stages (Figure 2.2). This same phenomenon can be observed in Figure 2.9c, where the genesis LCVA appears to be "connected" to another LCVA about 20 km due east of it. It is hypothesized that these represent vortex merger events in which like-signed regions of vorticity can exchange their vorticity, or combine altogether. In this section we quantitatively address this claim. Specifically, it is shown that LCVAs gather low-level vorticity horizontally from their surroundings, which may allow them a longer lifetime as the simulation progresses and there are more numerous regions of enhanced vorticity.

To test our hypothesis quantitatively, we consider the mean integral tangential momentum budget in cylindrical coordinates utilized in Hendricks et al. (2004) (their Equation 7):

$$\bar{v}(t_b)-\bar{v}(t_a)=-\int_{t_a}^{t_b}(\bar{u}\bar{\eta})dt-\int_{t_a}^{t_b}(\bar{w}\frac{\partial\bar{v}}{\partial z})dt-\int_{t_a}^{t_b}(\overline{u'\zeta'})dt-\int_{t_a}^{t_b}\overline{(w'\frac{\partial v'}{\partial z})}dt+\int_{t_a}^{t_b}(\overline{PBL}+\overline{DIFF})dt \tag{2.5}$$

where an overbar indicates an azimuthal average about a defined center point, and a prime indicates the perturbation from this azimuthal mean. Put mathematically for some parameter A,

$$A(r,\ \lambda,\ z,\ t)=\bar{A}(r,\ z,\ t)+A'(r,\ \lambda,\ z,\ t) \tag{2.6}$$

The terms on the right hand side of Equation 2.5, from left to right, are the mean horizontal vorticity flux, mean vertical momentum flux, eddy horizontal vorticity flux, eddy vertical momentum flux, and finally the influence from the planetary boundary layer (PBL) scheme and horizontal model diffusion (DIFF). Neither PBL nor DIFF are considered in the forthcoming analysis. A positive eddy horizontal vorticity flux term is consistent with a vortex merger event (i.e. $-\overline{u'\zeta'}\geq 0$, Hendricks et al. 2004). Physically this means that there are coincident regions of radial inflow and positive vorticity that are strong enough to dominate in an azimuthally averaged framework, meaning that the mean tendency is for positive vorticity to propagate towards the chosen center of the coordinate system.

For azimuthal average calculations, $\Delta\lambda$ is chosen as 6.28 x 10^{-2} radians (or 3.6°), so that there are 100 points in a full circular revolution. Time integrations are performed with the previous, current, and future values at each (r,z) point, which in total spans a time period of 2 minutes. Center points for the azimuthal averages are manually chosen as a fixed point where the smoothed maximum vorticity is found as a merger appears to be occurring. We manually altered the center point slightly and find that this does not have a large effect on these terms or the forthcoming arguments.

Figure 2.12 shows terms from Equation 2.5 at a model run time of 48 hours, during the life cycle of the early LCVA (discussed in Section 2.3.1). At this time, the early LCVA is “joined” to another region of enhanced vorticity to its southeast. The vortex to the south is shallow, with depth on the order of hundreds of meters, as it is created from the near-surface cold pool outflow of a VHT (not shown), in similar fashion to the early stages of both LCVAs. The mean radial wind computed in the LCVA-centered coordinate system is negative (indicating inflow, not shown), which is consistent with the positive values in the mean horizontal vorticity flux (panel g) computed at this time. Near the surface and extending past 15 km in radius, the eddy vorticity flux (panel d) is positive and therefore consistent with a vortex merger taking place. Panels f and i (the left and right sides of Equation 2.3) are very similar to one another indicating that this budget is accurately calculated. Minor discrepancies between these panels are likely due to the PBL and DIFF terms from Equation 2.5 not being included in panel i.

We now repeat this analysis for the genesis LCVA discussed in Section 2.3.2. Figure 2.13 shows the same fields as Figure 2.12, except at a model run time of 86 hours and 42 minutes during the life cycle of the genesis LCVA. Panel a shows the genesis LCVA which appears to be “connected” to isolated regions of vorticity to the east and southeast. The positive values from the eddy horizontal vorticity flux term found near the center of the LCVA are again consistent with a vortex merger event taking place (panel d). Panel g again indicates that radial inflow is present at low levels relative to the center of the LCVA, and comparing panels f and i indicates that the equation is still closed reasonably well. As the simulation progresses, additional convection provides more concentrated sources of positive low-level vorticity at the edges of convective cold pools, suggesting that LCVAs can be sustained by this mechanism for even longer as time goes on.

Based on the results from calculating this budget, it can be concluded that LCVAs draw some strength from other independently-formed vorticity sources in the domain, which is consistent with previous studies. As the simulation progresses, it is possible that additional convection at smaller radii due to the contracting MLV allows for LCVAs to have an easier path to the center of the larger-scale circulation by allowing for more vortex merger events

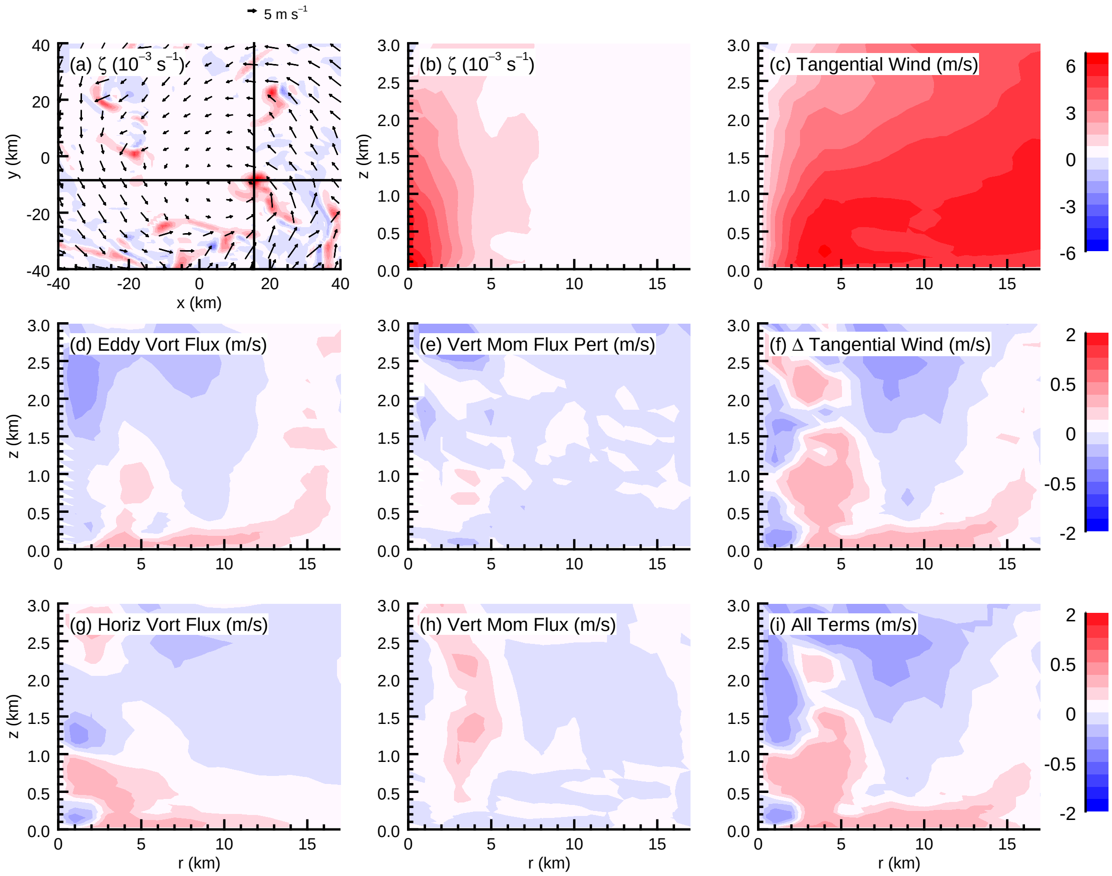

Figure 2.12: Cross sections taken at a model run time of 48 hours. Shown are (a) a horizontal cross section of vertical relative vorticity with wind vectors taken at the lowest model level (z = 29.5 m AGL) and azimuthally averaged fields of (b) vertical relative vorticity, (c) tangential wind, and the (d) horizontal vorticity flux perturbation term, (e) vertical momentum flux perturbation term, (f) change in tangential wind, (g) mean horizontal vorticity flux term, and (h) vertical momentum flux term from Equation 2.5. Panel i shows the sum of panels d, e, g, and h which comprises the right hand side of Equation 2.5 for comparison with f. The center for all averages is marked by the crosshairs in panel a. Vorticity fields are scaled by a factor of 10^3 s^{-1}.

to take place at decreasing radii.

2.6 Discussion

Our findings are consistent with those presented by Fang and Zhang (2011), who noted cyclonically propagating LCVAs in their WRF simulation of Hurricane Dolly (2008) which undergo cycles of convection and mergers (Section 2.5) causing them to persist much longer

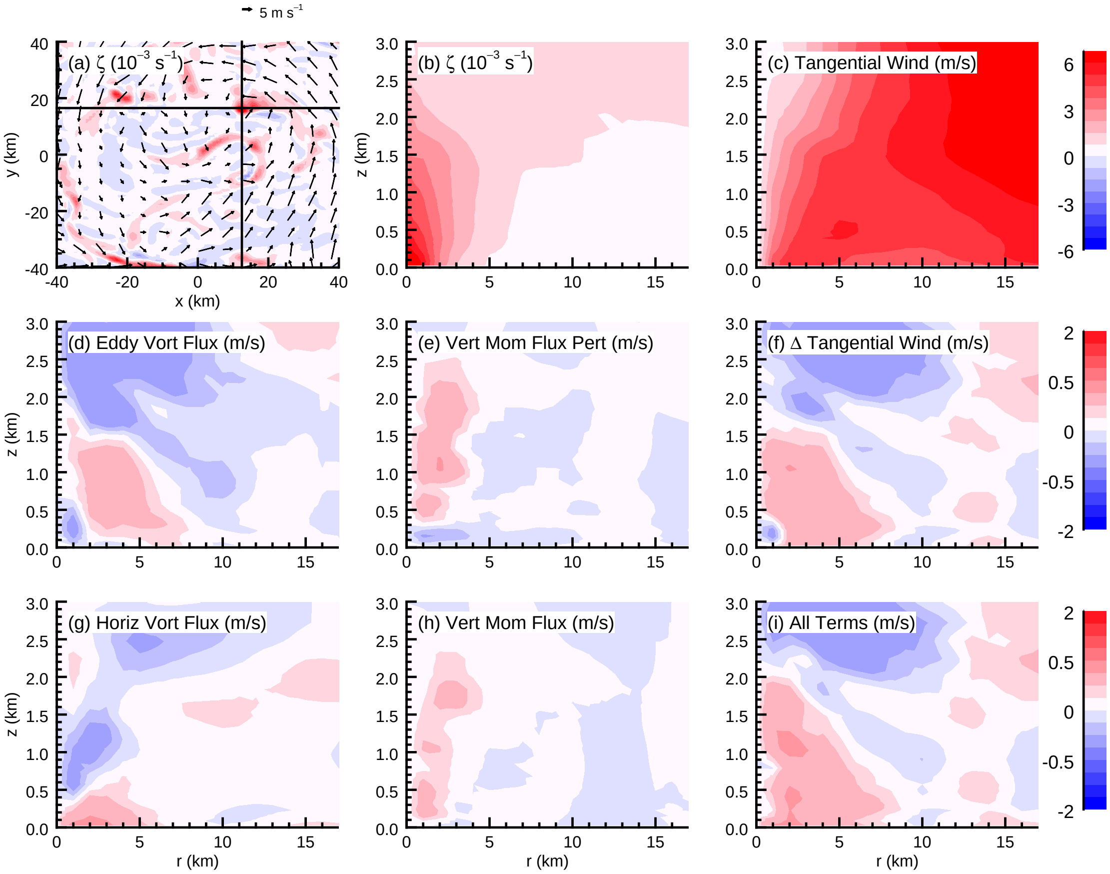

Figure 2.13: As in Figure 2.12, but at a model run time of 86 hours and 42 minutes for the genesis LCVA.

than a single convective tower (such as a VHT). Other numerical modeling approaches have also noted these phenomena, finding that vorticity is stretched into columns by deep convection in the development of TCs and that vortices tend to outlive the convection that forms them (Montgomery et al. 2010, Kilroy and Smith 2013).

It is worth noting that although TCG begins once the genesis LCVA reaches the center, the arrival of this low-level vortex in the center does not explain how the circulation increases in the mid- and upper-troposphere during TCG because vorticity is incapable of being exchanged between isobaric surfaces, according to the arguments of Haynes and McIntyre (1987). Our primary focus is not to understand how LCVAs may promote TCG in a deep layer, but rather to understand the origin of the vortex which arrives in the center (see Figures 3d and 8d from Nolan 2007). However, we do speculate that the presence of a strong, pronounced MLV in this simulation and the sudden convective burst which occurs as the genesis LCVA reaches the center are likely to assist with the concentration of vorticity in the mid- to upper-levels as TCG begins.

The processes we explore in this study could have relevance for understanding the TCG for small TCs in weak ambient vertical wind shear. While this pathway has yet to be definitively observed in nature, a study by Sippel et al. (2006) of the genesis of Tropical Storm Allison (2001) identified several meso-γ (1-10 km) and meso-β (10-100 km) scale vortices that were considered to be playing a significant role. The observed meso-γ vortices had RMW values of approximately 2 km and wind speeds on the order of 10 $m\ s^{-1}$, consistent with our observations from the early and genesis LCVAs in our RAMS simulation. The Center for Severe Weather Research (CSWR) also observed mesoscale vortices in Hurricane Harvey (2017) as it made landfall on the coast of Texas which had comparable diameters (2-11 km) to our LCVAs (Wurman and Kosiba, 2018). These observational studies suggest that LCVAs may be important beyond the scope of TCG and may lead to enhanced damage paths as hurricanes make landfall.

The pressure drop that follows the genesis LCVA during its life cycle (Figure 2.8) also reaches the domain center at 90 hours and continues to get stronger as time progresses from Figure 2.9. Since LCVAs are in approximate cyclostrophic balance (see Appendix A), a pressure drop in the center of a vortex which intensifies in synchrony with the magnitude of the wind is expected. A local pressure fall with similar intensity forming over small vortices was also discussed in Nicholls and Montgomery (2013). The authors examined the formation of such small vortices when making a decision on classifying the TCG mechanism in their simulations.

In the first of a three-part study on non-supercell tornadogenesis, Lee and Wilhelmsen modeled the creation of vortices in a similar scenario as observed here (Lee and Wilhelmson, 1997). Their experimental design included an eastward-advancing cold reservoir interacting with a southerly flow. As these regions interacted, several discrete vortices developed along the interface, which marks a shear to curvature transition without the aid of convection. This result lends further support to the ability for cold pool outflows to form an LCVA from primarily shear vorticity (Section 2.4).

2.7 Conclusions

We examine two representative low-level convectively-induced vorticity anomalies (LCVAs) in an idealized RAMS simulation of tropical cyclogenesis (TCG) in an effort to understand the origin and evolution of the small vortex (SSCV) that may form in the center of the parent circulation as TCG occurs. In our simulation it is found that LCVAs form as vorticity is concentrated by convection above regions of enhanced vorticity at the edges of cold pools. This process stretches ambient vorticity into a coherent vortex. LCVAs have maximum vorticity near the surface and outlive the convection that initially forms them. Convection occasionally strengthens these features as they cycle about the larger-scale vortex. One such LCVA that we analyze (which we termed the "early LCVA") dissipates about 8 hours after it forms, while the other LCVA we analyze (which we term the "genesis LCVA") is sustained until it reaches the center, where it becomes the low-level core of an intensifying TC. We confirm the ability for shear vorticity to convert to curvature vorticity at the edges of convective outflows, aiding in our understanding of how LCVAs are created. We also quantitatively validate that LCVAs undergo vortex merger events with other regions of enhanced vorticity in the model domain, which may provide a medium for LCVAs to retain their strength.

It is theorized that a strengthening MLV in this simulation increases the local vertical wind shear which allows for more persistent convection near the center of the ambient vortex as the simulation progresses (Figure 2.7). More persistent convection and stronger winds at the surface are also responsible for creating more outflows which may interact to produce more enhanced regions of vorticity (Figure 2.5). Additional regions of enhanced vorticity may serve to create additional LCVAs or facilitate more mergers with already active LCVAs (discussed in Section 2.5). These arguments provide evidence that the changing background conditions of the tropical disturbance eventually become conducive for an LCVA to form and make its way into the center of the larger-scale circulation. We do not feel that the success of the genesis LCVA compared to the early LCVA can be attributed to just one process. Rather, our intention is to provide evidence for some processes that might be contributors. In all likelihood, some combination of the above processes allow for this development mechanism to come to fruition, rather than there being one “smoking gun” in this group.

Throughout the simulation we present herein, many LCVAs form near the center of the larger-scale circulation which do not become the beginning of a tropical depression vortex, suggesting that there are other mesoscale thermodynamic and kinematic conditions required before it becomes conducive for an LCVA to reach the center of the larger-scale circulation and intensify. There are several environmental differences between the formation of the early and genesis LCVAs that may promote the genesis LCVA reaching the center which are not discussed in this paper. These differences include (but are not limited to) deep moistening at the center (Nolan, 2007), decreased low-level stability (Nicholls and Montgomery, 2013), the development of a broad cold pool near the center with positive vorticity around it (Nicholls and Montgomery, 2013), and a decrease in the RMW yielding higher equivalent potential temperature air closer to the center. Although we can not address the importance of these in this work, it is worthwhile for those factors to be examined in forthcoming studies to determine their role in LCVA formation and longevity.

Additional work is likewise required to verify this phenomenon in other modeling frameworks and to observationally validate the evolution and motion of LCVAs in real developing disturbances, as well as their link to TCG that we suggest here. The connection between LCVAs and tornadoes that occur in landfalling TCs also warrants exploration due to the very large values of vorticity observed near the model surface in this simulation. Since radiation is not included in this simulation, additional investigation is required to determine if the diurnal cycle of convection observed in the tropics has any impact on the persistence of convection acting on LCVAs (Gray and Jacobson Jr, 1977). A forthcoming publication will further examine the formation of enhanced vorticity and shear to curvature vorticity conversion at the edges of convective outflows in a more detailed and idealized framework.

Chapter 3

The Role of Radiation In Accelerating Tropical Cyclogenesis in Idealized Simulations

This chapter explores the role that longwave and shortwave radiation (hereafter just "radiation" unless otherwise noted) play in TCG by analyzing results from otherwise identical idealized simulations with and without radiation. This chapter is adapted from (Smith et al. 2019, full citation given below). The reader is also directed to Section 5.3 which features coauthor contributions to Nicholls et al. (2019a) for a discussion of sensitivity to radiation using the RAMS model.

Smith, W. P., Nicholls, M. E. and Pielke Sr., R. A. (2019), 'The role of radiation in accelerating tropical cyclogenesis in idealized simulations (in review)', Journal of the Atmospheric Sciences.

3.1 Introduction

Hurricanes are devastating storms capable of producing death tolls in the thousands and damage in the tens of billions of US Dollars. Prior to hurricane landfall, a vortex must transform from a tropical disturbance into a tropical depression, a process known as tropical cyclogenesis. It has been discovered through numerical modeling that longwave and shortwave radiation (hereafter just "radiation" unless otherwise noted) dramatically accelerates tropical cyclogenesis, however an important question still remains which is addressed in this paper: at what stage of development does radiation play the most significant role? We address this question by performing idealized simulations of tropical cyclogenesis with different initial vortex strengths, which represent different stages of a developing tropical disturbance.

It has long been recognized that tropical convection exhibits a diurnal cycle (e.g. Fingerhut 1978; Kraus 1963). Tropical convective activity has been noted to peak in the early morning and is weakest in the afternoon local time (Jacobson and Gray, 1976). This has been hypothesized to be due to both a nocturnal differential radiative forcing between cloud structures and their relatively clear-sky surroundings (Gray and Jacobson Jr, 1977) and to nocturnal longwave-induced destabilization (Xu and Randall, 1995). Convective destabilization of clouds due to longwave radiation is sensitive to the cloud quantity (Godbole, 1973) and has been linked to the intensification of tropical mesoscale convective systems (Dudhia, 1989; Miller and Frank, 1993).

It has been shown that numerical simulations of tropical cyclones (TCs) demonstrate high sensitivity to the changes in radiation due to the presence of hydrometeors, also known as cloud radiative forcing (CRF). The presence of CRF tends to form a broader storm circulation and enhances upper-tropospheric radial outflow, ascent in the core of the vortex, and outer-core winds (Bu et al., 2014). TC tracks, intensities, distribution of winds and strength of the secondary circulation are also greatly affected by CRF (Fovell et al., 2016).

Due to the documented diurnal variability of tropical convection and the impacts of CRF on TCs, it follows that TCs also exhibit a diurnal variability in convective activity (e.g. Leppert and Cecil 2016). This signature exists in observations of TCs (e.g. Dunion et al. 2014; Knaff et al. 2019) and has been reproduced in numerical models (e.g. Navarro and Hakim 2016). In addition to convective activity, TCs also exhibit diurnal cycles in their wind fields and their thermodynamic structure (Dunion et al., 2019). It has been noted that wind speeds tend to peak about 6 hours after the peak in heating occurs (Navarro et al., 2017).

The impacts of radiation on stability in the tropics is an important consideration for TCs as well. While longwave emission tends to destabilize the atmosphere, shortwave radiation tends to stabilize the atmosphere by diminishing cloud top cooling (Schmetz and Beniston, 1986). This may in turn restrict secondary eyewall formation in mature TCs (Tang et al., 2017). It has been shown that cooling at the tropopause and above can lead to significant changes in the potential intensity of TCs (e.g. Ramsay 2013; Wang et al. 2014). Temperatures in the upper troposphere have recently been linked to changes in ice species, upper-level vertical mass flux and the height of the TC (Trabing et al., 2019). Radiation's impacts on the Brunt-Väisälä frequency have been linked to potential vorticity near the tropopause, which may have implications for the rapid intensification of TCs (Duran and Molinari, 2019).

A vital process in the formation of a TC is the transformation from a tropical disturbance to a tropical depression, otherwise known as tropical cyclogenesis (hereafter "TCG"). Some of the earliest work found that TCG is favored in regions with sea surface temperatures (SSTs) in excess of 26°C and vertical wind shear less than 10 knots (Gray, 1968). More recently, the roles of convective organization and inner-core moisture in TCG have been explored in the literature. Early in the evolution of a tropical disturbance, the core tends to gradually warm and moisten and angular momentum surfaces are drawn inwards (Kilroy et al., 2016). The character of convection may change once the relative humidity (RH) reaches about 80% in the disturbance core below a height of 7 km, increasing the likelihood of TCG (Davis, 2015). Although mid-level vortices (MLVs) are frequent precursors to TCG, it is theorized that they are not essential for the development of a tropical depression (Kilroy et al., 2018).

Recent numerical modeling studies have shown the paramount importance of radiation in TCG. Removing radiation in a simulation often inhibits TCG from occurring for several days, suggesting that radiation plays a very active role in the development of a tropical disturbance (Melhauser and Zhang, 2014; Nicholls, 2015; Nicholls et al., 2019a; Nicholls and Montgomery, 2013; Tang and Zhang, 2016). Feedbacks of longwave radiation are found to assist with the self-aggregation of convection (Muller and Romps, 2018) and the development of a circulation (Wing et al., 2016). Although there appear to be distinctly different “pathways” to TCG depending on a model’s initialization and chosen physics parameterizations (Hendricks et al., 2004; Montgomery et al., 2006; Nolan, 2007), turning off radiation dramatically slows development regardless of the specific mechanism at play (Nicholls and Montgomery, 2013).

During TCG, sensitivity to radiation appears to be due to a weak nocturnal transverse circulation brought about from differential radiative forcing between the cloudy disturbance and the surrounding cloud-free region at night, similar to the mechanism discussed in Gray and Jacobson Jr (1977) for organized convective clouds. This circulation is associated with a slow rising motion in the core and subsidence in the surroundings, which leads to increased RH in the core of the disturbance and thereby promoting convection (Nicholls, 2015). Tao et al. (1996) also noted that radiation tends to increase the RH of the core, which enables additional condensation in a convective column. A moist vortex is more likely to undergo TCG (e.g. Bister and Emanuel 1997; Pielke Jr and Pielke Sr 1997; Rappin et al. 2010), lending further support to the fact that radiation accelerates development. TCG is also sensitive to heating and cooling from the diurnal cycle of radiation which impacts deep, moist convection (Melhauser and Zhang, 2014). The detrimental effects of shortwave radiation on tropical convection also translate to TCG, where sensitivity studies to shortwave radiation indicate that TCG is often delayed with it included (Tang and Zhang, 2016).

Despite the documented sensitivity of tropical disturbances to radiation as found in numerical modeling studies, there has been little exploration into the exact “stage” where radiation is the most important during TCG, a gap that this study seeks to address. Nicholls and Montgomery (2013) ran an extensive suite of simulations varying many initial parameters in their model, one of which was vortex strength. However, none of their simulations without radiation were run for the stronger version of their vortex. Nicholls (2015) briefly explored the impacts of imposing radiative forcing on two vortices which had already undergone TCG and concluded that radiation did not have as large an impact on intensification as it does on genesis, however these experiments did not employ a full physics suite, nor were their initial vortices weak enough to make inferences for TCG. Craig (1996) noted in simulations that radiation did not play a significant role in the intensification of TCs, however their initial vortex was a bit too strong to infer any applications for TCG.

The current work performs full-physics idealized simulations of three different initial vortices and explores how the sensitivity to radiation varies among them. In doing so, we highlight the stage of TCG where radiation is most important, giving further insight into our understanding of the role that radiation plays. We hypothesize that the stronger an initial vortex, the less impact that radiation has on the timing of TCG.

3.2 Methods

3.2.1 Numerical Model and Experimental Design

The Advanced Research WRF model (WRF-ARW) Version 3.9 is employed for the simulations presented in this study (Skamarock and Coauthors, 2008). Our simulations are based on the TC "test" simulation that comes with the default WRF-ARW distribution, which we modify significantly for the objectives in this study. We change the initial vertical structure of horizontal winds so that they are maximized at mid-levels rather than the surface, since a mid-level mesoscale convective vortex has been observed by numerous studies to be a precursor to TCG (e.g. Bister and Emanuel 1997; Harr and Elsberry 1996; Reasor et al. 2005; Zehr 1992). This change also allows our initial vortex to conform more closely to the one employed in Nicholls and Montgomery (2013) and Nicholls (2015) who used the Regional Atmospheric Modeling System (RAMS, Pielke et al. 1992). The exact methodology and formula for our vortex is given in Appendix D.

The simulations all contain three co-centric grids with horizontal grid spacing of 15 km (301 x 301 points), 3 km (301 x 301 points) and 1 km (400 x 400 points). All three grids have 60 vertical levels which are vertically stretched with height from about 100 m spacing near the surface to about 1 km spacing near the tropopause. The lowest model level is at 40.6 m above ground level (AGL) and the model top is at 25.0 km AGL. WRF uses a terrain-following η-vertical coordinate; for each model level we calculate physical height by averaging the base-state geopotential field in x, y, and time and then dividing by g = 9.81 $m\ s^{-2}$. The SST is set to a constant 28°C and the Coriolis force is approximated with an f-plane at a latitude of 15°N. The domains are located at 0° longitude and initialized at midnight local time.

These simulations utilize the mean tropical sounding from Jordan (1958) as a horizontally uniform initial state. Physics schemes used in these simulations include the Thompson microphysics scheme (Thompson et al., 2008), the RRTMG longwave and shortwave radiation schemes (Iacono et al., 2008) which update every 5 minutes, and the YSU planetary boundary layer (PBL) scheme (Hong et al., 2006). Because of the idealized nature of these simulations, the authors do not feel there is a need to parameterize convection in each disturbance's surrounding environment, so no cumulus scheme is activated for the coarse grid. An implicit gravity wave damping layer (*damp_opt* = 3) is used to suppress vertically propagating gravity waves from interacting with the model top, which covers the highest 5 km of the domain. All nests have two-way feedback enabled and the coarsest grid uses periodic boundary conditions on its zonal and meridional edges. Alternative drag and surface enthalpy coefficient formulations designed for TC applications are employed in all simulations ($isftcflx = 1$).

In order to understand when radiation is most important, we run simulations with and without radiation (hereafter "RAD" and "NORAD," respectively) for three different initial vortices. The mathematical formulation for these vortices is given in Appendix D. Table 3.1 provides a summary of these simulations and indicates their initial wind values at the surface and the height of maximum winds (4 km AGL). The two "Weak" and two "Medium" simulations are run for 5 days, while RAD_Strong is run for 3 days and NORAD_Strong is

Table 3.1: An overview of the 6 "core" simulations performed in this study. The two rightmost columns show the maximum azimuthally averaged tangential wind values from the initial vortex at the lowest model level (40.6 m AGL) and at the height of maximum winds (about 4 km AGL), respectively.

Name	Radiation	Microphysics	Max Surface V	Max V at 4 km
RAD_Weak	RRTMG	Thompson	4.7 $m\ s^{-1}$	9.1 $m\ s^{-1}$
NORAD_Weak	None	Thompson	4.7 $m\ s^{-1}$	9.1 $m\ s^{-1}$
RAD_Medium	RRTMG	Thompson	6.3 $m\ s^{-1}$	12.2 $m\ s^{-1}$
NORAD_Medium	None	Thompson	6.3 $m\ s^{-1}$	12.2 $m\ s^{-1}$
RAD_Strong	RRTMG	Thompson	7.9 $m\ s^{-1}$	15.3 $m\ s^{-1}$
NORAD_Strong	None	Thompson	7.9 $m\ s^{-1}$	15.3 $m\ s^{-1}$

run for 4 days. These 6 simulations (hereafter the "core simulations") form the foundation of this paper, however we run several other simulations (discussed in Section 3.3.3) which test a supplementary hypothesis that after the vortex core is moistened in a deep layer by radiation, radiation thereafter becomes less influential in accelerating TCG.

All of the following analyses are performed on the 3 km spaced grid because it spans into the tropical depression's surrounding environment, unlike the 1 km grid which only covers the core of the vortex. Because of our modifications to the initial vortex and the vertical height array chosen, the surface pressure balances at about 1017 hPa. Although this is higher than would be expected in the real world, the authors do not believe that the robustness of the following results are impacted by this in any way.

The nature of convection in TCs is random and intrinsically unpredictable (e.g. Van Sang et al. 2008). In order to validate that the differences between the simulations in this study are due to changes in radiation and moisture rather than the stochastic distribution of convection, we add modest perturbations to the SST field and perform otherwise identical runs of all the simulations presented herein twice. The mathematical formulation for these perturbations and the results from this ensemble are discussed at length in Appendix F. However, all of the figures and analyses that follow are produced from the simulations with a constant

SST.

3.2.2 Computations

We adopt a relatively simple tracking strategy for objectively determining a center point for azimuthal average calculations, since a vortex tends to move about in the domain after TCG occurs. First, we smooth the surface pressure field 50 times with a 1-2-1 filter in both the zonal and meridional directions, similar to the approach of Nolan et al. (2009). If the minimum smoothed pressure is below a specified threshold (for which we choose 1013 hPa), then the location of the minimum is used as the center point. If it is not below this threshold, then the center point is chosen as the location of the maximum initial vertical relative vorticity at the lowest model level (in other words, the original center of the vortex).

There is no widespread quantitative metric for defining if TCG has occurred (e.g. Nolan and McGauley 2012), so we determine this time as the point when the maximum azimuthally averaged tangential wind at the lowest model level (40.6 m AGL) reaches 12.0 $m\ s^{-1}$. We note by inspection that once our vortices reach this threshold, the wind (pressure) field is on a rapid rise (decline), supporting our contention that TCG has occurred. We also consider the time it takes each vortex to transition from a tropical depression to a tropical storm (upon reaching 17.5 $m\ s^{-1}$ winds) and from a tropical storm to a hurricane (upon reaching 33.0 $m\ s^{-1}$ winds). Data are output from WRF at 3-hour intervals, so we linearly interpolate to find a more precise approximation for when each classification is attained, and then round to the nearest hour.

3.3 Results

3.3.1 Sensitivity to Initial Vortex Strength

Table 3.2 shows the genesis times of all simulations performed in this study. The six core simulations given in Table 3.1 are given in the first group, along with a simulation which is performed using the weak initial vortex that includes radiation but has CRF deactivated (discussed more below). Following those seven simulations are five others which test sensitivity to initial moisture and to shutting off radiation during a run, which are introduced and described in Section 3.3.3. To further highlight their progression, time series of the six core simulations' intensity are shown in Figure 3.1. The weakest initial vortex is able to undergo TCG with radiation, but fails to do so in the absence of radiation in a 5 day period. The medium-strength and strong initial vortices are able to undergo TCG both with and without radiation within the allotted simulation time, however the absence of radiation delays genesis by about 2 days in both cases. We note, as expected, that strengthening a vortex without modifying radiation allows for TCG to happen faster.

Table 3.2: A list of times it takes for each simulation to reach TCG (12.0 $m\ s^{-1}$), tropical storm status (17.5 $m\ s^{-1}$) and hurricane status (33.0 $m\ s^{-1}$), respectively. Wind values are determined as the maximum azimuthally averaged tangential wind about the center point discussed in Section 3.2.2 at the lowest model level (40.6 m AGL). All times are linearly interpolated from 3 hour model output spacing and rounded to the nearest hour.

Name	TCG Time (h)	TD → TS Time (h)	TS → H Time (h)
RAD_Weak	70	4	14
NORAD_Weak	>120	n/a	n/a
NOCRF_Weak	88	4	11
RAD_Medium	42	5	13
NORAD_Medium	91	5	15
RAD_Strong	32	3	15
NORAD_Strong	74	4	13
RAD_Strong_MOIST	25	5	17
NORAD_Strong_MOIST	29	6	15
RAD_Strong_MOIST_LL	48	4	15
NORAD_Strong_MOIST_LL	66	3	15
RAD_Weak_Remove	72	6	13

It is interesting to note that the time it takes to go from a tropical depression to a tropical storm and from a tropical storm to a hurricane is not appreciably affected by the presence of radiation. This suggests that once winds at the surface are sufficiently fast,

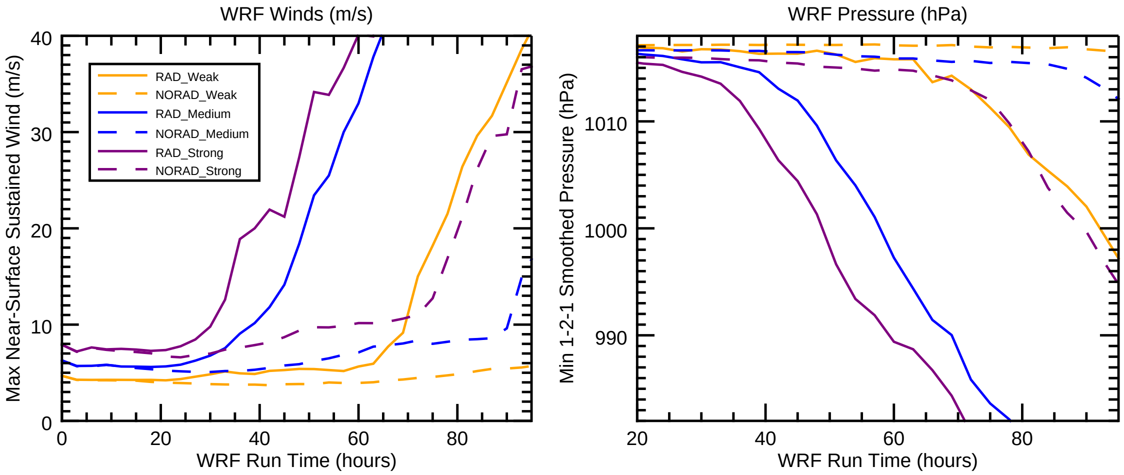

Figure 3.1: Time series of the (left) maximum azimuthally averaged tangential wind at the lowest model level (40.6 m AGL) and (right) the minimum smoothed surface pressure from the six core simulations.

fluxes from the warm ocean below provide a catalyst for increasing the intensity of the TC, rather than relying on any radiative mechanism. Using RAMS, Nicholls (2015) found that radiation did accelerate the transition from a tropical depression to a tropical storm, however this inconsistency might be explained by the different numerical model and employed physics schemes compared to those in this work.

Figure 3.2 shows azimuthally averaged tangential wind and ice hydrometeor fields for the six core simulations after 42 hours of run time. The RAD_Strong simulation has already undergone TCG and intensified into a tropical storm, and the RAD_Medium simulation is about to do the same. Distinguishable MLVs can be identified in the RAD_Weak and NORAD_Strong simulations prior to TCG. MLVs are a frequent precursor to TCG and have been seen in both models and observations (e.g. Davis and Ahijevych 2012; Kutty and Gohil 2017; Nolan 2007; Reasor et al. 2005; Ritchie and Holland 1997). All six of these simulations develop a strong MLV prior to TCG, which may be caused by sublimation at the base of their stratiform hydrometeor canopies after sufficient convection develops (Nicholls et al., 2018).

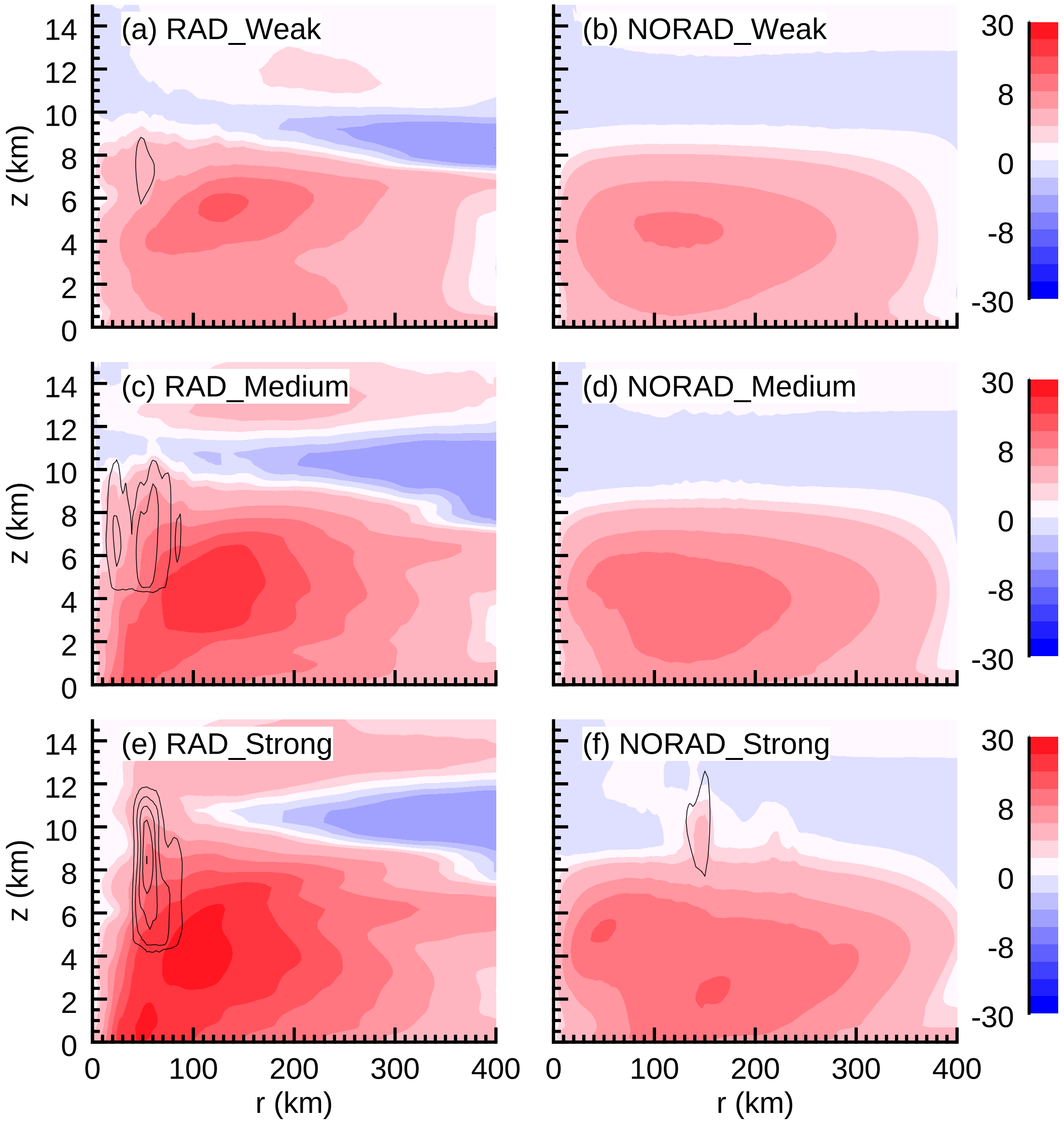

Figure 3.2: Azimuthally averaged tangential winds ($m\ s^{-1}$, filled contours) and total ice hydrometeor mixing ratio (black lines, incremented at 0.25 $g\ kg^{-1}$) from the six core simulations taken at a model run time of 42 hours. Simulations with (without) radiation are shown in the left (right) column and initial vortex strength increases from top to bottom. Center points for azimuthal averages are determined from the objective methodology given in Section 3.2.2.

Figure 3.3 shows the same fields as in Figure 3.2, but 27 hours later at a model run time of 69 hours. By this time the RAD_Strong and RAD_Medium simulations have reached hurricane status, and the RAD_Weak and NORAD_Strong simulations have developed strong MLVs with TCG imminent. Although the NORAD_Medium simulation has made some marginal progress, the NORAD_Weak simulation shows virtually no sign of development. Simulations with radiation develop ice canopies much faster, which is a proxy for convective activity being favored when radiation is included. These results suggest that radiation is very influential at the very early stages of TCG, but as a vortex gets stronger radiation is decreasingly important. In the next section we examine more specific details about how radiation influences these developing vortices.

3.3.2 Sensitivity to Radiation

In the previous section we show that a vortex is still able to undergo TCG without the influence of radiation for a sufficiently strong initial vortex, however in all cases genesis is delayed significantly compared to simulations with radiation included. In this section we explore the impact that radiation has on accelerating TCG, in particular its influence on convective activity. Figure 3.4 shows azimuthally averaged cross sections of total ice hydrometeors and coupled radiative forcing from the six core simulations at a model run time of 30 hours, as the first full night is ending in the simulation. As expected, a stronger initial vortex produces larger mixing ratios aloft from increased surface fluxes (compare Figures 3.4a-c and 3.4d-f). However, even for the strongest initial vortex, surface fluxes alone are not sufficient to rapidly produce an ice canopy without radiation included (compare Figures 3.4c and 3.4f).

Once a stratiform ice canopy develops, a weak transverse circulation forms which is driven by the radial gradient of nighttime longwave cooling. This circulation is marked by upward motion in the core and subsidence in the surroundings, which slowly moistens the core and favors convection (Nicholls, 2015). Figures 3.4g-i show this radial gradient of cooling is present in our simulations, with the core experiencing less cooling than the surrounding environment beneath a height of 8 km AGL due to hydrometeors “trapping” more outgoing

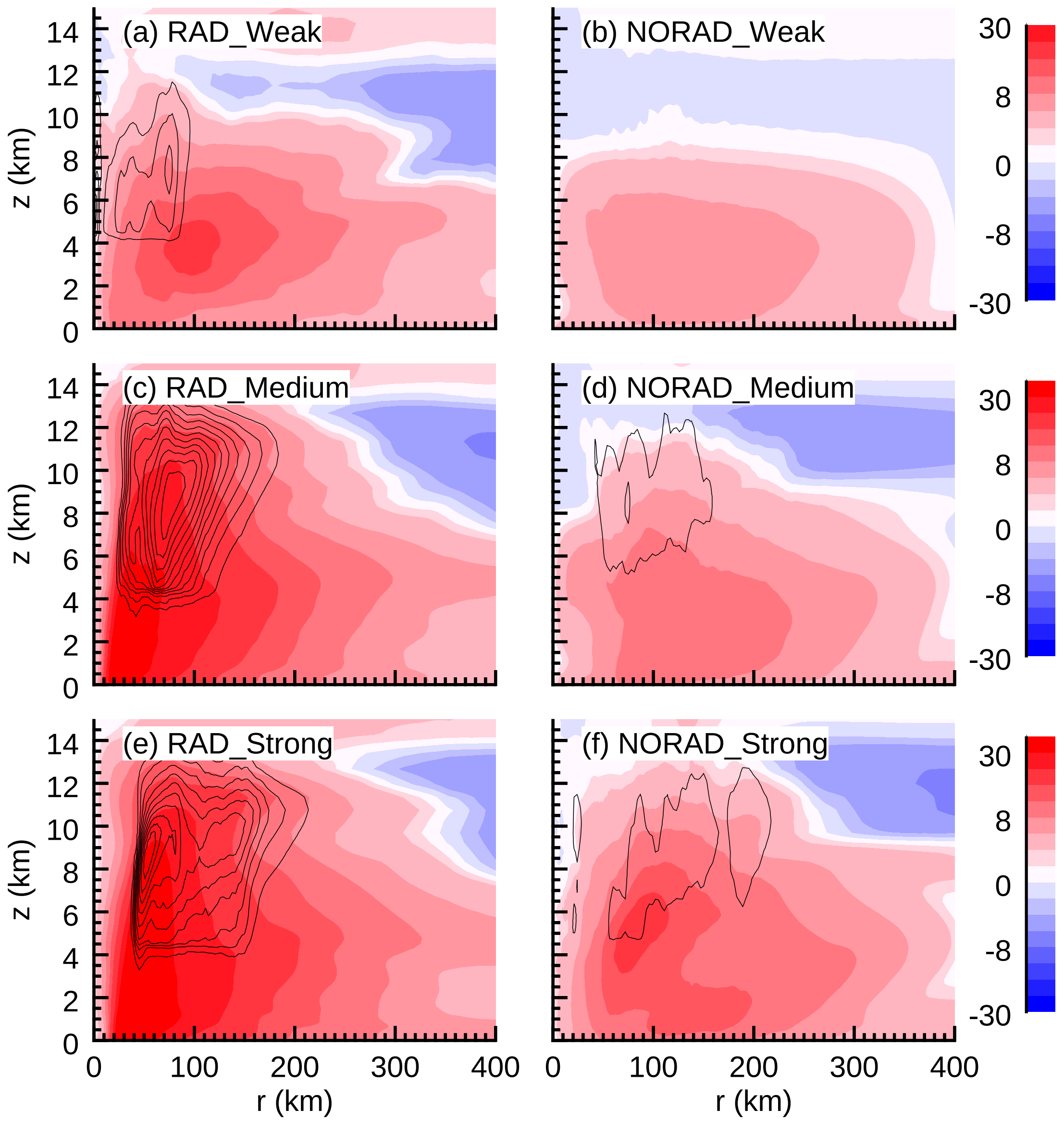

Figure 3.3: As in Figure 3.2, but at a model run time of 69 hours.

infrared radiation from the surface than clear sky does. As expected, this mechanism is stronger with a more developed hydrometeor canopy (compare Figures 3.4e-f, 3.4h-i). The expected general structure of tropical radiative forcing is seen in these simulations, with strong nocturnal infrared cooling present at the cloud top and warming at the cloud base (Webster and Stephens, 1980).

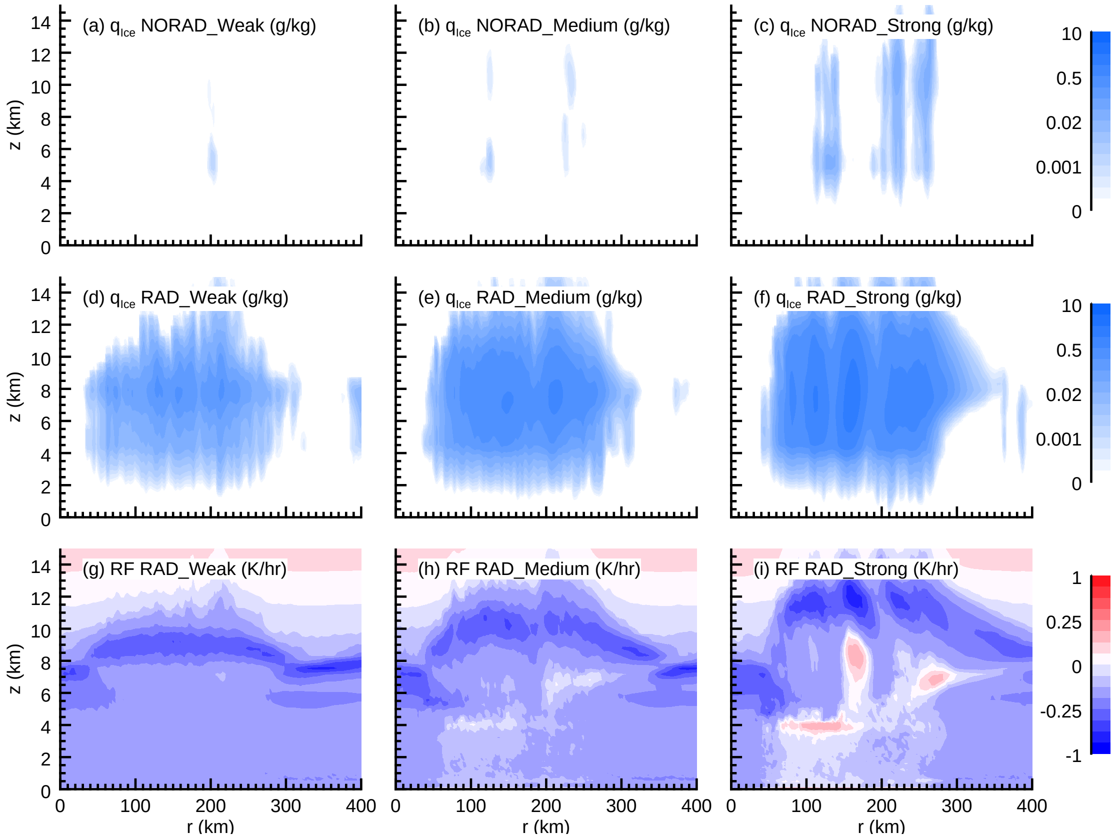

Figure 3.4: Azimuthally averaged cross sections of (top and middle) ice hydrometeor mixing ratio ($g\ kg^{-1}$) and (bottom) coupled radiative forcing ($K\ hr^{-1}$) from the six core simulations at a model run time of 30 hours.

To further support that radiative heating by hydrometeors is influential in genesis, we perform a simulation with the weak initial vortex with radiation activated but CRF disabled (NOCRF_Weak). This means that longwave and shortwave radiation do not respond to (interact with) hydrometeors. As given in Table 3.2, this simulation takes 88 hours to undergo genesis, which is significantly different than the 70 hours it takes with CRF activated. This suggests that radiation's interaction with hydrometeors is important in TCG. It is worth clarifying that longwave radiation in the simulation with no CRF still responds to the enhanced vapor mixing ratio in the core, which may still lead to a subdued version of the transverse circulation mechanism. Without the influence of enhanced RH, it stands to reason that the difference in genesis time between the RAD_Weak and NOCRF_Weak simulations would be even greater than we observe.

The diurnal cycle of radiation influences tropical convection primarily through nighttime longwave cooling which acts to moisten the core overnight. This mechanism is hypothesized to be responsible for an early morning maximum in convective activity (Gray and Jacobson Jr, 1977). Figure 3.5 shows time series of total ice mass in the 3 km domain and outgoing longwave radiation from the RAD_Medium simulation. A clear diurnal cycle of ice mass is present with an early morning maximum (Figure 3.5a), as evidenced by the peaks of the time series occurring at 9am local time as the sun is rising in the domain (dashed vertical lines), indicating that our studies are consistent with the observed tropical diurnal cycle mechanism. Figure 3.5b provides another means to show the radial gradient of nighttime longwave cooling, indicating that the cloudy core of the disturbance (less than 300 km from the center) prevents more longwave radiation from reaching the model top than the surrounding environment does, which drives the weak nocturnal transverse circulation (Nicholls, 2015).

Figure 3.6 shows the change in RH in the RAD_Medium and NORAD_Medium simulations from 0 to 36 hour run time. Both simulations have undergone low-level moistening, however there is a very large difference between the two simulations above 6 km AGL: the simulation with radiation has undergone a significant moistening at upper levels. The RAD_Medium vortex is now primed for TCG, which happens just 6 hours later, while it takes the simulation without radiation more than 2 more days to follow suit. This result is consistent with Rappin et al. (2010) who noted that TCG occurs when the storm's core becomes nearly saturated. We hypothesize that radiation's impact on enhancing convection leads to rapid deep moistening in a simulation, which is then favorable for TCG regardless of the continued influence of radiation. The next section introduces several supplementary simulations which support this claim.

(a) Total Ice Mass

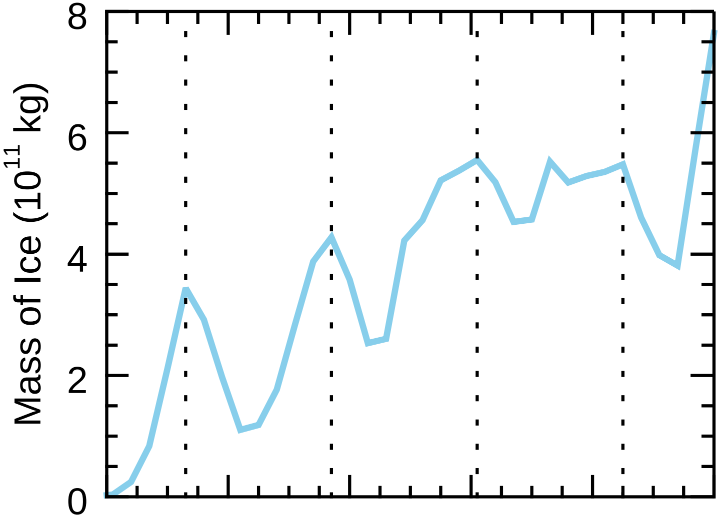

(b) Outgoing Longwave Radiation

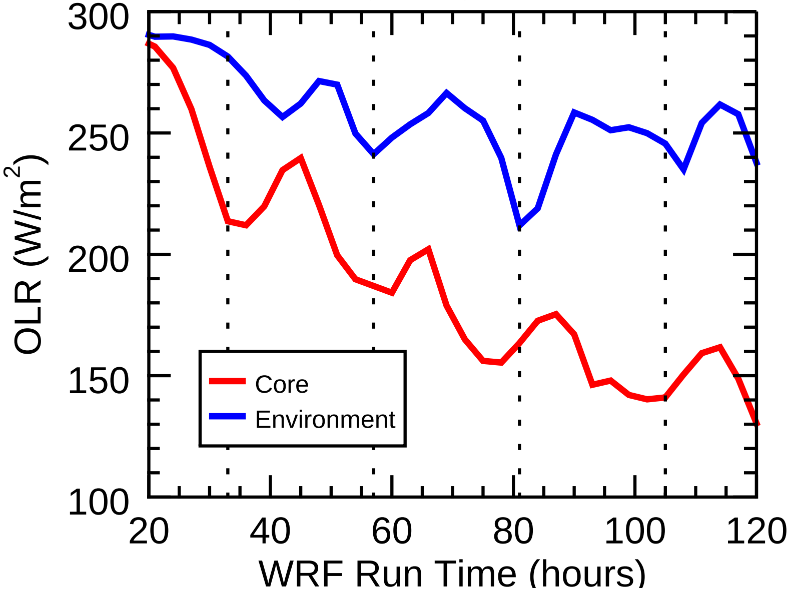

Figure 3.5: Time series of (top) total ice mass in the entire 3 km domain and (bottom) outgoing longwave radiation at the model top averaged inside (red) and outside (blue) of a 300 km radius, both from the RAD_Medium simulation. Vertical dashed lines indicate 9am local time.

3.3.3 Sensitivity to Moisture

We show in the previous two subsections that all else equal, radiation has less influence on the timing of TCG for a stronger initial vortex. However, as seen in Figure 3.1 and Table

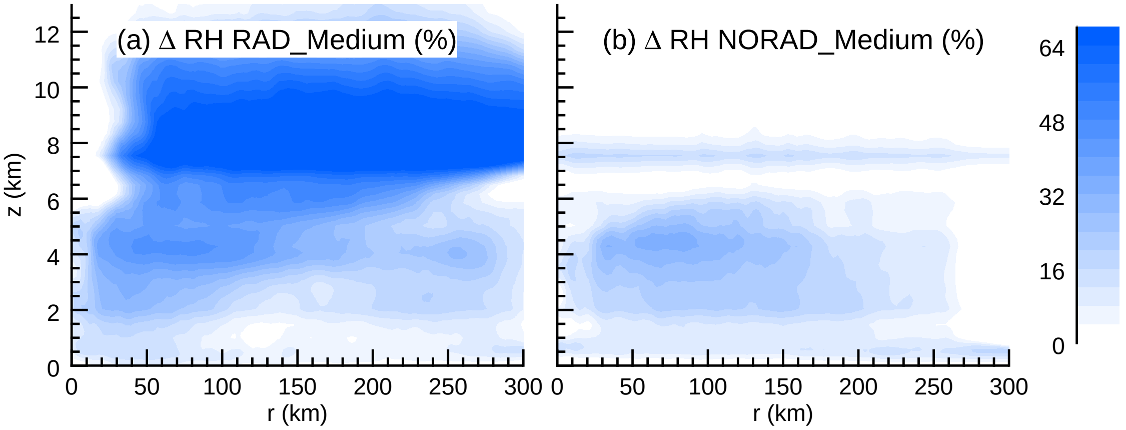

Figure 3.6: Azimuthally averaged cross sections of the change in RH from 0 to 36 hour run time from the (left) RAD_Medium and (right) NORAD_Medium simulations.

3.2, there is still a large disparity between runs with and without radiation. Figure 3.6 highlights a key difference between simulations with and without radiation: deep moistening of the vortex core occurs more readily with radiation included, which we hypothesize allows a vortex to undergo TCG even without the presence of radiation thereafter. Here we undertake five additional simulations which validate this claim.

Four additional simulations, which we name RAD_Strong_MOIST, NORAD_Strong_MOIST, RAD_Strong_MOIST_LL, and NORAD_Strong_MOIST_LL (where "LL" signifies "low-level"), are run which have identical initial vortices and physics parameterizations to the RAD_Strong and NORAD_Strong simulations except that the initial sounding from Jordan (1958) is moistened. In the "MOIST" ("MOIST_LL") runs, the sounding is moistened in a deep (shallow) layer. The exact modifications to the sounding are given in Appendix E. The purpose of the "MOIST" simulations is to mimic the core moistening which occurs faster in simulations with radiation due to enhanced convective activity to see if radiation still accelerates development once a vortex reaches that point. The "MOIST_LL" simulations are run to emphasize that moistening must be in a deep layer before radiation becomes less important in TCG.

Figure 3.7 shows the same time series as Figure 3.1, but for only the "Strong" initial vortices with and without the deep moisture anomaly. The purple curves are identical to those in Figure 3.1. It can easily be noted that for the deep-moistened initial sounding (brown curves), the presence of radiation only makes a small difference in the progression of these simulations. Table 3.2 also confirms that TCG occurs at nearly the same time with and without radiation, compared to a 42 hour difference for the default sounding. The similarity between these simulations suggests that once a vortex is sufficiently strong and moist, radiation does not play a role in its development or early intensification. It is also worth noting that regardless of the initial moisture field, TCG seems to occur once the core moisture reaches a certain threshold. This is illustrated in Figure 3.8, where fields of RH are qualitatively similar at the respective genesis times in two simulations. This supports the claim that the moisture modification made to these simulations is not excessive and is in line with that of the six core simulations when they reach TCG.

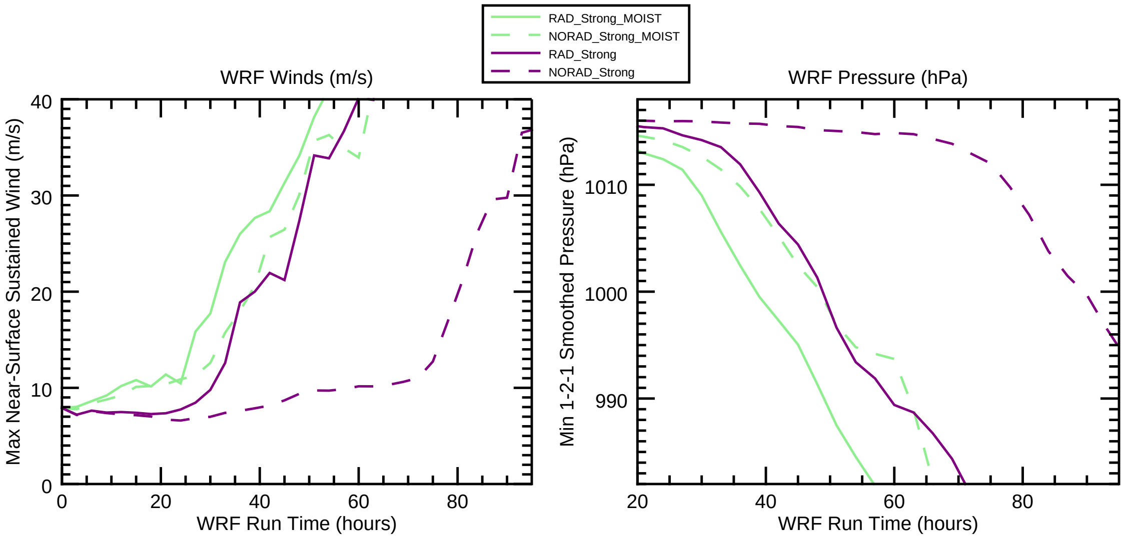

Figure 3.7: As in Figure 3.1, but for the 4 "Strong" initial vortex simulations. Time series in green (brown) show simulations with the default (deep-moistened) initial sounding described in Appendix E. The green curves are exactly the same as those pictured in Figure 3.1.

In order to emphasize that moisture must be enhanced in a deep layer before TCG ceases to depend on radiation, we run two simulations with extra moisture applied to the initial sounding only in the lowest 2 km AGL (denoted by "MOIST_LL"). Table 3.2 shows

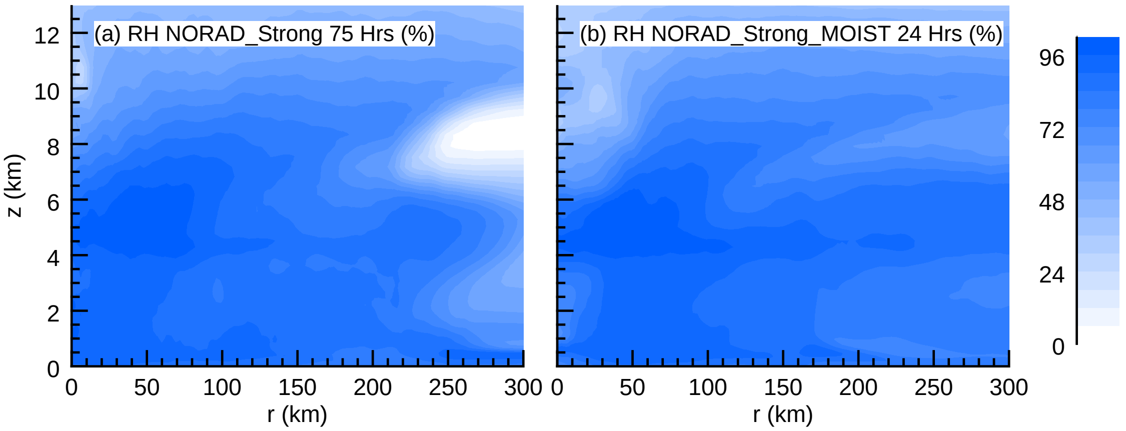

Figure 3.8: Azimuthally averaged cross sections of RH from the (left) NORAD_Strong simulation at 75 hours and the (right) NORAD_Strong_MOIST simulation at 24 hours.

that TCG is delayed by 18 hours in these simulations without the presence of radiation. It therefore appears that a vortex must have a deep layer of moisture before radiation becomes less important in its development. It is worth noting that RAD_Strong_MOIST_LL simulation actually takes longer to undergo TCG than the RAD_Strong simulation, which has no low-level moisture anomaly. It is likely that this is due to some combination of a subdued latent heat flux from the sea surface and weaker nocturnal radiative cooling in the disturbance's surrounding environment (not shown). Although the enhanced low-level moisture promotes strong convection at first, it is likely that these processes delay the formation of upper-level moisture and thus TCG.

To further validate the conclusion that radiation makes less of a difference once the core of a vortex is sufficiently moist, we "restart" the RAD_Weak simulation after 66 hours and shut radiation off at that point. In other words, we run a simulation which has radiation for the first 66 hours and then continues without it thereafter. This simulation is named RAD_Weak_Remove because radiation is removed during its evolution. The objective of this is to see if 66 hours of radiative forcing in this framework provides sufficient deep moistening to allow for TCG to occur. With radiation left on, TCG happens just hours after this point, and without radiation from the beginning at least another 54 hours passes without TCG occurring.

Figure 3.9 provides the same time series as Figure 3.1, but for all 3 “Weak” vortex cases, including the recently described run where radiation is switched off. TCG occurs just 6 hours after radiation is disabled (see Table 3.2), lending support to the conclusion that the influence of radiation for the first 66 hours “primes” the vortex for TCG. This must be true because the simulation which began without radiation (NORAD_Weak) is unable to undergo TCG within 5 days. To indicate the role that radiation plays for the first 66 hours in this framework, Figure 3.10 shows difference fields of RH and ice mixing ratio between RAD_Weak and NORAD_Weak at the point where radiation is turned off in RAD_Weak_Remove. Clearly radiation forces deep moistening in the core of the vortex, and a robust canopy of ice is a noticeable byproduct of this. The five supplementary simulations introduced in this section provide support that, in our modeling framework, radiation primarily serves to moisten the core over a deep layer in preparation for TCG and is much less important thereafter.

3.4 Conclusions

This work undertakes a numerical modeling investigation of the influence of longwave and shortwave radiation on tropical cyclogenesis (TCG) for varying strengths of initial vortices, with the aim at understanding when radiation is most important in promoting TCG. This is done by running simulations with and without radiation for three different initial vortices. We find that for a weak vortex, TCG occurs in about 3 days with radiation but is inhibited for more than 5 days without radiation. For the two stronger initial vortices, TCG is able to occur with and without radiation within 4 days, but experiences a delay of about 2 days without radiation included, suggesting that a strong vortex still requires the influence of radiation to undergo TCG rapidly. A strong diurnal cycle of convective activity is evident in our simulations, consistent with previous observational and modeling studies (e.g. Davis and Ahijevych 2012; Dunion et al. 2019; Gray and Jacobson Jr 1977). We also

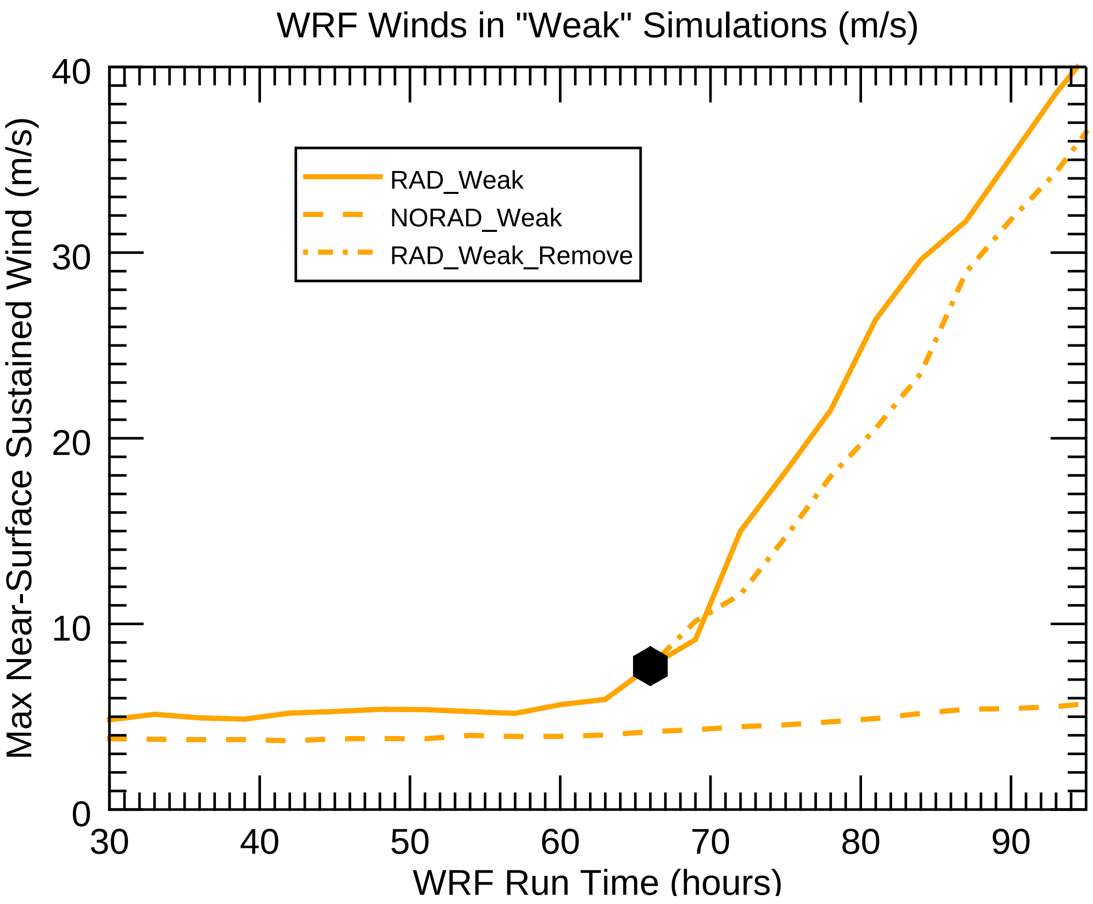

Figure 3.9: As in the left panel of Figure 3.1, but for the 3 "Weak" simulations. The solid and dashed curves are exactly the same as those pictured in Figure 3.1. The dot-dash curve shows a simulation which ran with radiation for the first 66 hours, at which point radiation is turned off. This point is marked with the black hexagon.

find that radiation does not have an appreciable effect on the timing of early intensification (reaching tropical storm and hurricane status) in our modeling framework.

We find that for an equal initial vortex, simulations with radiation develop deep moisture anomalies (extending into the middle troposphere) and hydrometeor canopies faster compared to their counterparts without radiation. This finding is largely consistent with the results of Nicholls (2015), who found that simulations with radiation tend to have increased RH and increased low-level cyclonic circulation. A differential radiative forcing between the cloudy disturbance core and its clear-sky surroundings appears to be important in providing

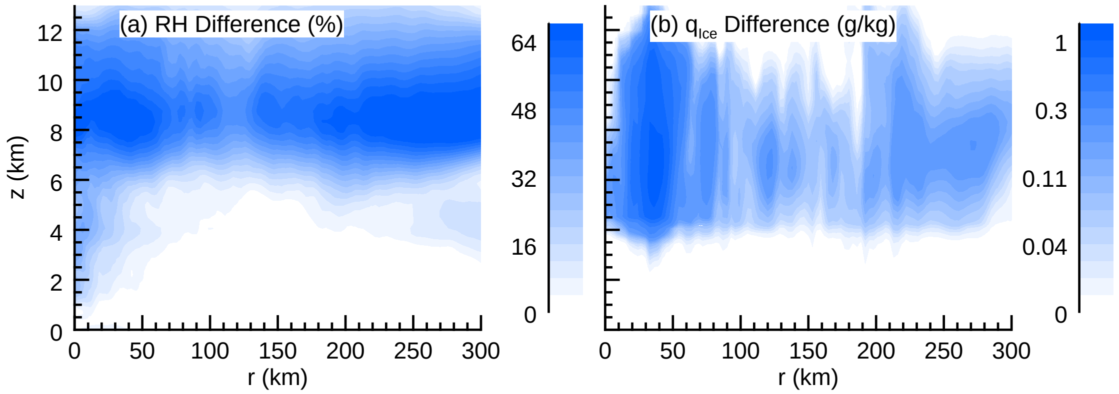

Figure 3.10: Azimuthally averaged cross sections of the difference in (left) RH and (right) ice mixing ratios between the RAD_Weak and NORAD_Weak simulations at 66 hour run time. It is after this time that radiation is turned off in the RAD_Weak_Remove simulation.

enhanced moisture for the disturbance and destabilizing the core, similar to the mechanism described by Gray and Jacobson Jr (1977). Convergence of low-level moisture provides an avenue for deep moistening of a tropical disturbance. Once the core is sufficiently moistened in a deep layer, the impact of radiation recedes, which we show through additional simulations which are pre-moistened as well as a simulation where radiation is turned off just prior to TCG occurring.

It stands to reason from the arguments presented herein that radiation has the largest influence on TCG at very early stages of a disturbance's development. It also emerges that its primary influence is to provide a catalyst for deep moistening in the core, since radiation does not play a significant role once the core is moistened in a deep layer. This work shows the importance of accurately simulating radiation and moisture in operational models, and provides insight into how much care should be taken to consider radiative processes at different stages of a TC's development. We expect that radiation's influence is strongest for disturbances which have broad clear-sky regions surrounding them, as that favors a heightened low-level moisture convergence from the surroundings. Additional work is required to validate these conclusions in other modeling frameworks and with different choices of physics schemes. A forthcoming publication will examine the relevance of these findings on a numerical modeling case study of the formation of a real hurricane.

Chapter 4

The Role of Radiation in the Genesis of Atlantic Hurricane Matthew (2016)

In Chapter 3 we confirm that radiation accelerates TCG in idealized simulations performed with the WRF-ARW model. We find that radiation's primary role is to moisten the core of a disturbance in a deep layer. Once the core is nearly saturated and a vortex is sufficiently strong, radiation no longer plays an influential role in TCG. In this chapter we perform case study simulations of Atlantic Hurricane Matthew (2016) to investigate the validity of these conclusions for a real event. This chapter is adapted from Smith et al. (2020) (full citation given below) which will be submitted to a journal for peer review in the summer of 2019.

Smith, W. P., Nicholls, M. E., Pielke Sr., R. A. and Thompson, G. (2020), 'The role of radiation in the genesis of Atlantic Hurricane Matthew (2016) (in preparation).'

4.1 Introduction

Hurricanes are devastating storms which take significant tolls on human life and property in coastal areas every year. Considerable efforts have been made to develop and improve numerical models for the prediction of a hurricane's eventual path and intensity. Hurricane formation is impossible without an organized cluster of clouds (known as a "tropical disturbance") developing into a "tropical depression" through a process known as TCG. It stands to reason that in order to continue to improve predictions of hurricanes, we must also continue to improve our understanding of TCG.

Numerous studies have shown recently that the presence of longwave and shortwave radiation (hereafter just “radiation” unless otherwise noted) dramatically accelerates TCG in both idealized (Nicholls, 2015; Nicholls et al., 2019a; Nicholls and Montgomery, 2013; Smith et al., 2019) and case study (Melhauser and Zhang, 2014; Tang and Zhang, 2016) numerical modeling simulations. This acceleration is thought to be due to a weak transverse circulation which develops due to a radial gradient of radiative cooling between a cloudy disturbance and its surroundings which are relatively devoid of clouds (Nicholls, 2015). This circulation tends to increase the RH of the core which promotes a diurnal cycle of convection that reaches peak intensity in the early morning hours. This mechanism is consistent with the arguments of Gray and Jacobson Jr (1977), and has also been observed for tropical MCSs (Dudhia, 1989; Miller and Frank, 1993) as well as mature TCs (Knaff et al., 2019).

In Chapter 3 it is shown that the presence of radiation in idealized numerical simulations is most important when a vortex is relatively weak, and that radiation’s primary role is to moisten the core of a developing disturbance, consistent with the transverse circulation mechanism discussed by Nicholls (2015). Once the core of a disturbance becomes nearly saturated from the surface into the middle troposphere, TCG tends to occur within a few hours and no longer exhibits any dependence on radiation (Smith et al., 2019). In this chapter we examine the validity of these conclusions by performing a case study of the genesis of Atlantic Hurricane Matthew (2016). Specifically, we test whether radiation has an impact on the timing of TCG and how this depends on the presence of moisture in the core of the disturbance.

4.1.1 Synoptic Overview of Hurricane Matthew

Hurricane Matthew was a Category 5 Atlantic storm that made devastating landfall in Haiti, Cuba, and the southeast coast of the United States in October 2016. Matthew began as a fast-moving easterly wave (20-25 kts) which exited the west coast of Africa on

September 23, 2016. A disturbance gradually formed within this easterly wave which was noted by satellite imagery and observations from reconnaissance aircraft to have well-defined mid- and upper-level circulations. Thunderstorm activity gradually organized and TCG was finally declared near the island of Barbados at 12Z on September 28 (Stewart, 2017).

Matthew reached a maximum sustained wind speed of 74.6 $m\ s^{-1}$ on October 1 at 0Z. The minimum in pressure was observed as 934 hPa by a dropwindsonde on October 4 at 0Z. Matthew was responsible for 585 direct deaths and the evacuation of roughly 4 million people from coastal areas. Total damages were estimated at $15 billion US dollars, including about $10 billion along the coasts of Florida, Georgia, and the Carolinas (Stewart, 2017).

In addition to the widespread destruction we mention in the previous paragraphs, Hurricane Matthew has been attributed to significant loss in retail sales in the southeastern United States (Aladangady et al., 2016). A survey conducted during this storm found that those in evacuation zones who were informed by trusted sources are more likely to heed the warnings and evacuate to safety (Wong-Parodi and Feygina, 2018). Because of the socioeconomic impacts of storms like Matthew, it is worthwhile to study the processes that lead to their development and intensification so that we may improve the quality of information that can be provided to citizens and encourage evacuations with more reliable lead times, as well as lessen the economic burdens on local businesses in remote coastal areas.

4.2 Methods

4.2.1 Numerical Model

The WRF-ARW model version 3.9.1.1 (Skamarock and Coauthors, 2008) is employed for the simulations presented in this study. The chosen physics schemes for our simulations include the Thompson microphysical parametrization (Thompson et al., 2008), the RRTMG longwave and shortwave radiation parametrization (Iacono et al., 2008), the YSU planetary boundary layer parametrization (Hong et al., 2006), the Betts-Miller-Janjic (BMJ) convective parametrization (Janjić, 2000) (for the 15 km grids only), and the Unified Noah land-surface scheme. Diffusion is chosen to act along model levels ($diff\_opt = 1$). Initial conditions and lateral boundary forcing are provided by the ECMWF-Reanalysis Interim (ERA-I) Project (ECMWF, 2009, updated monthly). The SST updates with the ERA-I reanalysis product as time progresses. The convective scheme is set to update every 5 minutes while the radiation schemes update every 1 minute. Although the latter is quite computationally expensive, we observe modest improvements in Matthew's track by running radiation at this frequency, compared to less frequent updates (not shown).

This chapter describes two simulations of Hurricane Matthew which are otherwise identical except that one of them has radiation activated while the other does not. The simulations are initialized at 18Z on September 25, 2016 and run until 0Z on September 30. They are outfit with two grids which have horizontal spacings of 15 km (hereafter "the coarse grid") and 3 km (hereafter "the nest"). The simulations use 60 vertical levels, the lowest of which is at about 100 m AGL and the highest of which is at 19.7 km AGL. The levels are vertically stretched with height in the boundary layer such that the spacing between them is about 70 m near the surface and reaches 377 m at an altitude of about 2 km AGL, after which the vertical spacing keeps this constant value to the model top. The size of the grids and the initial location of the nest in these simulations are shown in Figure 4.1. Feedback is enabled between the nest and the coarse grid.

The nest is specified to move towards the west-northwest as the simulation progresses using manual nest moves in order to keep the tropical disturbance within it as it tracks towards the Lesser Antilles and into the Caribbean. These moves are chosen such that the nest moves 15 km towards the west every 30 minutes and 15 km towards the north every 180 minutes. Attempts to use the built-in vortex-following utility in WRF-ARW were frequently unsuccessful; we attribute these struggles to the weak and disorganized nature of the initial vortex which is likely to confuse the algorithm, given it is designed to follow well-defined vortices.

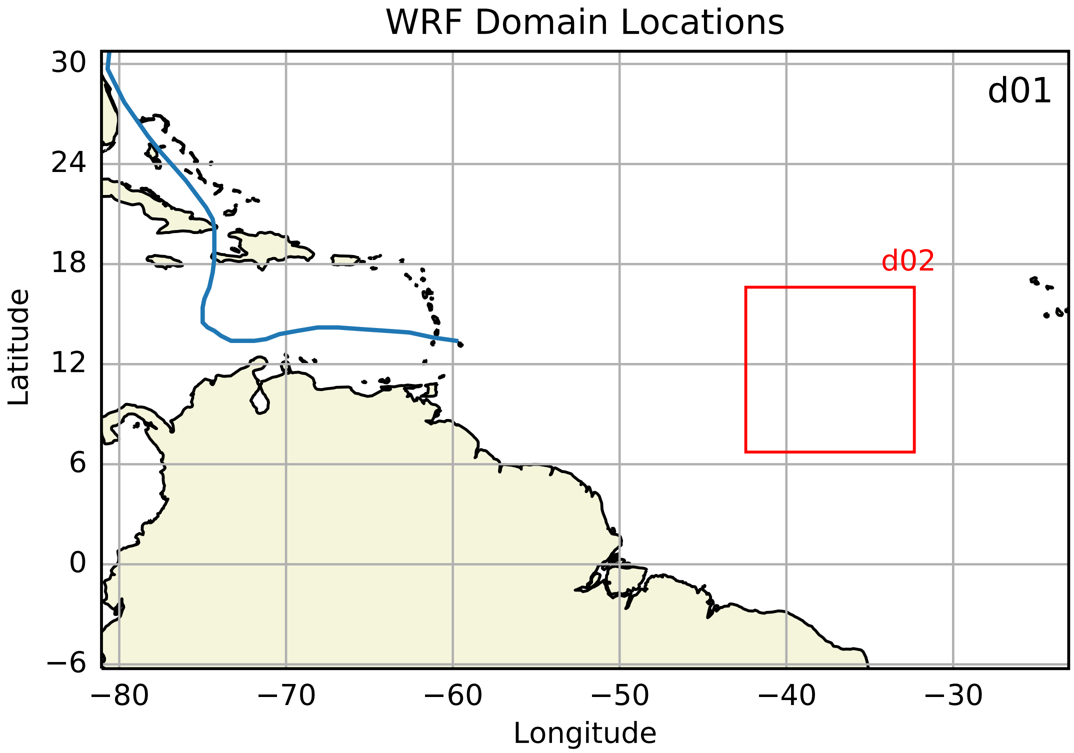

Figure 4.1: Location of the grids in the standard-resolution simulations. d01 has a grid spacing of 15 km and d02 has a grid spacing of 3 km. The blue line indicates the NHC's Best Track for Hurricane Matthew. d02 is specified to move towards the west-northwest with time to follow the developing disturbance.

4.2.2 Determining Track and Intensity

Center points used for tracking Hurricane Matthew and for computing azimuthal averages are determined by the following objective methodology. Sea level pressure is calculated using the hypsometric equation and is then smoothed with a 1-2-1 filter (as done in Nolan et al. 2009). We find that for our nested domains it is necessary to smooth this field 100 times but for the coarse grid it is only necessary to smooth 10 times, which is likely due to more convective chaos in the finer-spaced domain. For the coarse grids, the center point for Matthew is then chosen as the minimum smoothed sea level pressure within a 5° x 5° box centered on a "first guess" point. For grids with a horizontal spacing of 3 km, the minimum smoothed pressure in the entire domain is chosen as the center point.

At each model output step, a wind value is assigned to Matthew for comparison with observations and determining the evolution of its intensity. This value is chosen as the maximum tangential wind speed in the same 5° x 5° box used for determining the smoothed pressure minimum and in the lowest 3 model levels (below about 300 m AGL). The smoothed pressure center discussed in the previous paragraph is used for the calculation of tangential winds, with a positive sign convention given to cyclonic winds. A minimum pressure value is also assigned at each model output step as the un-smoothed sea level pressure value at the center point.

4.3 Results

Figure 4.2 shows time series of the track, wind and pressure from the simulations with and without radiation, with the National Hurricane Center (NHC) Best Track for Hurricane Matthew included for reference. Immediately it is evident that WRF does a reasonable job simulating Hurricane Matthew with this approach. In particular, the hurricane tracks are very near to the observed track (panel a) and the RAD simulation produces very realistic wind values for Matthew (panel b). The track is sensitive to radiation, which is consistent with the findings of Tang and Zhang (2016). The pressure field in RAD follows a similar rate of decline, but is a bit offset from the Best Track (panel c).

It is worth noting that although radiation does appear to accelerate the genesis of Hurricane Matthew slightly, the difference between simulations with and without radiation are not as drastic as would be expected by the literature (e.g. Nicholls 2015, Chapter 3), which is quite perplexing. In numerous other attempts to simulate Matthew with slightly different approaches (different physics schemes, grid spacing and location, etc.) we find that this conclusion emerged as well (not shown).

Figure 4.3 shows moisture cross sections from both the RAD and NORAD simulations at 18Z on September 26 (just 24 hours into the simulations). Both simulations show that water vapor mixing ratios in the boundary layer exceed 19 $g\ kg^{-1}$ in a broad area surrounding

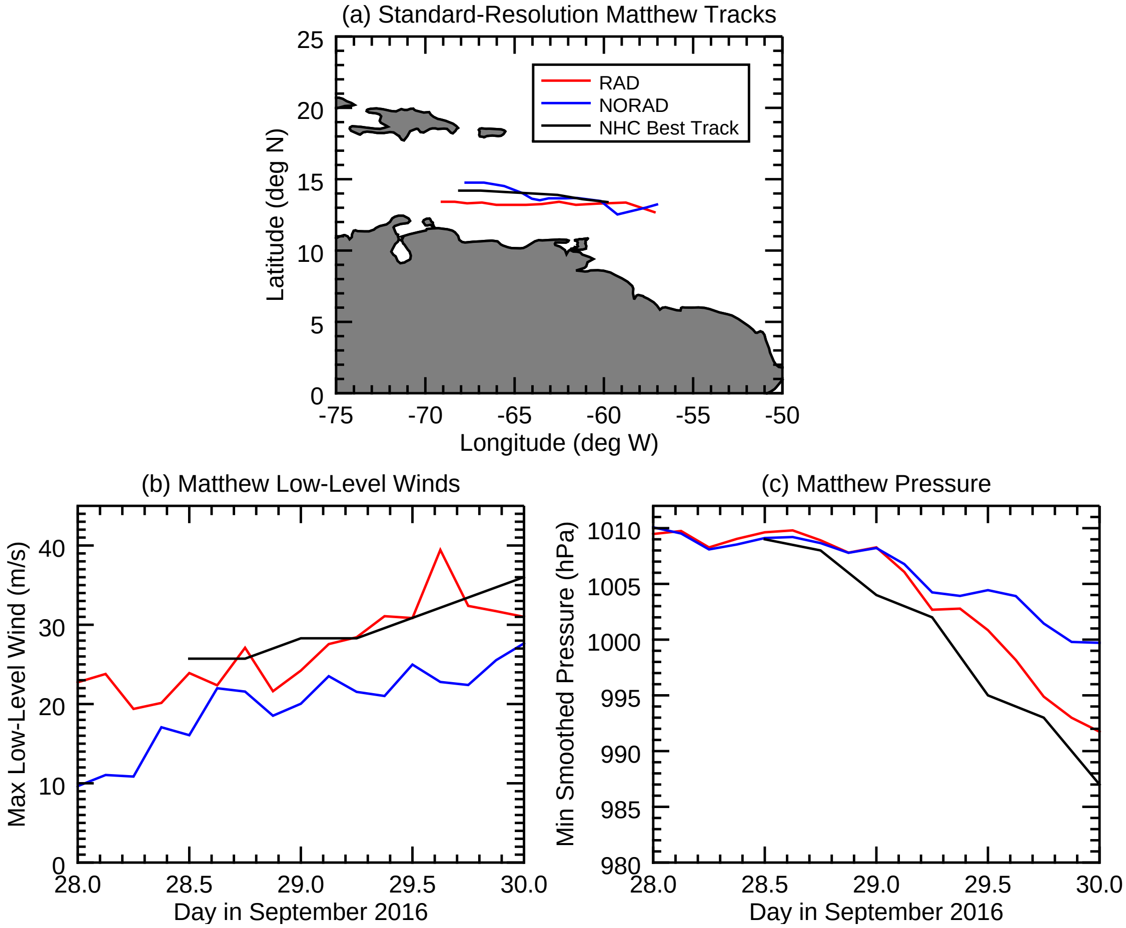

Figure 4.2: Time series of the (a) track, (b) wind speed and (c) un-smoothed pressure at the smoothed pressure minimum location from 12Z on September 28 to 0Z on September 30. Shown in red (blue) is the simulation with (without) radiation included, and the NHC's Best Track data are shown in black.

the disturbances (panels a and b). These moisture values are comparable to the "MOIST" runs we perform in Chapter 3, which show that with enough moisture in a deep layer and a sufficiently strong cyclonic vortex TCG is not accelerated by radiation. Near-saturation is already present from the surface into the mid-troposphere in both simulations at this time (panels c and d). These anomalously high values of moisture are coming directly from the ERA-I Project reanalysis product we use for the initial conditions in these simulations (not shown). The results from Chapter 3 suggest that radiation does not play a significant role in the development of Matthew from this point on, which is what we observe as these simulations evolve (Figure 4.2).

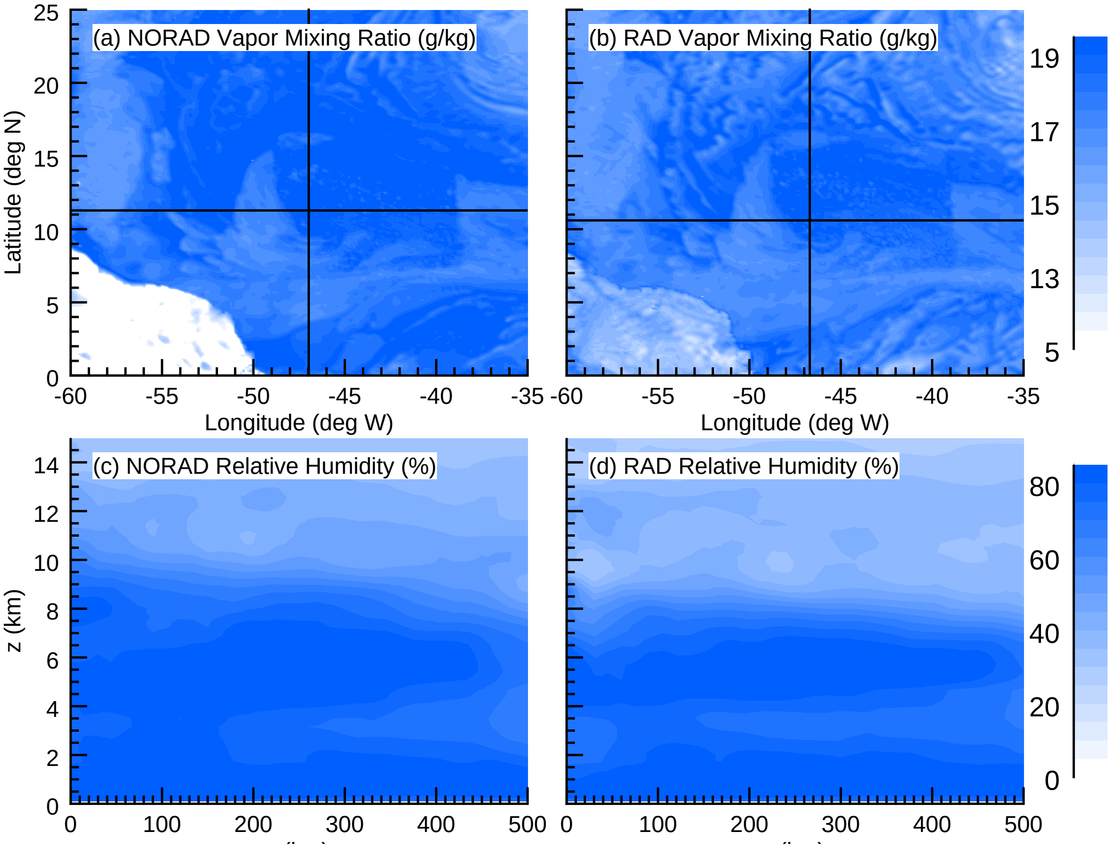

Figure 4.3: Cross sections taken from the both simulations. Shown are (top) horizontal cross sections of water vapor mixing ratio at the lowest model level (z = 97.9 m AGL) and (bottom) azimuthally averaged cross sections of RH from the (left) NORAD and (right) RAD simulations at 18Z on September 26. The center points for azimuthal averages are marked with the crosshairs in the top panels, which are determined by the methodology we provide in Section 4.2.2.

4.4 Conclusions

In this chapter we perform a case study on Atlantic Hurricane Matthew (2016) to investigate the role that radiation plays in its development. Our results indicate that radiation does not enact a large influence on the genesis of Atlantic Hurricane Matthew. We attribute this to the initial conditions provided by the ERA-I Project, which prescribe a very moist column near the tropical disturbance at the time the model is initialized. Based on the arguments we present in Chapter 3 (Smith et al., 2019), this excessive moisture mutes the effect that radiation has on the development of the TC. This further validates the hypothesis we provide in Chapter 3 that radiation primarily acts to moisten the core of a disturbance and once nearly saturated, radiation no longer plays an important role in TCG.

The penultimate chapter of this dissertation provides some insights into coauthor work which reinforces the analyses from this and the previous chapters. The final chapter summarizes the primary objectives and findings of this dissertation and provides some proposed avenues for continued study on these subjects.

Chapter 5

Relevant Contributions to Coauthor Publications

In this chapter we highlight relevant contributions to coauthor publications which further support the analyses and conclusions of the first-author publications given in Chapters 2, 3 and 4. Sections 5.1 and 5.2 simulate an idealized VHT and the formation of a coherent vortex from horizontally sheared winds, respectively, and are adapted from coauthor contributions to Nicholls et al. (2019b). Section 5.3 shares results from two simulations with and without radiation performed with the RAMS model and is adapted from Nicholls et al. (2019a). Coauthor contributions to two other publications (Nicholls et al. 2018 and Nair et al. 2019) are not included in this chapter in the interest of brevity.

5.1 Idealized VHT Simulation

VHTs are deep, rotating columns of cumulonimbus convection that allow for tropospheric heating and vertical mass transport which contribute to a stratiform anvil region aloft (Hendricks et al., 2004; Montgomery et al., 2006). VHTs preferentially develop positive vorticity around the edges of the shallow surface cold pools that form in their downdraft region (Nicholls and Montgomery, 2013). This positive vorticity is approximately as deep as the cold pool it surrounds, both roughly 300 m in height. Low-level vorticity generated in this way is important because it enriches the low-level environment with anomalously high vorticity, which can be stretched into even stronger vorticity anomalies in later convective activity (discussed in Chapter 2 and later in Section 5.2).

A RAMS simulation is initialized with a vortex of 12 $m\ s^{-1}$ peak wind speed and a 50 km radius of maximum winds (RMW) at an altitude of 6 km AGL. The model consists of two nested grids, the coarser of which has 200 horizontal grid points spaced at 3 km, and the finer of which has 202 horizontal grid points spaced at 750 m. Each grid has 55 vertical grid points, with the lowest point at 29.5 m AGL and a model top at about 23 km AGL. The vertical spacing between levels is stretched from about 60 m near the surface to until it reaches 700 m at a height of about 9 km AGL, above which it is kept constant. All of the following analyses are performed on the finer spaced grid.

An idealized VHT is created in this domain from a shallow surface warming of 2°C and moistening of 2 $g\ kg^{-1}$ applied over the first 5 minutes 25 km due east of the model center. The warming and moistening perturbation in this simulation provides sufficient forcing to create a VHT that spans the depth of the troposphere. Figure 5.1 shows vertical cross sections of the VHT at a run time of 15 minutes as the cell ascends into the mid-troposphere. As the warm air rises (Figure 5.1c), a dipole of vorticity is created from the tilting of horizontal vorticity into vertical vorticity (Figure 5.1e). The sign of the stretching term is positive initially at low levels since horizontal convergence occurs as the air rises (Figures 5.1b, 5.1d). Vorticity created from these sources is then advected vertically by the updraft (Figure 5.1f), inspiring the column to rotate (Figure 5.1a). Because of the phase changes that occur in the column, a strong diabatic heating is present there on the order of 100 J $\mathrm{kg}^{-1}\ \mathrm{s}^{-1}$ (not shown) which further promotes rising motion.

Figure 5.2 shows horizontal cross sections taken at the lowest model level at a model run time of 25 minutes. At this time, a small region of positive vorticity is present at the bottom of the column (Figure 5.2a), coincident with a modest region of stretching and convergence (Figure 5.2b and 5.2c). This convergence is the result of the rising column of air above, which demands a low-level horizontal inflow for mass continuity. The horizontal advection (Figure 5.2d) field shows the influence of the local inflow, which is accented in the meridional direction because of the mean flow surrounding the cell. The positive negative/dipole in this

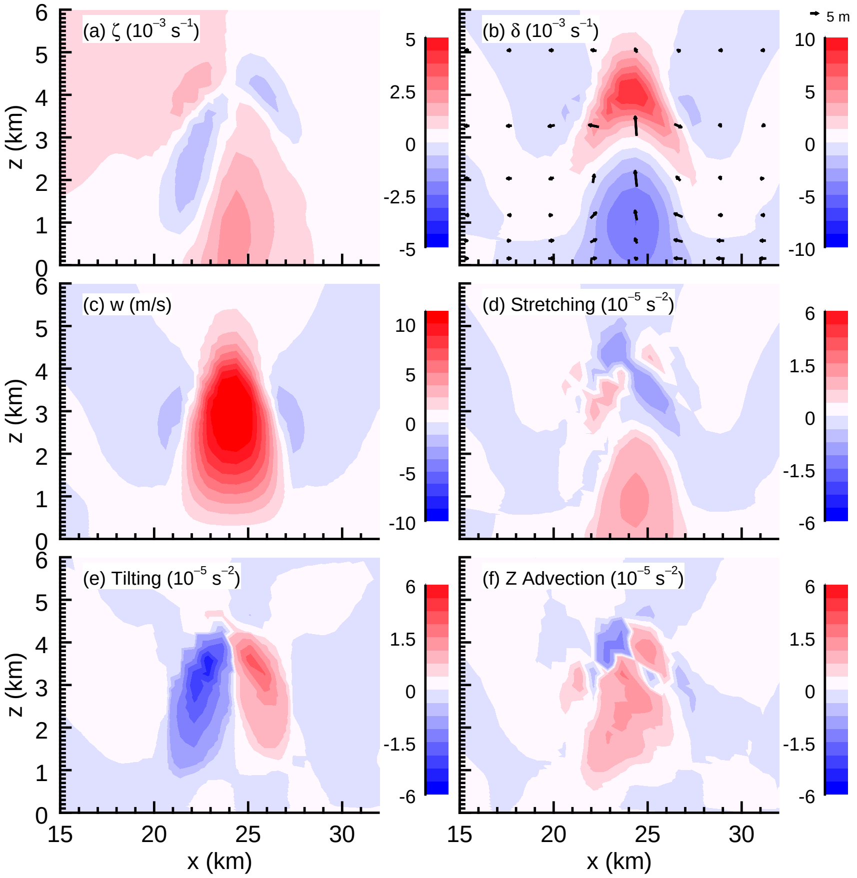

Figure 5.1: Vertical cross sections of (a) vertical vorticity ζ, (b) horizontal divergence δ, (c) vertical velocity, and the (d) stretching, (e) tilting and (f) vertical advection terms from Equation 2.3 taken through the center of the VHT at a model run time of 15 minutes. Vorticity and divergence fields are both scaled by $10^3\ s^{-1}$, and all terms are scaled by a factor of $10^5\ s^{-2}$.

field is the result of $\frac{\partial \zeta}{\partial y}$ changing signs in a near southerly flow.

After 30 minutes of run time, the collision and coalescence processes in the VHT force raindrops of sufficient size to fall through the lower portion of the column, which causes cooling from latent heat absorption as some liquid water is converted back into vapor. This forms a cool downdraft which first reaches the surface at 35 minute run time, creating a shallow cold pool (shown later in Figure 5.4). The cold pool is approximately 3 K cooler than the ambient environment when it forms, but weakens as it spreads out horizontally and

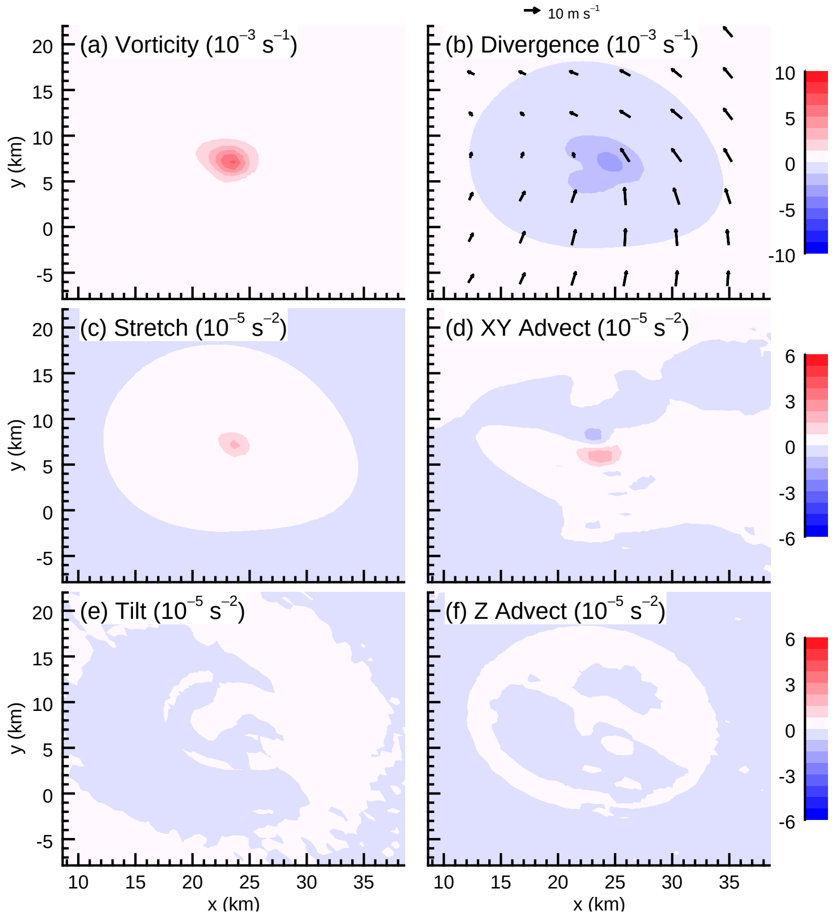

Figure 5.2: Horizontal cross sections of (a) vertical vorticity ζ, (b) horizontal divergence δ, and the (c) stretching, (d) horizontal advection, (e) tilting, and (f) vertical advection terms from Equation 2.3 taken at a model run time of 25 minutes at the lowest model level (z = 29.5 m AGL). Vorticity and divergence are both scaled by a factor of 10^3 s^{-1}, and all terms are scaled by a factor of 10^5 s^{-2}.

the downdraft gradually subsides. This temperature depression is consistent with other observational and modeling studies of cold pools in tropical environments (Drager and van den Heever, 2017; Eastin et al., 2012). The downdraft also causes divergence at the surface in the cold pool region. However, at the edges of the cold pool, the horizontal wind experiences convergence as the strong outflow interacts with the ambient larger-scale circulation.

Figure 5.3 shows the same fields as in Figure 5.2, but is taken 15 minutes later at a model run time of 40 minutes. The x and y axes are shifted because the VHT is propagating along with the mean flow, and the plot bounds are manually chosen to follow the feature of interest. The positive (red) region in Figure 5.3b indicates divergence which is surrounded by a negative (blue) ring indicating convergence. It is worth noting that the convergence is stronger on the southeast side of the outflow as compared to the northwest side, which is due to the mean vortex flow opposing the outflow direction on the southeast side, thereby heightening the values of convergence there (see the wind vectors in Figure 5.3b). Similarly, the stretching term (Figure 5.3c) shows a ring of positive values coincident with the region of convergence. The vorticity field (Figure 5.3a) shows a striking similarity to the stretching term, suggesting that this term is the primary driver in generating the low-level vorticity at the edge of the VHT outflow.

It is evident from the similarity in the vorticity and stretching term fields from Equation 2.3 that the ring of positive vorticity is created by the stretching of ambient vorticity in the domain. While horizontal advection appears to play a role, this term's only contribution is moving the generated vorticity around in the model and spreading it out from the center of the downdraft region. The vertical component of advection is isolated in Figure 5.2f and it is shown to be negligible at the outflow edge, indicating that there is no appreciable vertical transport of vorticity. The weak vertical velocities near the model surface also prevent the tilting term from being important in generating the ring of vorticity at the VHT outflow edge (Figure 5.3e).

As the simulation progresses, the VHT continues to cycle slowly about the domain center. The downdraft gradually weakens since most of the eligible hydrometeors fall out by one hour run time, which causes the cold pool to weaken in magnitude. The outflow continues to spread radially from the downdraft region, which weakens the wind speeds at the outer rim of the cold pool. The stretching term and the vorticity fields also weaken at the outflow edge from the diminishing fuel source and the increase in horizontal span. Figure 5.4 shows horizontal cross sections of vorticity and perturbation potential temperature, giving an overview of this slow weakening process as well as the horizontal advection of the feature

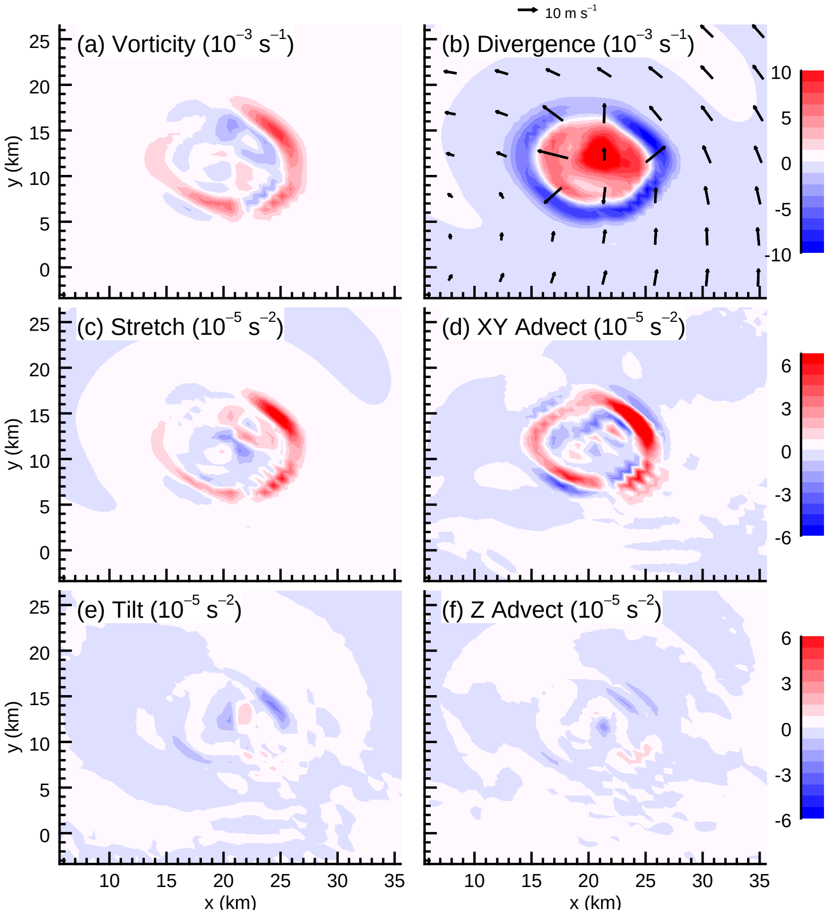

Figure 5.3: As in Figure 5.2, but at a model run time of 40 minutes.

with time. The ring of vorticity continues to weaken over an additional hour as the downdraft ceases entirely and the system reestablishes equilibrium (not shown).

This section shows the generation of enhanced vorticity around the edge of a shallow surface cold pool. An analysis of the vorticity equation (Equation 2.3) indicates that the stretching term is the dominant driver in enhancing vorticity to values considerably larger than those in the ambient environment. This term is important at the edge of a cold pool because spreading winds in the cool outflow converge there with winds from the larger-scale circulation, which thereby concentrates vorticity by stretching. In the next section, we consider how this vorticity may deepen through the presence of new convection to create the

LCVA structures discussed in Chapter 2.

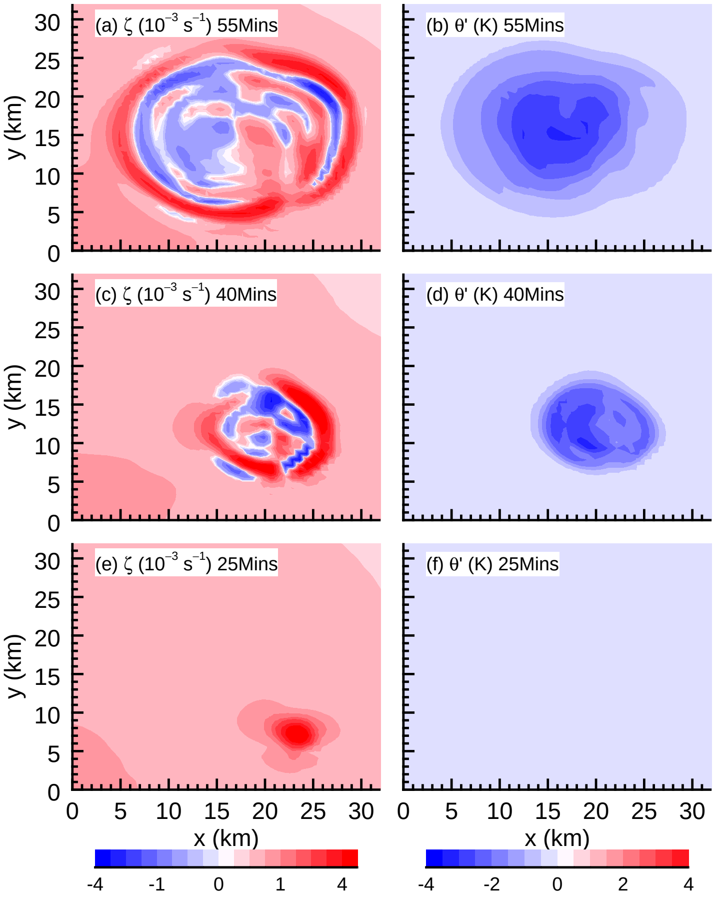

Figure 5.4: Horizontal cross sections of (left) vertical vorticity ζ and (right) perturbation potential temperature taken at the lowest model level (z=29.5 m AGL) at times of (bottom) 25, (middle) 40, and (top) 55 minutes of model run time. Vorticity fields are scaled by a factor of $10^3\ s^{-1}$.

5.2 Idealized LCVA Simulation

The previous section shows that enhanced regions of low-level vorticity can develop at the edges of convective cold pools when embedded in a weak vortex. This section illustrates how enhanced low-level vorticity might influence the TCG process. The vorticity generated at the edges of cold pools is primarily “shear vorticity”, meaning it is the result of a change in wind across a horizontal boundary. We show experimentally that shear vorticity can be converted into "curvature vorticity," which signifies rotation about an axis, by simply adding a heat source. The mathematical foundation for these arguments is given in Section 2.4.

To show the production of curvature vorticity from shear vorticity, a RAMS simulation is initialized with a horizontal shear region, with easterly winds to the north and westerly winds to the south of the model center. These winds are 5 $m\ s^{-1}$ in magnitude and the horizontal transition from westerly to easterly winds occurs over approximately 6 km. The winds are strongest at the surface and gradually reduce to zero at a height of 300 m. This initial wind field results in a region of purely shear vorticity. A constant heating rate is applied below 6.5 km in the center of the wind transition to force a rising column. This simulation's only grid consists of 100 horizontal grid points spaced at 750 m. There are 55 vertical levels set up identically to those of the idealized VHT simulation presented in Section 5.1.

Figure 5.5 shows horizontal cross sections at 0 and 30 minutes of run time, illustrating the evolution of vorticity in the model domain. The left 3 panels of Figure 5.5 show that initially, the region of vorticity found among the horizontal wind gradient (Figure 5.5a) is entirely shear vorticity (compare 5.5c and 5.5e). After 30 minutes, the center of the feature is marked with a region of particularly strong vorticity (Figure 5.5b). A comparison of panels d and f indicates that this "vorticity anomaly" now contains a pronounced quantity of curvature vorticity, whereas no curvature vorticity is present there at the beginning of the simulation (Figure 5.5c).

Figure 5.6 shows a vertical perspective of the enhanced vorticity that is created in this simulation. The surface heating induces a convective tower to form, not unlike the VHT we discuss in Section 5.1 (Figure 5.6a and 5.6b). The vertical velocity stretches vorticity in the column (Figure 5.6c) which is then advected upwards in the updraft. Tilting also plays a role in converting horizontal vorticity into vertical vorticity (Figure 5.6d). One fundamental difference between the VHT produced in the previous simulation and this "vorticity anomaly"

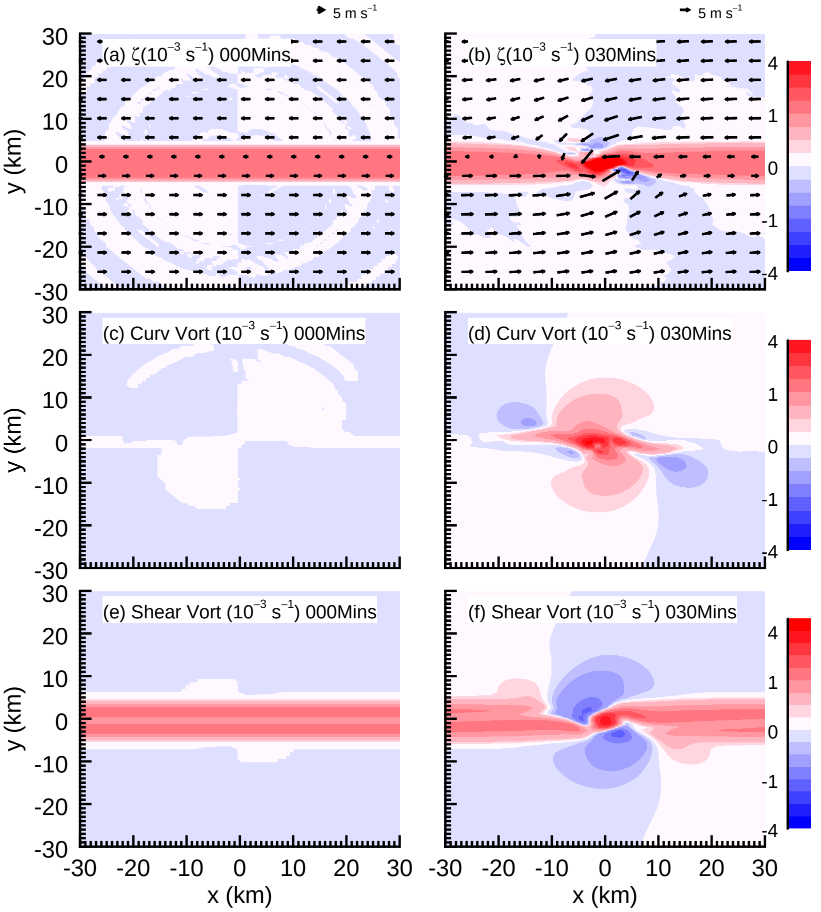

Figure 5.5: Horizontal cross sections of (top) vertical vorticity ζ, (middle) the curvature component of vorticity, and (bottom) the shear component of vorticity taken at a model run time of (left) 0 and (right) 30 minutes at the lowest model level (z=29.5 m AGL). Panels c-f have been smoothed once with a 1-2-1 filter. All fields are scaled by 10^3 s^{-1}.

is that the maximum vorticity is found at the surface in this case, and this idealized "vorticity anomaly" (which we term an LCVA in Chapter 2) does not span the entire depth of the troposphere. In addition, this feature tends to persist for much longer than a typical VHT, which is discussed at length in Chapter 2.

In this section we show how discrete vortices made up of "curvature vorticity" may be created from regions of purely "shear vorticity." A simulation is considered where a heat source is added to the center of a shallow region with a horizontal wind shift. It is shown

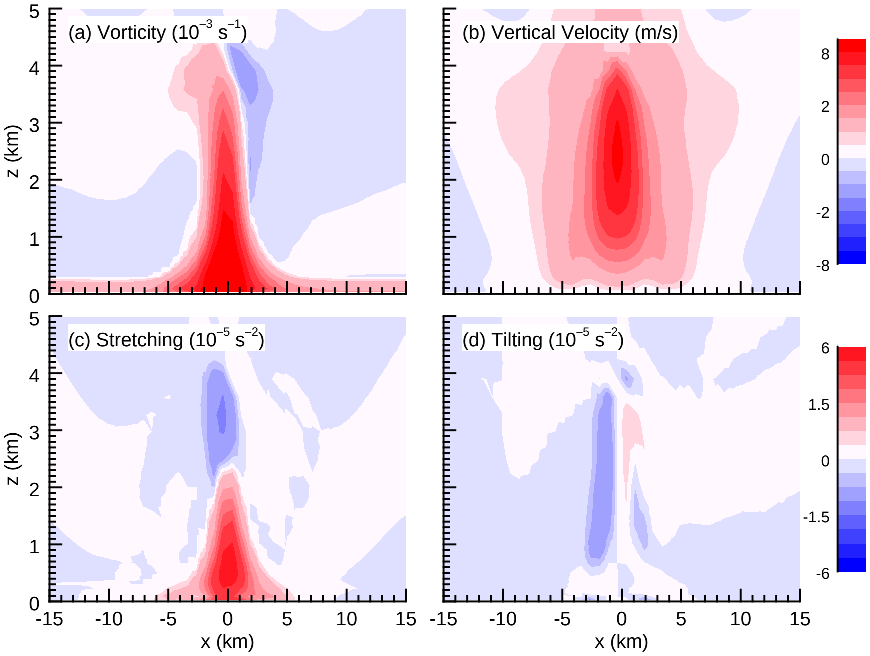

Figure 5.6: Vertical cross sections of (a) vertical vorticity ζ, (b) vertical velocity, and the (c) stretching, and (d) tilting terms from Equation 2.3 taken at a model run time of 20 minutes through the center of the model domain. Vorticity is scaled by a factor of 10^3 s^{-1}, and the terms are scaled by a factor of 10^5 s^{-2}.

that the heat source alone, which drives a column of convection, may generate a column of curvature vorticity which extends to mid-levels and has maximum vorticity near the surface, as seen in LCVAs in Chapter 2.

5.3 Sensitivity to Radiation in RAMS

In Chapter 2 and Sections 5.1 and 5.2 we show the formation process and importance of low-level vorticity in idealized numerical modeling of TCG. However, all of those simulations are performed without radiation, which has been shown to significantly accelerate TCG in both idealized models (e.g. Nicholls 2015; Nicholls and Montgomery 2013) and in real-event case studies (e.g. Melhauser and Zhang 2014; Tang and Zhang 2016). In an effort to illustrate this accelerated development rate, two idealized RAMS simulations are undertaken. One simulation does not include radiation schemes (hereafter “NORAD”) while the other uses radiation schemes (hereafter “RAD”), but the two are otherwise identical. A comparison of these simulations illustrates the exact role that radiation plays in TCG. All of the RAMS model details from Section 2.2 are also employed in these simulations, except as otherwise noted in the next paragraph.

A mesoscale convective vortex is initialized with an RMW of roughly 140 km, with maximum winds of 8 $m\ s^{-1}$ at a height of about 4 km AGL. Both simulations contain three nested grids in the domain which have horizontal grid spacings of 24 km (170 x 170 points), 6 km (202 x 202 points) and 2 km (353 x 353 points). All grids have 58 vertical grid points which are vertically stretched from the lowest model level at 29.5 m AGL to roughly 10 km AGL, after which the spacing remains constant to the model top at 24.3 km. Only output from the middle grid (spaced at 6 km) is considered in this analysis. The domain is located at 40°W longitude and the simulation is initialized at 12Z (corresponding to a model run time of 0 hours, this day is henceforth referred to as Day 1), which is morning in the tropical Atlantic. The radiation scheme employed in RAD is the Harrington long- and shortwave scheme (Harrington, 1997), which has 5 infrared and 3 solar wavelength bands.

Figure 5.7 shows a time series from both simulations of the maximum azimuthally averaged tangential wind at the lowest model level (z=29.5 m AGL). It is immediately evident that radiation accelerates the rate of TCG in these simulations. Until about 18 hour model run time (6Z on Day 2), neither disturbance appears to be intensifying. After this time, the winds in RAD begin a slow rise and at a model run time of 66 hours they begin a rapid climb. In contrast, the winds in NORAD show only marginal development over the first 120 hours of run time.

We now examine the difference in wind fields and convection in the two simulations. Figure 5.8 shows azimuthally averaged fields of tangential wind and total hydrometeor mixing ratio at a model run time of 60 hours (0Z on Day 4). The RAD simulation has developed a very robust anvil region from the presence of numerous VHTs (Figure 5.8c). Two distinct

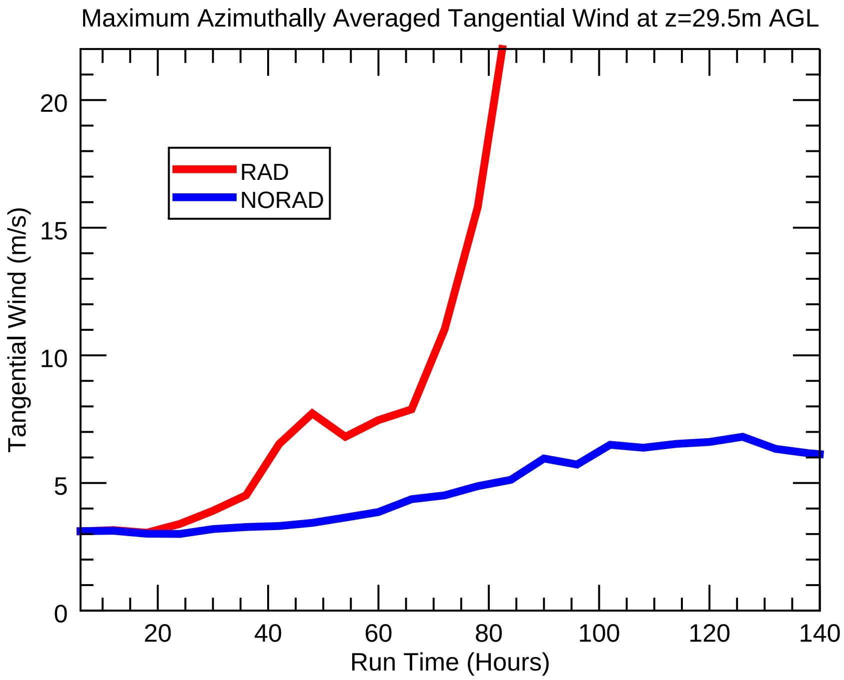

Figure 5.7: Time series of the maximum azimuthally averaged tangential wind at the lowest model level (z=29.5 m AGL) in the (red) RAD and (blue) NORAD simulations.

maxima exist in the wind field, one at low levels with an RMW of about 140 km, and a newly developed MLV with an RMW of about 100 km, which is stronger than the low-level circulation (Figure 5.8d). A MLV primarily forms from sublimation at the base of the stratiform ice region (Nicholls et al., 2018), and such a vortex has thus not formed in the NORAD simulation because its anvil region is much less developed than that of the RAD simulation (Figure 5.8a). The NORAD simulation eventually develops a noteworthy MLV by 120 hour model run time (not shown), once the anvil region becomes more pronounced.

Figure 5.9 shows the same fields as in 5.8, but is taken 24 hours later at a model run time of 84 hours (0Z on Day 5). By this time, the RAD simulation has undergone TCG and become a weak tropical storm. This is evidenced both by pronounced hydrometeor mixing ratios in a vertical column within 50 km of the model center (Figure 5.9b) and a deep region of tangential winds exceeding 20 $m\ s^{-1}$ (Figure 5.9d). The NORAD simulation shows only

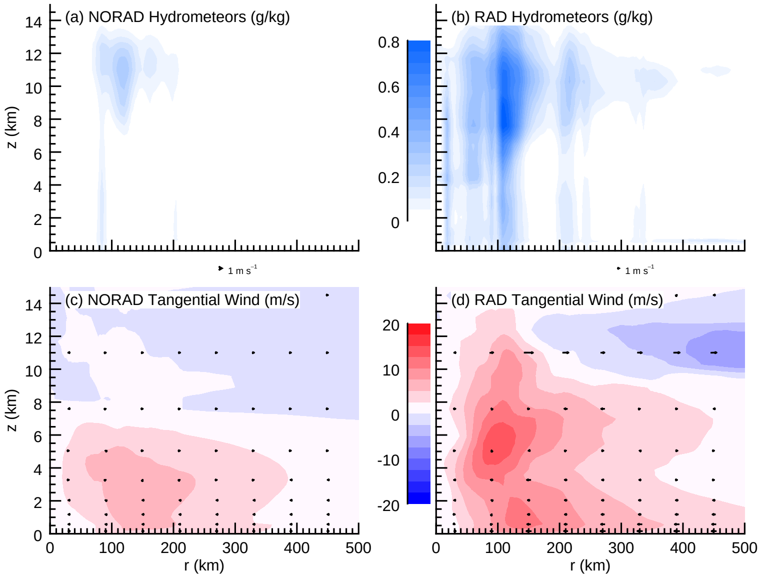

Figure 5.8: Contour plots of (top) total liquid and ice hydrometeor mixing ratio and (bottom) tangential wind azimuthally averaged about the model center from the (left) NORAD and (right) RAD simulations taken at a model run time of 60 hours.

marginal signs of development; the surface winds have increased modestly but the RMW at low levels has not contracted from its original value (Figure 5.9c).

In the RAD simulation, clear sky radiative cooling at night helps create an instability which favors morning VHTs. Gray and Jacobson Jr (1977) noted observationally that tropical convective activity has a maximum in the morning. The differential radiative forcing between the cloudy and clear sky regions furthers convection which enhances the core's RH, thus accelerating TCG. The NORAD simulation does not have longwave radiation included, so there is no additional differential radiative forcing mechanism active to promote convection. Instead, this simulation sees a delay in widespread convection until sea surface fluxes build up enough heat and moisture to generate sufficient instability. Once convection begins, further convection is likely favored due to VHT outflow convergence at low levels.

In this section we show that a simulation with radiation (RAD) underwent TCG on a realistic time scale (≈3 days) from a parent vortex whereas an otherwise identical simulation

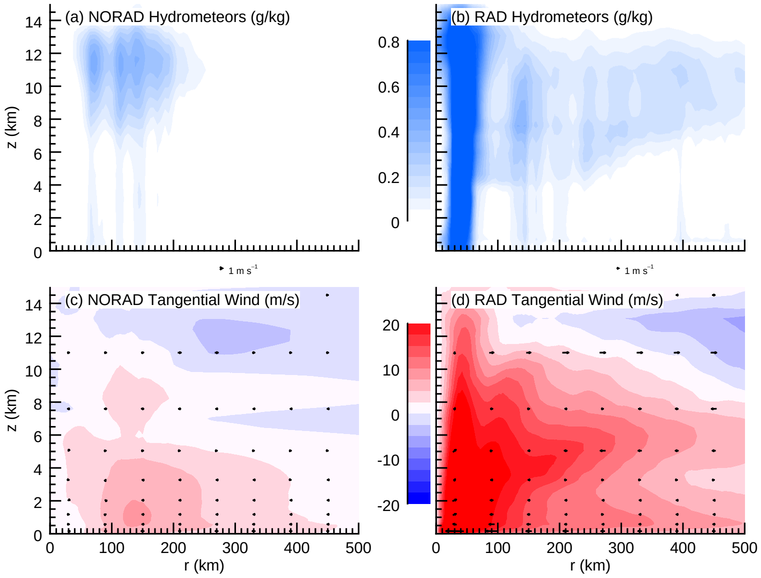

Figure 5.9: As in Figure 5.8, but at a model run time of 84 hours.

without radiation (NORAD) shows only marginal signs of development over this time period. The presence of radiation creates differential radiative forcing between the cloudy and clear regions, helping to accelerate convection and the rate of TCG. Convection is suppressed almost entirely in NORAD due to the lack of this radiative mechanism, thus delaying the formation of an expansive anvil region, a pronounced MLV which is observed in RAD, and TCG.

Chapter 6

Conclusions

In this dissertation we explore two important aspects of TCG: the roles played by radiation and low-level vorticity. This chapter restates the overarching research questions which guide the approach we take, summarizes all of the important findings from our research questions, and provides some avenues for future areas of research facilitated by these findings.

6.1 Objectives

The work of Nolan (2007) showed that as TCG occurs, a small concentrated vortex "appears" in the center of a larger-scale circulation. Chapter 2 of this dissertation examines the origin of such a vortex from shallow, enhanced vorticity at the edges of convective cold pools. These vortices, termed low-level convectively-induced vorticity anomalies (LCVAs), are investigated for their production of curvature vorticity as well as their tendency to undergo vortex merger events.

It has been shown that radiation dramatically accelerates TCG in numerical models (e.g. Nicholls 2015), however the importance of radiation in certain "stages" of TCG has yet to be explored. In Chapter 3, we perform numerical simulations to show radiation's primary influence in TCG. Otherwise identical simulations with different initial vortex strengths and different background moisture profiles are performed to understand the propensity for radiation to accelerate TCG.

In Chapter 4, we attempt to understand how radiation impacts the development of a real hurricane. Otherwise identical simulations with and without radiation are performed of Atlantic Hurricane Matthew (2016) to explore the change in TCG time. As in Chapter 3, the role of inner core moisture is also explored to highlight how it affects radiation's influence on this process.

6.2 Key Findings

In Chapter 2 we explore the theory of low-level vorticity generation in a full simulation of TCG, where low-level convectively-induced vorticity anomalies (LCVAs) of positive sign are shown to form at low levels and circulate around the center of a larger-scale vortex. Such LCVAs originate from the stretching of ambient vorticity in VHT cold pool outflows, but become deeper and persist much longer than those at the edges of VHT outflows. As time progresses, the low-level environment becomes more vorticity-rich and more conducive for LCVAs to form, and eventually one LCVA is able to sustain itself in the center of the larger-scale circulation and becomes the low-level core of an intensifying TC. The creation of curvature vorticity from shear vorticity and the presence of vortex merger events are examined quantitatively through the calculation of budget equations. It is hypothesized that additional sources of low-level vorticity and a stronger mid-level circulation above which enhances local vertical wind shear are mechanisms that allow LCVAs to retain their strength longer as the simulation evolves.

Sections 5.1 and 5.2 explore the role of low-level vorticity generation on idealized TCG simulations and supplement the arguments presented in Chapter 2. It is shown that in an environment pre-enriched with vorticity, VHTs preferentially generate positive low-level vorticity at the edges of their convective downdraft outflows. This vorticity is created from the stretching of ambient vorticity brought about by the convergence of air where the low-level VHT outflow meets the larger-scale vortex flow (Section 5.1). When acted upon by convection, shallow vorticity produced in this way may deepen to form a coherent, more circular vortex. This is shown in an idealized simulation where a heat source is applied to a region of horizontally sheared winds, which causes the initial “shear vorticity” to convert to “curvature vorticity” (Section 5.2) and form an LCVA.

In Chapter 3 we examine the role of radiation in accelerating TCG in idealized simulations. This is done by performing several simulations using the WRF model which test the response of TCG to changes in initial vortex strength and the background moisture profile. It is found that the stronger an initial vortex, the less influential radiation is in TCG. Radiation is most important when a vortex is fairly weak and does not have a very moist core. The primary role of radiation is to moisten the core of a tropical disturbance in a deep layer, and after the core is nearly saturated and a vortex is sufficiently strong, radiation no longer plays an influential role in accelerating TCG. This hypothesis is confirmed through supplementary simulations which are run with a strong vortex and a moist vapor profile, as well as a simulation where radiation is shut off after the core is nearly saturated to show that TCG can still readily occur after that point, even without radiation.

Further validation of the arguments presented in Chapter 3 are provided in Section 5.3. Otherwise identical simulations with and without radiation performed with the RAMS model confirm in a different framework that radiation is extremely influential in TCG. A simulation with radiation undergoes TCG within about 3 days, while a simulation without it hardly shows any evidence of development over this time period. The formation of a robust ice canopy with radiation allows for a differential radiative forcing mechanism to act between the disturbance and the surrounding cloud-free region which provides extra moistening to the core, thus favoring more convection and therefore TCG.

In Chapter 4 we perform a case study of Atlantic Hurricane Matthew (2016) in an attempt to validate the conclusions from Chapter 3 for a real hurricane. It is found that otherwise identical simulations with and without radiation do not indicate that radiation plays a significant role in accelerating the genesis of Hurricane Matthew. It is hypothesized that this is due to the reanalysis product used for initial conditions having a nearly saturated region near the tropical disturbance when the simulations are initialized (Section 4.3).

6.3 Avenues for Future Work

There are several avenues of future work that build off of the conclusions from this dissertation. Additional work is required to continue the study of LCVAs in other modeling frameworks and to observationally validate the evolution and motion of such vortices in real developing disturbances, as well as their link to TCG that we suggest in Chapter 2. This may be done with the use of boundary layer observations in tropical disturbances which have spatial resolution on the order of 1 km and temporal resolution on the order of ten minutes. The connection between LCVAs and "landfalling tornadoes" also warrants exploration due to the very large values of vertical vorticity we observe in LCVAs near the model surface in our simulation (e.g. Figure 2.6). Tornadoes frequently spawn in the outer rainbands of landfalling tropical systems (Orton, 1970), and are responsible for a considerable portion of TC damage and casualties (Novlan and Gray, 1974), so it is important to explore a link between these processes to gain insight into forecasting tornadic activity upon landfall.

The role of radiation in TCG also warrants further idealized and real-case numerical modeling to further support the conclusions discussed in Chapters 3 and 4. Observational studies, perhaps with the aid of satellite imagery, would also help with the understanding of the differential radiative forcing mechanism which takes place between a tropical disturbance and its surroundings. Nocturnal rapid core moistening provided by differential radiative cooling must be examined in this manner so that it may be correctly accounted for during tropical forecasting. Observations of the diurnal cycle of convection in real tropical disturbances may provide a pathway to understanding how effective this mechanism is for an individual event. Although it is impossible to modify longwave and shortwave radiation during a real hurricane, it is important that we fully understand how radiation impacts core moistening and convective activity so that the predictability of TCG may improve operationally and thus aid our efforts to provide earlier and more reliable warnings of landfalling hurricanes to those who live along tropical coastlines.

Bibliography

Aladangady, A., Aron-Dine, S., Dunn, W. E., Feiveson, L., Lengermann, P., Sahm, C. R. et al. (2016), The effect of hurricane matthew on consumer spending, Technical report, Board of Governors of the Federal Reserve System (US).

Arakawa, A. and Lamb, V. R. (1977), 'Computational design of the basic dynamical processes of the ucla general circulation model', Methods in computational physics **17**, 173–265.

Bell, G. D. and Keyser, D. (1993), 'Shear and curvature vorticity and potential-vorticity interchanges: Interpretation and application to a cutoff cyclone event', Monthly weather review **121**(1), 76–102.

Bister, M. and Emanuel, K. A. (1997), 'The genesis of hurricane guillermo: Texmex analyses and a modeling study', Monthly weather review **125**(10), 2662–2682.

Blake, E. S. and Gibney, E. J. (2011), 'Noaa technical memorandum nws nhc-6: The deadliest, costliest, and most intense united states tropical cyclones from 1851 to 2010 (and other frequently requested hurricane facts)', National Weather Service, National Hurricane Center, Miami, Florida .

Bu, Y. P., Fovell, R. G. and Corbosiero, K. L. (2014), 'Influence of cloud–radiative forcing on tropical cyclone structure', Journal of the Atmospheric Sciences **71**(5), 1644–1662.

Burpee, R. W. (1972), 'The origin and structure of easterly waves in the lower troposphere of north africa', Journal of the Atmospheric Sciences **29**(1), 77–90.

Cotton, W. R., Pielke Sr, R., Walko, R., Liston, G., Tremback, C., Jiang, H., McAnelly, R., Harrington, J., Nicholls, M., Carrio, G. et al. (2003), 'Rams 2001: Current status and future directions', Meteorology and Atmospheric Physics **82**(1-4), 5–29.

Craig, G. C. (1996), 'Numerical experiments on radiation and tropical cyclones', Quarterly Journal of the Royal Meteorological Society **122**(530), 415–422.

Davis, C. A. (2015), 'The formation of moist vortices and tropical cyclones in idealized simulations', Journal of the Atmospheric Sciences **72**(9), 3499–3516.

Davis, C. A. and Ahijevych, D. A. (2012), ‘Mesoscale structural evolution of three tropical weather systems observed during predict’, Journal of the Atmospheric Sciences **69**(4), 1284–1305.

Drager, A. J. and van den Heever, S. C. (2017), ‘Characterizing convective cold pools’, Journal of Advances in Modeling Earth Systems **9**(2), 1091–1115.

Dritschel, D. and Waugh, D. (1992), ‘Quantification of the inelastic interaction of unequal vortices in two-dimensional vortex dynamics’, Physics of Fluids A: Fluid Dynamics **4**(8), 1737–1744.

Dudhia, J. (1989), ‘Numerical study of convection observed during the winter monsoon experiment using a mesoscale two-dimensional model’, Journal of the atmospheric sciences **46**(20), 3077–3107.

Dunion, J. P., Thorncroft, C. D. and Nolan, D. S. (2019), ‘Tropical cyclone diurnal cycle signals in a hurricane nature run’, Monthly Weather Review **147**(1), 363–388.

Dunion, J. P., Thorncroft, C. D. and Velden, C. S. (2014), ‘The tropical cyclone diurnal cycle of mature hurricanes’, Monthly Weather Review **142**(10), 3900–3919.

Dunkerton, T. J., Montgomery, M. and Wang, Z. (2009), ‘Tropical cyclogenesis in a tropical wave critical layer: Easterly waves.’, Atmospheric Chemistry & Physics **9**(15).

Duran, P. and Molinari, J. (2019), ‘Tropopause evolution in a rapidly intensifying tropical cyclone: A static stability budget analysis in an idealized axisymmetric framework’, Journal of the Atmospheric Sciences **76**(1), 209–229.

Eastin, M. D., Gardner, T. L., Link, M. C. and Smith, K. C. (2012), ‘Surface cold pools in the outer rainbands of tropical storm hanna (2008) near landfall’, Monthly Weather Review **140**(2), 471–491.

ECMWF (2009, updated monthly), ‘Era-interim project’.
URL: *https://doi.org/10.5065/D6CR5RD9*

Elsner, J., Lehmiller, G. and Kimberlain, T. (1996), ‘Objective classification of atlantic hurricanes’, Journal of Climate **9**(11), 2880–2889.

Fang, J. and Zhang, F. (2011), ‘Evolution of multiscale vortices in the development of hurricane dolly (2008)’, Journal of the Atmospheric Sciences **68**(1), 103–122.

Fingerhut, W. A. (1978), ‘A numerical model of a diurnally varying tropical cloud cluster disturbance’, Monthly Weather Review **106**(2), 255–264.

Fovell, R. G., Bu, Y. P., Corbosiero, K. L., Tung, W.-w., Cao, Y., Kuo, H.-C., Hsu, L.-h. and Su, H. (2016), ‘Influence of cloud microphysics and radiation on tropical cyclone structure and motion’, Meteorological Monographs **56**, 11–1.

Gjorgjievska, S. and Raymond, D. J. (2014), ‘Interaction between dynamics and thermodynamics during tropical cyclogenesis’, Atmospheric Chemistry and Physics **14**(6), 3065–3082.

Godbole, R. V. (1973), ‘On destabilization of clouds by radiative cooling’, Monthly Weather Review **101**(6), 496–500.

Gopalakrishnan, S. G., Goldenberg, S., Quirino, T., Zhang, X., Marks Jr, F., Yeh, K.-S., Atlas, R. and Tallapragada, V. (2012), ‘Toward improving high-resolution numerical hurricane forecasting: Influence of model horizontal grid resolution, initialization, and physics’, Weather and Forecasting **27**(3), 647–666.

Gray, W. M. (1968), ‘Global view of the origin of tropical disturbances and storms’, Monthly Weather Review **96**(10), 669–700.

Gray, W. M. and Jacobson Jr, R. W. (1977), ‘Diurnal variation of deep cumulus convection’, Monthly Weather Review **105**(9), 1171–1188.

Harr, P. A. and Elsberry, R. L. (1996), ‘Structure of a mesoscale convective system embedded in typhoon robyn during tcm-93’, Monthly weather review **124**(4), 634–652.

Harrington, J. Y. (1997), The effects of radiative and microphysical processes on simulated warm and transition season Arctic stratus, PhD thesis, Colorado State University.

Haynes, P. and McIntyre, M. (1987), ‘On the evolution of vorticity and potential vorticity in the presence of diabatic heating and frictional or other forces’, Journal of the Atmospheric Sciences **44**(5), 828–841.

Hendricks, E. A., Montgomery, M. T. and Davis, C. A. (2004), ‘The role of vortical hot towers in the formation of tropical cyclone diana (1984)’, Journal of the atmospheric sciences **61**(11), 1209–1232.

Hill, G. E. (1974), ‘Factors controlling the size and spacing of cumulus clouds as revealed by numerical experiments’, Journal of the Atmospheric Sciences **31**(3), 646–673.

Holton, J. (1992), ‘An introduction to dynamic meteorology’, Academic Press .

Hong, S.-Y., Noh, Y. and Dudhia, J. (2006), ‘A new vertical diffusion package with an explicit treatment of entrainment processes’, Monthly Weather Review **134**(9), 2318–2341.

Iacono, M. J., Delamere, J. S., Mlawer, E. J., Shephard, M. W., Clough, S. A. and Collins, W. D. (2008), ‘Radiative forcing by long-lived greenhouse gases: Calculations with the aer radiative transfer models’, Journal of Geophysical Research: Atmospheres **113**(D13).

Jacobson, R. W. and Gray, W. M. (1976), ‘Diurnal variation of oceanic deep cumulus convection’, Atmospheric science paper; no. 243 .

Janjić, Z. I. (2000), ‘Comments on development and evaluation of a convection scheme for use in climate models’, Journal of the Atmospheric Sciences **57**(21), 3686–3686.

Jordan, C. L. (1958), 'Mean soundings for the west indies area', Journal of Meteorology **15**(1), 91–97.

Kilroy, G. and Smith, R. K. (2013), 'A numerical study of rotating convection during tropical cyclogenesis', Quarterly Journal of the Royal Meteorological Society **139**(674), 1255–1269.

Kilroy, G., Smith, R. K. and Montgomery, M. T. (2016), 'A unified view of tropical cyclogenesis and intensification', Quarterly Journal of the Royal Meteorological Society .

Kilroy, G., Smith, R. K. and Montgomery, M. T. (2018), 'The role of heating and cooling associated with ice processes on tropical cyclogenesis and intensification', Quarterly Journal of the Royal Meteorological Society **144**(710), 99–114.

Knaff, J. A., Slocum, C. J. and Musgrave, K. D. (2019), 'Quantification and exploration of diurnal oscillations in tropical cyclones', Monthly Weather Review .

Kraus, E. B. (1963), 'The diurnal precipitation change over the sea', Journal of the Atmospheric Sciences **20**(6), 551–556.

Kutty, G. and Gohil, K. (2017), 'The role of mid-level vortex in the intensification and weakening of tropical cyclones', Journal of Earth System Science **126**(7), 94.

Lee, B. D. and Wilhelmson, R. B. (1997), 'The numerical simulation of non-supercell tornadogenesis. part i: Initiation and evolution of pretornadic misocyclone circulations along a dry outflow boundary', Journal of the atmospheric sciences **54**(1), 32–60.

Leppert, K. D. and Cecil, D. J. (2016), 'Tropical cyclone diurnal cycle as observed by trmm', Monthly weather review **144**(8), 2793–2808.

Lilly, D. K. (1962), 'On the numerical simulation of buoyant convection', Tellus **14**(2), 148–172.

Melander, M., Zabusky, N. and McWilliams, J. (1987), 'Asymmetric vortex merger in two dimensions: Which vortex is victorious?', The Physics of fluids **30**(9), 2610–2612.

Melander, M., Zabusky, N. and McWilliams, J. (1988), 'Symmetric vortex merger in two dimensions: causes and conditions', Journal of Fluid Mechanics **195**, 303–340.

Melhauser, C. and Zhang, F. (2014), 'Diurnal radiation cycle impact on the pregenesis environment of hurricane karl (2010)', Journal of the Atmospheric Sciences **71**(4), 1241–1259.

Meyers, M. P., Walko, R. L., Harrington, J. Y. and Cotton, W. R. (1997), 'New rams cloud microphysics parameterization. part ii: The two-moment scheme', Atmospheric Research **45**(1), 3–39.

Miller, R. A. and Frank, W. M. (1993), 'Radiative forcing of simulated tropical cloud clusters', Monthly weather review **121**(2), 482–498.

Montgomery, M., Nicholls, M., Cram, T. and Saunders, A. (2006), ‘A vortical hot tower route to tropical cyclogenesis’, Journal of the atmospheric sciences **63**(1), 355–386.

Montgomery, M. T., Dunkerton, T. and Wang, Z. (2010), ‘Coarse, intermediate and high resolution numerical simulations of the transition of a tropical wave critical layer to a tropical storm’, Atmospheric Chemistry and Physics **10**, 10803–10827.

Muller, C. J. and Romps, D. M. (2018), ‘Acceleration of tropical cyclogenesis by self-aggregation feedbacks’, Proceedings of the National Academy of Sciences **115**(12), 2930–2935.

Nair, U. S., Rappin, E., Foshee, E., Smith, W. P., Pielke Sr., R. A., Mahmood, R., Case, J. L., Blankenship, C. B., Shepherd, M., Santanello, J. A. and Niyogi, D. (2019), ‘Influence of land cover and soil moisture based brown ocean effect on an extreme rainfall event from a louisiana gulf coast tropical system (in review)’.

Navarro, E. L. and Hakim, G. J. (2016), ‘Idealized numerical modeling of the diurnal cycle of tropical cyclones’, Journal of the Atmospheric Sciences **73**(10), 4189–4201.

Navarro, E. L., Hakim, G. J. and Willoughby, H. E. (2017), ‘Balanced response of an axisymmetric tropical cyclone to periodic diurnal heating’, Journal of the Atmospheric Sciences **74**(10), 3325–3337.

Nicholls, M. (2015), ‘An investigation of how radiation may cause accelerated rates of tropical cyclogenesis and diurnal cycles of convective activity’, Atmos. Chem. Phys. **15**(5), 6125–6205.

Nicholls, M. E., Pielke Sr, R. A., Wheeler, D., Carrio, G. and Smith, W. P. (2018), ‘A numerical modelling investigation of the role of diabatic heating and cooling in the development of a mid-level vortex prior to tropical cyclogenesis–part 1: The response to stratiform components of diabatic forcing’, Atmospheric Chemistry and Physics **18**(19), 14393–14416.

Nicholls, M. E., Smith, W. P., Pielke Sr, R. A., Saleeby, S. M. and Wood, N. B. (2019a), ‘A numerical modelling study of the physical mechanisms causing radiation to accelerate tropical cyclogenesis and cause diurnal cycles (in review)’, Atmospheric Chemistry and Physics .

Nicholls, M. E., Smith, W. P. and Wallace, R. W. (2019b), ‘A numerical modeling investigation of vorticity generation around cold pool outflow boundaries during tropical cyclogenesis (in preparation)’.

Nicholls, M. and Montgomery, M. (2013), ‘An examination of two pathways to tropical cyclogenesis occurring in idealized simulations with a cloud-resolving numerical model’, Atmos. Chem. Phys. **13**, 5999–6022.

Nolan, D. S. (2007), ‘What is the trigger for tropical cyclogenesis’, Australian Meteorological Magazine **56**(4), 241.

Nolan, D. S. and McGauley, M. G. (2012), ‘Tropical cyclogenesis in wind shear: Climatological relationships and physical processes’, Cyclones: Formation, triggers, and control pp. 1–36.

Nolan, D. S., Zhang, J. A. and Stern, D. P. (2009), ‘Evaluation of planetary boundary layer parameterizations in tropical cyclones by comparison of in situ observations and high-resolution simulations of hurricane isabel (2003). part i: Initialization, maximum winds, and the outer-core boundary layer’, Monthly weather review **137**(11), 3651–3674.

Novlan, D. J. and Gray, W. M. (1974), ‘Hurricane-spawned tornadoes’, Monthly Weather Review **102**(7), 476–488.

O’Brien, J. J. (1970), ‘Alternative solutions to the classical vertical velocity problem’, Journal of Applied Meteorology **9**(2), 197–203.

Ooyama, K. V. (1982), ‘Conceptual evolution of the theory and modeling of the tropical cyclone’, J. Meteor. Soc. Japan **60**(1), 369–380.

Orton, R. (1970), Tornadoes associated with hurricane Beulah on September 19-23, 1967, National Emergency Training Center.

Pielke Jr, R. A. and Pielke Sr, R. A. (1997), Hurricanes: Their nature and impacts on society, John Wiley and Sons.

Pielke, R. A., Cotton, W., Walko, R. e. a., Tremback, C. J., Lyons, W. A., Grasso, L., Nicholls, M., Moran, M., Wesley, D., Lee, T. et al. (1992), ‘A comprehensive meteorological modeling system: Rams’, Meteorology and Atmospheric Physics **49**(1-4), 69–91.

Ramsay, H. A. (2013), ‘The effects of imposed stratospheric cooling on the maximum intensity of tropical cyclones in axisymmetric radiative–convective equilibrium’, Journal of Climate **26**(24), 9977–9985.

Rappin, E. D., Nolan, D. S. and Emanuel, K. A. (2010), ‘Thermodynamic control of tropical cyclogenesis in environments of radiative-convective equilibrium with shear’, Quarterly Journal of the Royal Meteorological Society **136**(653), 1954–1971.

Raymond, D. and López Carrillo, C. (2011), ‘The vorticity budget of developing typhoon nuri (2008)’, Atmospheric Chemistry and Physics **11**(1), 147–163.

Reasor, P. D., Montgomery, M. T. and Bosart, L. F. (2005), ‘Mesoscale observations of the genesis of hurricane dolly (1996)’, Journal of the atmospheric sciences **62**(9), 3151–3171.

Riehl, H. (1948), ‘On the formation of west atlantic hurricanes’, Studies of upper-air conditions in low latitudes. Rep **24**.

Riemer, M., Montgomery, M. and Nicholls, M. (2013), ‘Further examination of the thermodynamic modification of the inflow layer of tropical cyclones by vertical wind shear’, Atmos. Chem. Phys **13**, 327–346.

Ritchie, E. A. and Holland, G. J. (1997), 'Scale interactions during the formation of typhoon irving', Monthly weather review **125**(7), 1377–1396.

Rotunno, R. and Emanuel, K. A. (1987), 'An air-sea interaction theory for tropical cyclones. part ii: Evolutionary study using a nonhydrostatic axisymmetric numerical model', Journal of the Atmospheric Sciences **44**(3), 542–561.

Saucier, W. J. (1955), Principles of meteorological analysis, Courier Corporation.

Schenkel, B. A. (2009), An Examination Of Tropical Cyclone Evolution Using Curvature Vorticity And Shear Vorticity, PhD thesis, Florida State University.

Schmetz, J. and Beniston, M. (1986), 'Relative effects of solar and infrared radiative forcing in a mesoscale model', Boundary-Layer Meteorology **34**(1-2), 137–155.

Sharkov, E. A. (2011), Global tropical cyclogenesis, Springer Science & Business Media.

Sippel, J. A., Nielsen-Gammon, J. W. and Allen, S. E. (2006), 'The multiple-vortex nature of tropical cyclogenesis', Monthly weather review **134**(7), 1796–1814.

Skamarock, W. C. and Coauthors (2008), A description of the advanced research wrf version 3. ncar tech. note, Technical report, NCAR/TN-475+ STR.

Skamarock, W. C., Klemp, J. B., Dudhia, J., Gill, D. O., Barker, D. M., Wang, W. and Powers, J. G. (2005), A description of the advanced research wrf version 2, Technical report, DTIC Document.

Smagorinsky, J. (1963), 'General circulation experiments with the primitive equations: I. the basic experiment', Monthly weather review **91**(3), 99–164.

Smith, R. K. and Montgomery, M. T. (2016), 'Understanding hurricanes', Weather **71**(9), 219–223.

Smith, W. P. and Nicholls, M. E. (2019), 'On the creation and evolution of small scale low level vorticity anomalies during tropical cyclogenesis (accepted for publication)', Journal of the Atmospheric Sciences .

Smith, W. P., Nicholls, M. E. and Pielke Sr., R. A. (2019), 'The role of radiation in accelerating tropical cyclogenesis in idealized simulations (in review)', Journal of the Atmospheric Sciences .

Smith, W. P., Nicholls, M. E., Pielke Sr, R. A. and Thompson, G. (2020), 'The role of radiation in the genesis of atlantic hurricane matthew (2016) (in preparation)'.

Stewart, S. R. (2017), Tropical cyclone report: Hurricane matthew (al142016), Technical report, National Hurricane Center.

Tang, X., Tan, Z.-M., Fang, J., Sun, Y. Q. and Zhang, F. (2017), 'Impact of the diurnal radiation cycle on secondary eyewall formation', Journal of the Atmospheric Sciences **74**(9), 3079–3098.

Tang, X. and Zhang, F. (2016), 'Impacts of the diurnal radiation cycle on the formation, intensity, and structure of hurricane edouard (2014)', Journal of the Atmospheric Sciences **73**(7), 2871–2892.

Tao, W., Lang, S., Simpson, J., Sui, C., Ferrier, B. and Chou, M. (1996), 'Mechanisms of cloud-radiation interaction in the tropics and midlatitudes', Journal of the atmospheric sciences **53**(18), 2624–2651.

Thompson, G., Field, P. R., Rasmussen, R. M. and Hall, W. D. (2008), 'Explicit forecasts of winter precipitation using an improved bulk microphysics scheme. part ii: Implementation of a new snow parameterization', Monthly Weather Review **136**(12), 5095–5115.

Trabing, B. C., Bell, M. M. and Brown, B. R. (2019), 'Impacts of radiation and upper-tropospheric temperatures on tropical cyclone structure and intensity', Journal of the Atmospheric Sciences **76**(1), 135–153.

Tripoli, G. J. and Cotton, W. R. (1981), 'The use of lce-liquid water potential temperature as a thermodynamic variable in deep atmospheric models', Monthly Weather Review **109**(5), 1094–1102.

Van Sang, N., Smith, R. K. and Montgomery, M. T. (2008), 'Tropical-cyclone intensification and predictability in three dimensions', Quarterly Journal of the Royal Meteorological Society: A journal of the atmospheric sciences, applied meteorology and physical oceanography **134**(632), 563–582.

Walko, R. L., Cotton, W. R., Meyers, M. and Harrington, J. (1995), 'New rams cloud microphysics parameterization part i: the single-moment scheme', Atmospheric Research **38**(1-4), 29–62.

Wang, S., Camargo, S. J., Sobel, A. H. and Polvani, L. M. (2014), 'Impact of the tropopause temperature on the intensity of tropical cyclones: An idealized study using a mesoscale model', Journal of the Atmospheric Sciences **71**(11), 4333–4348.

Wang, Z., Montgomery, M. and Dunkerton, T. (2010), 'Genesis of pre-hurricane felix (2007). part ii: Warm core formation, precipitation evolution, and predictability', Journal of the Atmospheric Sciences **67**(6), 1730–1744.

Webster, P. J. and Stephens, G. L. (1980), 'Tropical upper-tropospheric extended clouds: Inferences from winter monex', Journal of the Atmospheric Sciences **37**(7), 1521–1541.

Wing, A. A., Camargo, S. J. and Sobel, A. H. (2016), 'Role of radiative–convective feedbacks in spontaneous tropical cyclogenesis in idealized numerical simulations', Journal of the Atmospheric Sciences **73**(7), 2633–2642.

Wong-Parodi, G. and Feygina, I. (2018), 'Factors influencing (mal) adaptive responses to natural disasters: the case of hurricane matthew', Weather, climate, and society **10**(4), 747–768.

Wurman, J. and Kosiba, K. (2018), ‘The role of small-scale vortices in enhancing surface winds and damage in hurricane harvey (2017)’, Monthly Weather Review **146**(3), 713–722.

Xu, K.-M. and Randall, D. A. (1995), ‘Impact of interactive radiative transfer on the macroscopic behavior of cumulus ensembles. part ii: Mechanisms for cloud-radiation interactions’, Journal of the atmospheric sciences **52**(7), 800–817.

Zehr, R. M. (1992), Tropical cyclogenesis in the western north pacific, Technical report, National Oceanic and Atmospheric Administration.

Appendix A

LCVA Hydrostatic and Cyclostrophic Balance (Chapter 2)

This appendix focuses on the nature of hydrostatic and cyclostrophic balances found in the genesis LCVA. Hydrostatic balance is approximately satisfied when

$$\frac{1}{\rho_0}\frac{\partial p'}{\partial z} - g\frac{\theta_v'}{\theta_{v,0}} \approx 0 \tag{A.1}$$

where p is pressure, ρ is density, θ_v is virtual potential temperature, the subscript 0 denotes a “background” profile and primes denote perturbations from said profile. This approach uses all points within a 20 km radius from the model center (the center of the parent circulation) to create a unique background profile for each time step, which perturbations can then be calculated from.

Cyclostrophic wind can be derived from setting the Coriolis force $f = 0$ in the formula for gradient wind balance, giving

$$V_{cyc} = \sqrt{-\frac{2r^2\theta_{v,0}\pi'}{(r^2 + a^2)}} \tag{A.2}$$

In Equation A.2, r denotes radius from the vortex center, a is an approximate RMW, $\theta_{v,0}$ is background virtual potential temperature as in Equation A.1, and π' is the perturbation Exner function. The Exner function is defined as

$$\pi = c_p * (\frac{P}{P_0})^{(R_d/c_p)} \tag{A.3}$$

for specific heat of dry air at constant pressure c_p, dry gas constant R_d, pressure P and reference pressure P_0. For LCVAs, we use $a = 4.0km$ and $P_0 = 10^5 Pa$.

Figure A.1 shows azimuthally averaged cross sections centered on the genesis LCVA at a model run time of 84 hours. Shown are tangential wind, vorticity, cyclostrophic wind, both sides of Equation A.1 and a difference field between the two. At this time, the genesis LCVA extends to about 3 km AGL (panel b). A comparison of panels a and c show some similarities, but the magnitude of the cyclostrophic wind is a bit higher than the observed tangential winds. The "nose" in panel a in the lowest several hundred meters is likely the result of boundary layer frictional convergence, discussed by Smith and Montgomery (2016), a process that is not reflected in the cyclostrophic wind formula. We conclude that the LCVA is in approximate cyclostrophic balance, and it is likely the relatively small effects of friction and the Coriolis force which lead to the slight magnitude disparity in these wind fields. We also conclude that the LCVA is in approximate hydrostatic balance at this time, evidenced by panel d having magnitudes near zero. Both of these conclusions are sensitive to the presence of convection near the LCVA; active convection causes some violation in these balances since strong vertical motion and diabatic heating are not accounted for in these simplified approximations.

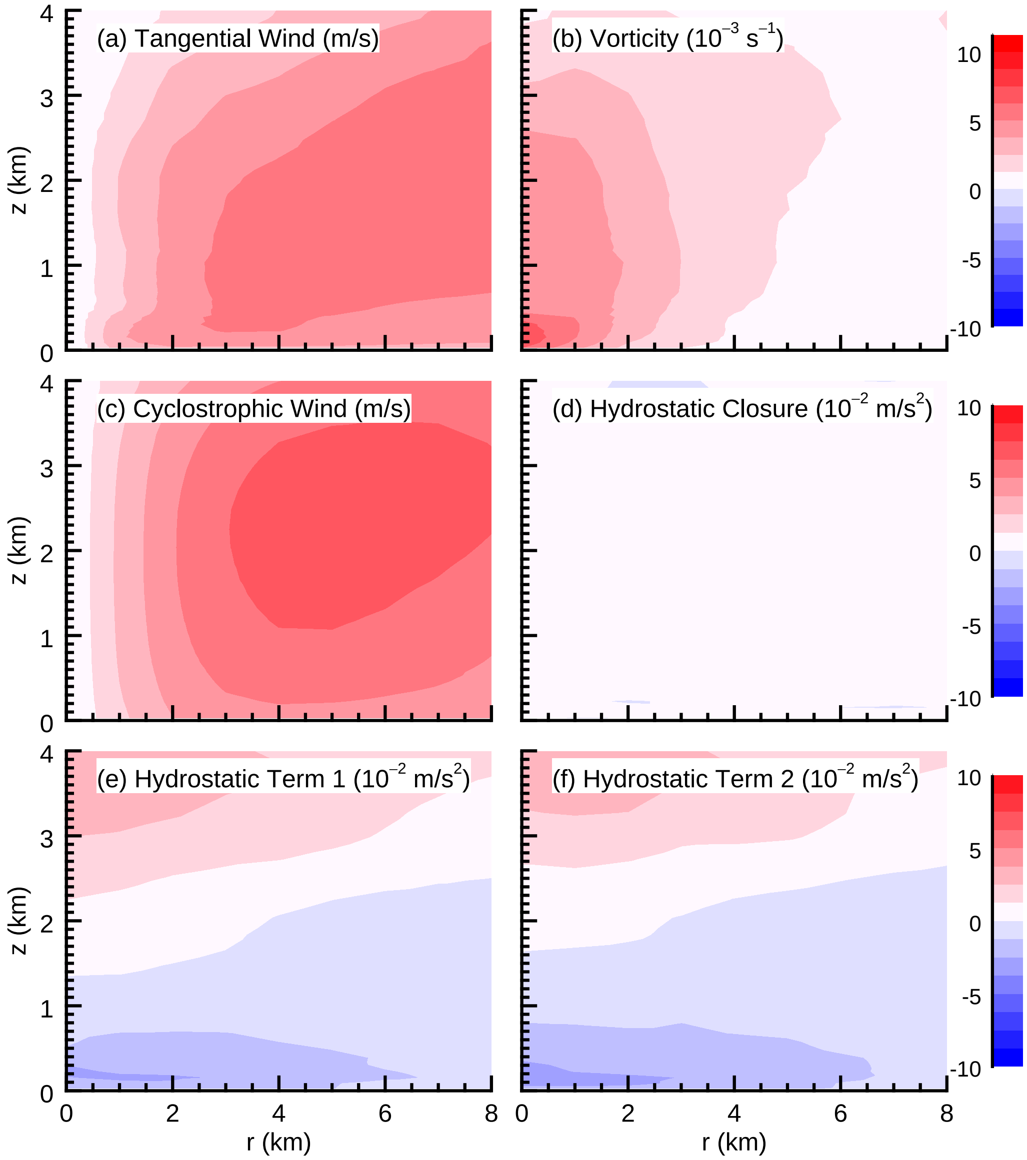

Figure A.1: Azimuthally averaged cross sections of (a) tangential winds, (b) vertical vorticity, (c) cyclostrophic wind, and the (e) first and (f) second terms in Equation A.1 at a model run time of 84 hours with r = 0 km corresponding to the center of the genesis LCVA. Panel d shows panel e minus panel f to depict how well the hydrostatic equation closes. Vorticity is scaled by a factor of 10^3 s^{-1}.

Appendix B

Surface-Based CAPE (Chapter 2)

The importance of surface-based convective available potential energy (SBCAPE) for small, rotating vorticity anomalies has been emphasized in prior modeling studies of TCG (Fang and Zhang, 2011; Nicholls and Montgomery, 2013), so we feel it is important to briefly discuss its evolution in our simulation as well. Figure B.1 shows horizontal cross sections of SBCAPE at various times during the evolution of the genesis LCVA. In panel a, the LCVA has not formed yet, and the enhanced region of SBCAPE serves as an important precondition for the convection that eventually forms it. After its initial formation, the SBCAPE field weakens near the LCVA (panel b) as convection briefly wanes before recovering in panel c. The fuel provided is enough to sustain convection long enough for the LCVA to reach the center (panel d). This analysis provides a window into understanding how convection is able to persist. It is theorized that the increasing surface fluxes with time allow for a faster recharge rate of SBCAPE for the genesis LCVA, however the mechanisms responsible for this recharge warrant further investigation.

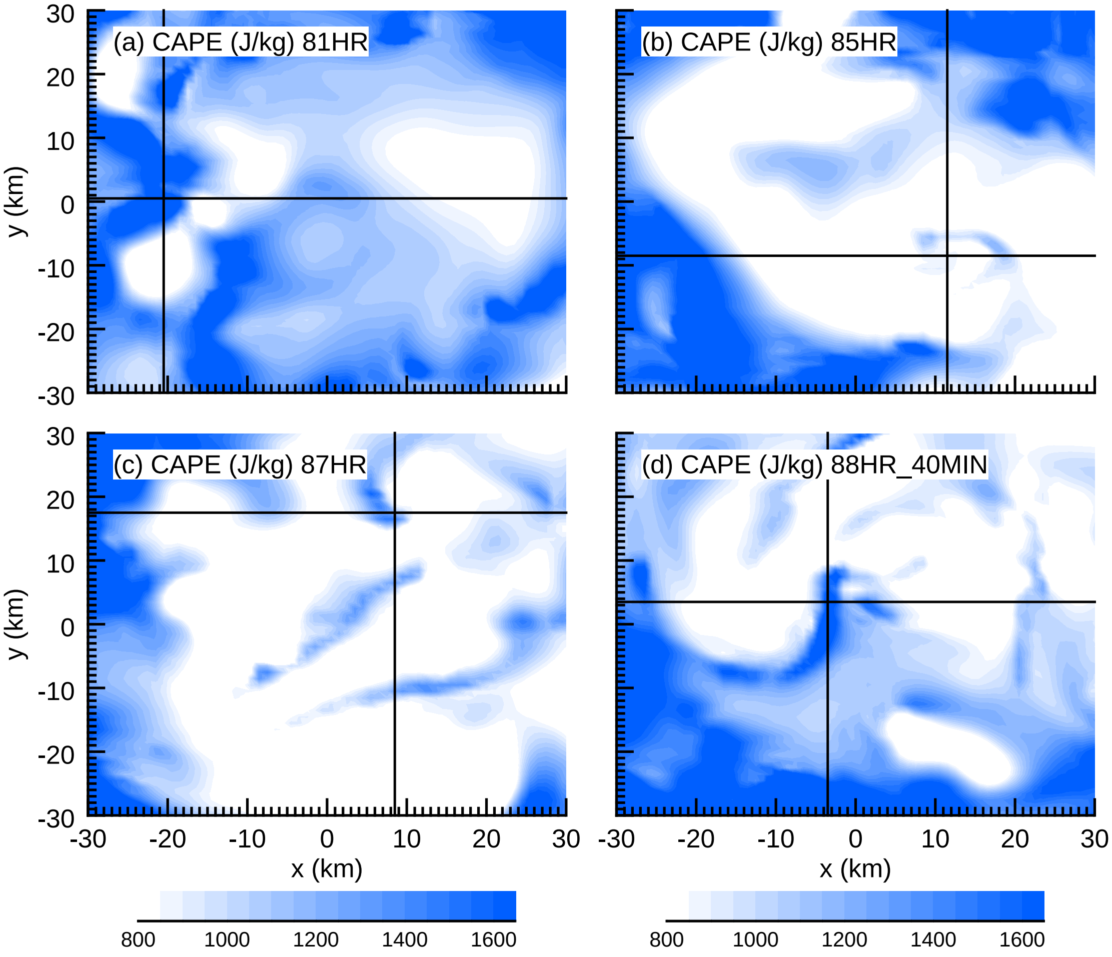

Figure B.1: Horizontal cross sections of SBCAPE at model run times of (a) 81 hours, (b) 85 hours, (c) 87 hours, and (d) 88 hours and 40 minutes. The crosshairs in each plot mark the low-level center of the genesis LCVA and are included only for reference.

Appendix C

Estimation of Friction for the Curvature Vorticity Budget (Chapter 2)

Although subgrid-scale fluxes are not output from RAMS in our simulation, we feel it is appropriate to provide an estimation for the magnitude of friction given the proximity of the curvature vorticity analysis to the model surface. The friction term included in Equation 2.4 is estimated according to:

$$F_{\zeta_c} = -g\frac{\partial}{\partial p}\left(\frac{\partial \tau_y}{\partial x} - \frac{\partial \tau_x}{\partial y}\right) \tag{C.1}$$

where $g = 9.81 m\ s^{-2}$ is acceleration due to gravity. The wind stresses at the surface are calculated by:

$$\begin{aligned} \tau_x &= \rho C_d \frac{p}{p_0} u_s V_s \\ \tau_y &= \rho C_d \frac{p}{p_0} v_s V_s \end{aligned} \tag{C.2}$$

where ρ is the density of air, p is the pressure, p_0 is a reference pressure, u_s, v_s and V_s are the surface zonal, meridional, and total wind speeds, respectively, and C_d is surface drag calculated by Deacon's formula (Riemer et al., 2013):

$$C_d = 1.1 \times 10^{-3} + (4.0 \times 10^{-5})V_s \tag{C.3}$$

Wind stresses in Equation C2 are assumed to reduce to 1% of their surface value at 800 hPa as done in Schenkel (2009).

Appendix D

Modification of Initial Vortex Winds in Idealized WRF Simulations (Chapter 3)

The default vortex in the tropical cyclone "test" case in WRF is based on that used in Rotunno and Emanuel (1987) and has maximum horizontal winds at the surface. These surface winds are linearly interpolated to reach zero at a height specified by the user. We modify this vertical interpolation to be similar to the method in Montgomery et al. (2006) so that our vortex more closely matches the initial RAMS vortex employed by other recent idealized modeling studies of TCG (Nicholls, 2015; Nicholls et al., 2018; Nicholls and Montgomery, 2013). Now, the vortex is defined by:

$$v(r,z) = v_{sfc}(r)\left\{A\left[cos\left(\frac{\pi z}{H}\right)+1\right] - B\left[cos\left(\frac{2\pi z}{H}\right)-1\right]\right\} \tag{D.1}$$

where

$$v_{sfc}(r) = \sqrt{\left(\frac{v_{max}\ r}{r_{max}}\right)^2\left[\left(\frac{2r_{max}}{r+r_{max}}\right)^3 - \left(\frac{2r_{max}}{r_0+r_{max}}\right)^3\right] + \frac{1}{4}f^2r^2}\ - \frac{1}{2}fr \tag{D.2}$$

In Equations D.1 and D.2, A and B are scalars, H is the height of the vortex (above which the wind speeds are zero), v_{max} is the maximum value of the vortex winds, r_{max} is the radius of maximum winds, r_0 is the maximum radius occupied by the vortex (outside which the wind speeds are zero), and f is the Coriolis parameter, all of which are specified by the user. For our simulations, we choose the following values: $A = 0.5,\ B = 0.7,\ H =$

$9.5km$, $r_{max} = 125km$, $r_0 = 400km$, and $f = 3.8\ x\ 10^{-5}\ s^{-1}$ (corresponding to 15°N latitude). To produce three different initial vortex strengths, we chose values for v_{max} of 7.0, 8.8, and $10.6m\ s^{-1}$ (corresponding to the "Weak," "Medium," and "Strong" initial vortices, respectively). Because of the new vertical interpolation method we employ (Equation D.1), these values chosen for v_{max} do not match the actual maximum winds found in the domain initially; the values that do result are those listed in Table 3.1. Because this vortex formulation is designed to exist in azimuthal (r,z) space, WRF-ARW "unravels" this vortex into three-dimensional space so that a simulation may be run.

Appendix E

Changes to Initial Sounding for MOIST runs (Chapter 3)

To validate the hypothesis that a sufficiently strong initial vortex with a deep moisture anomaly would develop in about the same time regardless of the influence of radiation, we modify the horizontally homogeneous initial sounding used in the model for four model runs ("RAD_Strong_MOIST," "NORAD_Strong_MOIST," "RAD_Strong_MOIST_LL," and "NORAD_Strong_LLMOIST," see Table 3.2 and Section 3.3.3). Table E.1 shows the vapor mixing ratios from the moistened soundings next to those of the default Jordan (1958) sounding used in all other simulations, with difference values provided in parentheses.

Table E.1: Water vapor mixing ratios from the default sounding used in the idealized tropical cyclone "test" case in WRF (Jordan 1958), the new soundings used for the deep-moistened ("MOIST", Column 3), and low-level-moistened ("MOIST_LL", Column 4) simulations in this work. The difference between the modified sounding and the default value (in Column 2) is given in parentheses.

Height (m)	Jordan (1958) default sounding ($g\ kg^{-1}$)	Deep-Moistened sounding ($g\ kg^{-1}$)	Low-Level Moistened sounding ($g\ kg^{-1}$)
0	18.2	20.2 (2.0)	20.2 (2.0)
583	15.3	17.3 (2.0)	17.3 (2.0)
1547	11.0	13.0 (2.0)	12.0 (1.0)
2609	7.1	9.1 (2.0)	7.1 (0.0)
3792	4.6	6.6 (2.0)	4.6 (0.0)
5138	3.2	5.2 (2.0)	3.2 (0.0)
6703	1.4	3.0 (1.6)	1.4 (0.0)
8581	0.0	0.6 (0.6)	0.0 (0.0)
10935	0.0	0.0 (0.0)	0.0 (0.0)

Appendix F

Ensemble Simulations (Chapter 3)

Due to the stochastic nature of convection in our simulations, it is worthwhile to understand how the timing of TCG is impacted by subtle differences in the distribution of convection. With this in mind, in order to validate the robustness of the conclusions presented in this manuscript, ensemble simulations based on each of the twelve simulations in Table 3.2 are performed and discussed below. We generate two new SST fields which are used to rerun all of the simulations presented in Table 3.2. Running otherwise identical simulations with these SST differences provides insight into how significant the changes in radiation and moisture are as it pertains to the conclusions in this study.

We employ a "chaos sequence" approach to add small (order of 0.1°C) perturbations to the SST field. The value of the perturbation (x) at a given grid cell depends on its value at the previous grid cell, according to:

$$x[n+1] = r^{*}x[n]^{*}(1 - x[n]) \tag{F.1}$$

where r is a constant. The SST is then perturbed according to:

$$SST[n+1] = 28 + (0.2^{*}x[n+1]) - 0.1 \tag{F.2}$$

To create two distinct SST fields, we chose r = 3.7 and r = 3.9.

Table F.1 shows how long it took each ensemble member to undergo TCG. It can be seen that, by and large, the simulations presented in this study do not exhibit a strong

Table F.1: A list of the time it takes (in hours) for each ensemble member to undergo TCG.

Simulation Name	Constant SST Run	SST 1 (r = 3.7)	SST 2 (r = 3.9)
RAD_Weak	70	74	74
NORAD_Weak	>120	>120	>120
NOCRF_Weak	88	83	83
RAD_Medium	42	41	41
NORAD_Medium	91	94	97
RAD_Strong	32	32	32
NORAD_Strong	74	73	73
RAD_Strong_MOIST	25	25	24
NORAD_Strong_MOIST	29	31	31
RAD_Strong_MOIST_LL	48	49	46
NORAD_Strong_MOIST_LL	66	73	77
RAD_Weak_Remove	72	77	82

sensitivity to changes in the location and distribution of convection, suggesting that the experimental design does a reasonable job of supporting the conclusions in this manuscript.

Appendix G

Acronyms

AGL	Above Ground Level
ATOC	Department of Atmospheric and Oceanic Sciences
BMJ	Betts-Miller-Janjic
CAPE	Convectively Available Potential Energy
CIRES	Cooperative Institute for Research in Environmental Sciences
CSWR	Center for Severe Weather Research
CVA	Convectively-induced Vorticity Anomaly
DIFF	Diffusion
ECMWF	European Centre for Medium-range Weather Forecasting
ERA-I	ECMWF Reanalysis - Interim
ESSS	Earth System and Space Science
CRF	Cloud Radiative Forcing
HWRF	Hurricane Weather Research and Forecasting Model
IDL	Interactive Data Language
JAS	Journal of the Atmospheric Sciences
LCVA	Low-level Convectively-induced Vorticity Anomaly
MLV	Mid-Level Vortex
NHC	National Hurricane Center
NCAR	National Center for Atmospheric Research

NORAD	A simulation without radiation included
NSF	National Science Foundation
PBL	Planetary Boundary Layer
RAD	A simulation with radiation included
RAMS	Regional Atmospheric Modeling System
RH	Relative Humidity
RMW	Radius of Maximum Winds
RRTMG	Rapid Radiative Transfer Model - Goddard
SBCAPE	Surface-Based Convectively Available Potential Energy
SSCV	Small Surface Concentrated Vortex
SST	Sea Surface Temperature
TEXMEX	Tropical Experiment in Mexico
TC	Tropical Cyclone
TCG	Tropical Cyclogenesis
WRF	Weather Research and Forecasting Model
WRF-ARW	Advanced Research WRF
VHT	Vortical Hot Tower
YSU	Yonsei University